UNIVERSITY OF Southampton

University of Southampton Research Repository
ePrints Soton

Copyright © and Moral Rights for this thesis are retained by the author and/or other copyright owners. A copy can be downloaded for personal non-commercial research or study, without prior permission or charge. This thesis cannot be reproduced or quoted extensively from without first obtaining permission in writing from the copyright holder/s. The content must not be changed in any way or sold commercially in any format or medium without the formal permission of the copyright holders.

When referring to this work, full bibliographic details including the author, title, awarding institution and date of the thesis must be given e.g.

AUTHOR (year of submission) "Full thesis title", University of Southampton, name of the University School or Department, PhD Thesis, pagination

http://eprints.soton.ac.uk

UNIVERSITY OF SOUTHAMPTON

FACULTY OF NATURAL AND ENVIRONMENTAL SCIENCES

School of Ocean and Earth Science

The effect of eddies and Rossby waves on the Atlantic meridional overturning circulation at 26.5°N and their decay at the western boundary.

Louis Clément

A thesis submitted for the degree of Doctor of Philosophy

July 2014

UNIVERSITY OF SOUTHAMPTON

ABSTRACT

FACULTY OF NATURAL AND ENVIRONMENTAL SCIENCES
SCHOOL OF OCEAN AND EARTH SCIENCE

Doctor of Philosophy

The effect of eddies and Rossby waves on the Atlantic meridional overturning circulation at 26.5°N and their decay at the western boundary.

by Louis Clément

The meridional overturning circulation (MOC) at 26.5°N in the Atlantic has a standard deviation of 4.9 Sv and contains large fluctuations at subannual periods. The geostrophic component of the MOC is believed to be influenced on subannual timescales by eddies and Rossby waves. To quantify this effect, the vertical structure and surface characteristics of westward propagating signals are studied using altimetry data and full-depth mooring measurements from the RAPID array at 26.5°N. Westward propagating features are observed in the western North Atlantic in both datasets and have periods of 80–250 days in the first baroclinic mode. These features are still observed by the RAPID moorings 20 km offshore of the western boundary. The effect of eddies and Rossby waves on the geostrophic transport is quantified by representing their vertical structure with the first baroclinic mode. In total, 42% of the variance of the transbasin thermocline transport inferred from geostrophic calculations at 26.5°N can be attributed to first mode variability, which is associated with eddies and Rossby waves at periods of 80–250 days. The standard deviation of the transbasin thermocline transport due to eddies and Rossby waves is estimated to be 2.6 Sv.

Having observed eddies to propagate towards the western boundary; the aim of the second section is to study the eddy energy sink at the boundary as one component of the energy redistribution from large scale winds to smaller scale internal waves. This section investigates the generation of internal waves by eddies in the North Atlantic western boundary where eddies dissipate. The eddy presence and decay are measured from the altimetric surface relative vorticity associated with an array of full-depth current meters extending ∼100 km offshore at 26.5°N. In addition, internal waves are analysed over a topographic rise from 2-year high-frequency measurements of an Acoustic Doppler Current Profiler (ADCP), which is located 13 km offshore in 600 m deep water. Despite a polarity independence of the eddy decay observed from altimetric data, the bottommost 100 m flow is enhanced for anticyclones (25.2 cm s^{-1}) compared with cyclones (-4.7 cm s^{-1}). Accordingly, the internal wave field is sensitive to this polarity-dependent deep velocity. This is apparent from the eddy-modulated enhanced shear spectra and dissipation rates, which are obtained from a finescale parameterisation, ϵ=2.8×10^{-9} W kg^{-1} for $|v|$>8 cm s^{-1}, whilst ϵ=0.9×10^{-9} W kg^{-1} for $|v|$<8 cm s^{-1}. The local dissipation of anticyclones significantly contributes to the eddy decay at the western boundaries. The present study underlines the importance of oceanic western boundaries for removing the energy of low-mode westward propagating eddies to higher mode internal waves.

Contents

List of Figures

List of Tables

Declaration Of Authorship

I, Louis Clément declare that this thesis and the work presented in it are my own and has been generated by me as the result of my own original research.

The effect of eddies and Rossby waves on the Atlantic meridional overturning circulation at 26.5°N and their decay at the western boundary.

I confirm that:

1. This work was done wholly or mainly while in candidature for a research degree at this University;
2. Where any part of this thesis has previously been submitted for a degree or any other qualification at this University or any other institution, this has been clearly stated;
3. Where I have consulted the published work of others, this is always clearly attributed;
4. Where I have quoted from the work of others, the source is always given. With the exception of such quotations, this thesis is entirely my own work;
5. I have acknowledged all main sources of help;
6. Where the thesis is based on work done by myself jointly with others, I have made clear exactly what was done by others and what I have contributed myself;
7. The results of the second and third chapter have been published in
   L. Clément, E. Frajka-Williams, Z. B. Szuts, and S. A. Cunningham (2014), Vertical structure of eddies and Rossby waves, and their effect on the Atlantic meridional overturning circulation at 26.5°N, *J. Geophys. Res. Oceans, 119*

Signed: .....

Date: .....

Acknowledgements

In particular, I would like to thank Eleanor who has been a great inspiration over the past few years. I will remember for a long time to come her willingness to explore new ideas and her approach to tackling challenging problems. She has been of great support throughout my thesis and I am extremely grateful that she made herself so available whenever I had questions. I also want to thank my other supervisors Zoli, Stuart and Harry. Zoli, especially, has been of considerable help throughout the thesis. He was very generous with his time, explaining various concepts in oceanography and my work strongly benefited from his advice. I am also grateful to all the other scientists in Southampton, through whom I broadened my interests in oceanography. Joel in particular was always supportive.

I also want to thank Alberto who, by acting as my panel chair, gave me valuable advice throughout the thesis. Furthermore, I had the chance to work with Kurt who hosted me at WHOI and who shared his enthusiasm for his research. This year, I enjoyed the opportunity to work with Katy and Alex, who were both very supportive and took the time to introduce and explain new areas of research.

During my years in Southampton, I enjoyed being part of the PhD community where I made many new friends. I particularly want to thank Chris, Simon and Ben for sharing new interests and the ups and downs of postgraduate life. A particular thanks goes to my family and friends from Paris. I could not have accomplished a PhD without the support of my close family Sophie, Pierre, Sarah, Pascal, Junie, Charles, Sarah and Catherine. Finally, I want to thank Karen for always being by my side.

Chapter 1

Introduction

The Atlantic Meridional Overturning Circulation plays an essential role in the climate system by carrying warm surface waters poleward and returning cold deep waters southward from their formation sites. These warm surface waters release their heat into the atmosphere at midlatitudes. The heat can then contribute to the mild European climate once it is transported by the westerlies. The oceanic heat transport in the North Atlantic was estimated to carry 1.1 PW with an error of 0.3 PW (1 PW= 10^{15} W) at 25°N (Hall and Bryden, 1982). The ocean transports approximately 25% of the total heat flux which also includes the atmospheric contribution (Trenberth et al., 2001). An understanding of the strength and variability of the MOC is essential to comprehend the fluctuations of the mild European climate (Pohlmann et al., 2006). In addition, the significant role of the MOC has also been linked to the abrupt climate change of glacial cycles using paleoclimatic data (Broecker, 2003). Given the central role played by the MOC in our climate system, it is essential to study its sensitivity to the concentration of greenhouse gases. In the scenario of an increase concentration of CO_2 in the atmosphere, the MOC is expected to slowdown (Gregory et al., 2005). Despite earlier expectations of a slowly varying MOC, the subannual variability of the MOC (Cunningham et al., 2007) needs to be better understood to accurately identify any trend or long-term changes of the MOC.

Eddies and Rossby waves play a major role in the dynamics of the ocean. These westward propagating signals can affect both the large-scale circulation and the small-scale turbulence of the ocean. The study of their effect on the large scale circulation will be analysed in the first instance. The meridional overturning circulation (MOC) is a fundamental process of the climate system. Understanding the effect of westward propagating signals on the MOC is essential to distinguish the contribution of the inherent variability of the ocean from potential long-term changes. The contribution of eddies and Rossby waves on the MOC will be assessed using altimetric measurements along with full-depth hydrographic measurements from the RAPID program at 26.5°N. The fate of mesoscale eddies as they approach the boundary will be studied in the second part of the present work. The focus will be on the eddy contribution to the internal wave field over a steep topographic feature.

1.1 Measurements of the Atlantic Meridional Overturning Circulation

To estimate the MOC in the North Atlantic, transatlantic sections measured in 1957, 1981, 1992, 2004 and 2010 have previously been used (Fuglister, 1960; Roemmich and Wunsch, 1985; Bryden et al., 2005b, Atkinson et al., 2012). These sections provide a snapshot of the oceanic circulation around 26.5°N. Each section, from the Bahamas Islands to the African coast, measures the geostrophic transport estimated from repeated CTD (Conductivity, Temperature and Depth) measurements. The southward geostrophic transport is opposed by a mean northward Gulf Stream transport measured by telephonic cables in the Florida Straits and the northward Ekman transport inferred from wind stress climatologies. Using the first five transatlantic sections, Bryden et al. (2005b) found a 30% decrease in the MOC from 1957 and 2004. The decline was observed in the larger southward mid-ocean geostrophic transport above 1000 m and in the decrease of southward deep North Atlantic Deep Water between 3000 and 5000 m. The reduction of transport in both layers was close to the eddy uncertainty of 6 Sv estimated by Ganachaud (2003) from an inverse box model using hydrographic data. However, due to a thermocline temperature anomaly which is present several degrees off the western boundary and due to an uneven transport in the deep layers, Bryden et al. (2005b) discard an eddy-induced explanation. The quantification of the variability of the transbasin transport which is attributed to the eddy effect still remains an open question.

In order to obtain continuous measurements of the MOC, the RAPID-WATCH program (Fig. 1.1) has been developed from a UK-US collaboration. The transport in the basin interior within the RAPID array at 26.5°N relies on geostrophic measurements using full-depth moorings at the western and eastern boundaries of the Atlantic basin. The compensation of the geostrophic transport by the Gulf Stream and Ekman transports imposes a barotropic circulation, which is redistributed equally throughout the section in the RAPID methodology. Using the first year of measurements, which started in March 2004, Cunningham et al. (2007) found a strong variability in the overturning and in the upper mid-ocean transport of 18.7 $\pm$ 5.6 Sv and -16.1 $\pm$ 3.1 Sv, respectively. The range of the MOC variability over one year of measurements not only changed the perception of a slowly-varying MOC but it also underlined the importance of studying the subannual variability of the MOC.

1.2 Subannual variability of the MOC due to westward propagating features

The westward propagating anomalies contribution to the MOC variability was investigated in numerical models (Hirschi et al., 2007; Wunsch, 2008) and from the RAPID measurements (Kanzow et al., 2009). Wunsch (2008) and Kanzow et al. (2009) both

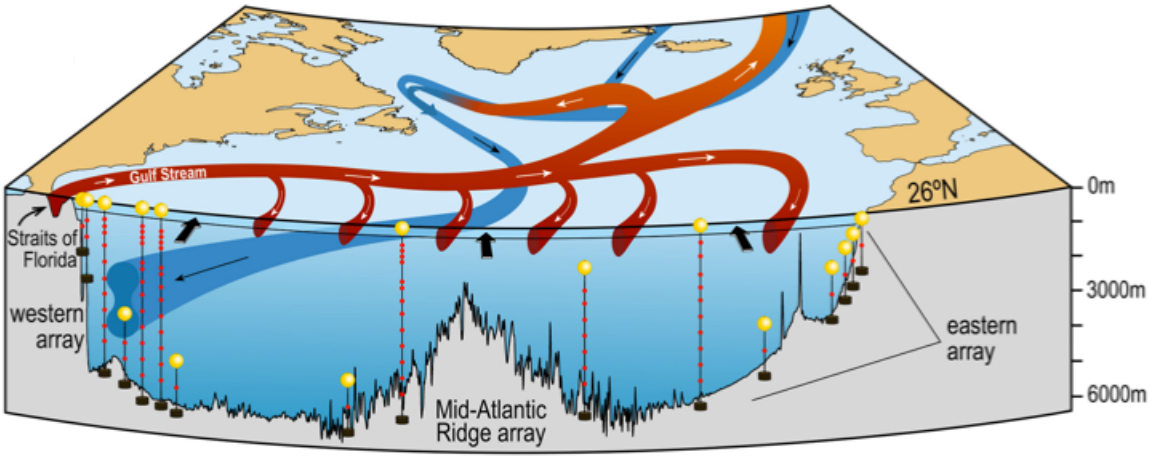

Figure 1.1: Schematic of the mooring array of the RAPID program extracted from Bryden et al. (2014) with the Ekman transport (black arrows) and the Gulf Stream transport restricted to the Straits of Florida at 26°N.

relied on the surface signature of these signals but found strongly divergent results with an rms of 16 and 4.2 Sv attributed to westward propagating anomalies, respectively. The effect of Rossby waves on the subannual and seasonal variability of the MOC was investigated by Hirschi et al. (2007) using an eddy-permiting model. The authors found that Rossby waves could affect the MOC through the modification of the density field and of the thermal-wind relation. Seasonal anomalies of the meridional transport were found to propagate at midlatitudes with the phase speed of baroclinic Rossby waves. However, an exact estimation of the influence of Rossby waves on the large scale circulation still needed to be quantified. Meanwhile, Wunsch (2008) studied the effect of eddies on the large scale geostrophic transport. The author relied on past observations (Wunsch, 1997) to define the vertical structure of the surface variability measured by the altimetry. This vertical structure, which is mainly associated with the effect of eddies, was related to the first baroclinic mode. Using an rms of 16 cm for the sea surface height anomaly (SSHA) around the Bahamas, Wunsch (2008) attributed an rms of 16 Sv of the geostrophic transport to the eddy variability.

The estimation found by Wunsch (2008) was however too large compared to the 3.1 Sv observed in Cunnigham et al. (2007). This disagreement led Kanzow et al. (2009) to further analyse the influence of eddies on the geostrophic transport using both the altimetry and full-depth moorings. The authors studied the variability of the transbasin thermocline transport, referred as the upper mid-ocean transport, and found a decrease of rms from 10.8 to 3.6 Sv by considering the weternmost mooring from 500 to 16 km offshore, respectively. The main finding of Kanzow et al. (2009) was to observe that the rms decrease of SSHA, of 11.2 to 5.3 cm by moving from 75.8 to 76.75°W, was associated with an rms decrease of dynamic height of similar amplitude. The authors put forward a dynamical explanation for the decrease of eddy and Rossby wave activity through the presence of boundary waves. Based on 15 years of altimetric measurements, Kanzow

et al. (2009) inferred that the variability of the transbasin thermocline transport of 4.2 Sv was still four times smaller than the estimation of Wunsch (2008). Furthermore, Kanzow et al. (2009) determined from an eddy-resolving model that the interannual to decadal variability of the MOC was not dominated by the effect of eddies. To evaluate this variability, the authors assumed that the MOC variability non coherent in one latitudinal degree is mostly attributed to the contribution of eddies. Despite the evaluation of an upper limit for the eddy variability of the meridional transport in Kanzow et al. (2009), a quantification of the influence of eddy on the upper mid-ocean transport still needs to be calculated. To estimate this effect, westward propagating features can first be studied using the global coverage of altimetry to determine their frequency and zonal wavelength. The vertical structure of these features can then be investigated and related to their surface signature using normal modes. From the knowledge of the vertical structure of westward propagating anomalies, their effect on the upper mid-ocean transport can be estimated.

1.3 Westward propagating features

Based on the improved accuracy of the altimetry in the past decades, global observations of eddies and Rossby waves are possible. The wavelength and frequency of their wave pattern can be estimated from altimetric measurements. The vertical structure of eddies has been described from hydrographic measurements (Parker, 1971) and also from experiments such as the MODE project, which studied their dynamics in the Sargasso Sea (MODE group, 1978). The development of several years of altimetric data with improved spatial and temporal resolution raised the question as to how the surface signature of westward propagating anomalies could be related to their subsurface structure. In this regard, the method of normal mode decomposition has been used in the past to describe the vertical structure of propagating features.

1.3.1 Surface characteristics of eddies and Rossby waves

The global coverage of satellite altimetry provides an unprecedented description of the surface variability. The launch of the altimetric mission TOPEX/POSEIDON in 1992 improved the accuracy of the SSHA measurements to 4 cm and also reduced tidal aliasing with the M2 constituents previously observed in the GEOSAT mission (Schlax and Chelton, 1994). Using the first three years of sea surface height measurements, Chelton and Schlax (1996) were able to detect oceanic Rossby waves. Their global observations led subsequently to a vast area of research due to the role of these waves on the large scale circulation. This contribution was already known from the theory; they have been linked, for example, to the intensified western boundary currents in Anderson and Gill (1975). Rossby waves, which can transfer SSHA across the ocean, are created by buoyancy forcing, Kelvin waves, wind or coastal current anomalies (Cipollini et al., 2000).

Chelton and Schlax (1996) displayed a time-longitude plot –referred to as a Hovmoller plot– to describe the propagation of Rossby waves at a selected latitude. The authors used a Radon transform to estimate the Rossby wave phase speed and found faster phase speed in the western basin compared with the eastern basin. They attributed this difference to the deepening of the pycnocline. The authors were able to describe the latitudinal dependence of the phase speed, which decreases with increasing latitudes and so confirmed the expected link of Rossby waves with the latitudinal gradient of the Coriolis parameter. In addition, the phase speed was in agreement with the theoretical prediction of linear first baroclinic mode Rossby waves in the tropics but observed speeds were faster than the theory outside the tropics.

The discrepancy in phase speeds led to the development of extended theories which included the mean currents (Killworth et al., 1997), the topography (Tailleux and McWilliams, 2000) and both processes (Killworth and Blundell, 2003). Another method of estimating Rossby wave characteristics relied on 2D frequency-zonal wavelength spectra of time-longitude SSH diagrams. This method has the advantage of distinguishing westward propagating anomalies with varying periods and wavelengths. In this way, Cipollini et al. (1997) were able to determine the zonal wavelength, period and phase speed of propagating anomalies using SSH but also sea surface temperature from Along-Track Scanning Radiometer in the Northeast Atlantic. Osychny and Cornillon (2004) also used 2D spectra in the North Atlantic and detected two peaks around 25°N at 180-day and 700-day

The improved resolution of SSH with the merged altimetric missions TOPEX/POSEIDON and ERS-1/2 suggested that about 50% of the SSH variability was attributed to nonlinear eddies instead of Rossby waves (Chelton et al., 2007). The main consequence of this result was attributed to the trapping of eddies which can, as opposed to Rossby waves, transport water properties across the ocean. The nonlinear factor, defined in Chelton et al. (2007) as the ratio of the azimuthal velocity over the propagating speed of westward anomalies, is used to detect the presence of eddies. Eddies are observed to propagate westward at the phase speed of the linear Rossby wave theory rendering their distinction with Rossby waves challenging. Despite the difficulty of distinguishing the exact mechanism responsible for the propagation of westward anomalies, their frequency and zonal wavelength can be assessed from the global coverage of altimetry.

1.3.2 Vertical structure of westward propagating anomalies

The global knowledge of the oceanic surface dynamic provided by altimeters created an interest in depicting the vertical structure of westward propagating anomalies. The link between the sea surface variability and the first baroclinic mode was investigated in Stammer (1997) and Wunsch (1997). Stammer (1997) used the first three years of SSH and geostrophic velocity data to determine their frequency and wavenumber spectra in various dynamical regions of the ocean: the bounday currents, and the tropical and ex-

tratropical regions. The author found a significant correlation of 0.81 between the eddy scale and the Rossby radius of the first baroclinic mode. The eddy scale is defined in Stammer (1997) as the lag of the first zero crossing of the spatial autocorrelation of SSH. The Rossby radius is calculated by solving a Sturm-Liouville equation given a buoyancy frequency extracted from the climatology of Levitus et al. (1994). From the correlation found between the eddy scale and the Rossby radius, the author concluded that the surface variability was mostly attributable to the first mode signal. The author was however unable to indicate the importance of the barotropic mode relative to the baroclinic mode in the SSH variability. Wunsch (1997) studied the link between the surface kinetic energy and the kinetic energy of the barotropic and baroclinic modes based on a dataset of current meters at multiple locations. According to Wunsch (1997), the full depth kinetic energy is mainly divided between the barotropic and the first baroclinic mode. The structure of the first baroclinic mode, which is intensified at the surface, was however determined to be the most representative mode of the SSH variability in Wunsch (1997).

The RAPID mooring array provides a new dataset with which to investigate eddy and Rossby wave variability in three dimensions: zonal, vertical and time. Szuts et al. (2012) studied the vertical structure of fluctuations in the full-height RAPID mooring data and their correlation with SSHA. Szuts et al. (2012) observed a strong link between the first baroclinic mode and SSHA variability in the ocean interior; a link which weakened toward the boundary. It is still necessary to investigate zonal propagation to connect mooring observations with the altimetric signature of propagating signals.

1.4 Eddy decay at the western boundary

Mesoscale eddies, with a vertical structure which is best characterised by the first baroclinic mode, are known to represent 90% of the subinertial kinetic energy of the flow as reported in Ferrari and Wunsch (2009). One major concern in closing the oceanic energy budget is to establish the contribution of each pathway of eddy energy before dissipation. According to Ferrari and Wunsch (2009), several processes can be responsible for the dissipation of the eddy energy: bottom drag, loss of balance, interaction with internal wave field, interaction with the continental margin and wind work. The dissipation of eddy energy by quadratic bottom boundary layer drag was estimated to be of 0.2 to 0.8 TW in Sen et al. (2008). The large uncertainty of this estimate prevents the conclusion that bottom drag is the dominant process in energy dissipation. Nevertheless, the interaction between eddies and internal waves may still be a significant process in the eddy dissipation. The difficulty of measuring both processes simultaneously, however, does not facilitate the identification of the eddy/internal wave interaction in the ocean.

One mechanism by which eddy bottom flow is believed to contribute to the internal wave field and subsequently to the small-scale turbulence is through the generation of

lee waves over topographic features (Nikurashin and Ferrari, 2011). This mechanism is dependent on the scales of the topographic feature H, the bottom velocity U_0 and the buoyancy frequency N_0 (Bell, 1975; Gill, 1982) as defined through the dependence of the topographic Froude number $\mathrm{Fr}_{topo}=N_0H/U_0$. Polzin et al. (1997) were able to relate the enhanced diapycnal diffusivity to the rough topography of the Brazil Basin. This observation supports the hypothesis of creation of internal waves due to the interaction of tidal current over topographic features. The breaking of internal waves is then responsible for the enhanced diapycnal diffusivity. A similar process of lee wave generation is believed to happen in the presence of eddy intensified flow and has been observed in the Southern Ocean (Nikurashin and Ferrari, 2010; Brearley et al., 2013), which is characterised by particularly strong bottom flow and rough topography. Nikurashin and Ferrari (2010) and Brearley et al. (2013) analysed profiles of lowered acoustic Doppler current profiler and moored current meters, respectively. Both studies are located in the Drake Passage which is characterised by maximum abyssal velocities around 20 cm s^{-1}. Due to the presence of the Antilles Current at the western boundary of the North Atlantic, bottom velocities are also expected to be intensified at this location which may enhance the internal wave activity.

1.5 Outline of the thesis

In this thesis, the interaction of westward propagating anomalies with the meridional circulation and the small-scale turbulence are analysed using both altimetric data and full-depth moorings. The two main questions addressed are:

- What is the effect of eddies and Rossby waves on the meridional overturning circulation measured at 26.5°N in the Atlantic?
- Is the internal wave field related to the eddy decay at the western boundary of the North Atlantic?

To address the first question, the zonal wavelength and the vertical structure of westward propagating anomalies will be studied in the second chapter. Using altimetric measurements across the North Atlantic, the zonal wavelength and frequency of westward propagating features will be identified. The vertical structure of eddies and Rossby waves will then be studied based on a modal decomposition of the isopycnal displacements of neutral density. For this analysis we use three moorings located at 20, 49 and 500 km offshore of the western boundary. We will identify a vertical structure for westward propagating anomalies at various longitudes across the mooring array. Another method referred as the Wentzel-Kramers-Brillouin-Jeffreys method will confirm the results of the modal decomposition. A spectral analysis at each mooring of the modal amplitudes will indicate the prevailing frequencies for varying vertical wavelengths. Once the best representation of the vertical structure of westward propagating anomalies is found with the modal decomposition, the phase speed of the propagating features between each

mooring section can be estimated using a cross-spectral analysis. This result can be compared to the phase speed attributed to SSHA at 26.5°N, which is determined from a 2D frequency-zonal wavelength spectra.

The effect of westward propagating features on the MOC will then be evaluated in the third chapter. The RAPID methodology and the calculation of the internal, external and upper mid-ocean transport will be presented. This methodology relies on a geostrophic calculation between the eastern and western boundary. The method will be adapted to only include the vertical structure of the first baroclinic mode found to best represent eddies and Rossby waves detected in the second chapter. The determination of the influence of westward propagating anomalies on the internal and upper mid-ocean transports will thus be possible.

The second question will be addressed in the fourth chapter. In order to detect eddies in the western basin of the North Atlantic as they approach the western boundary, the results of an eddy tracking product will be analysed. The focus will then be at the western boundary using current meters attached on full-depth moorings within 100 km of the coast to describe the deep velocity field in the presence of cyclones and anticyclones. The meridional velocity measured by an acoustic Doppler current profiler (ADCP) over a topographic rise will be analysed by applying a filter at subinertial, near-inertial and high frequencies. The shear variance measured by the ADCP will be used in a finescale parameterisation to estimate the rate of dissipation of turbulent kinetic energy for varying eddy conditions. Rotary spectra will confirm whether the direction of propagation of energy agrees with the theory of lee waves.

Chapter 2

The vertical structure and spectral characteristics of westward propagating anomalies

2.1 Introduction

The aim of the present chapter is to provide a description of the vertical structure of westward propagating signals. The identification of these features will first be obtained from satellite altimetry before being related to subsurface measurements of the RAPID mooring array. The main characteristics of eddies and Rossby waves, which are their westward phase speeds in the absence of mean current and their surface and subsurface signature, will be essential in their identification. Once these signals are detected their frequency can be determined, and it will become relevant to evaluate their effect on the geostrophic meridional transport in the following chapter. The characterisation of eddy and Rossby wave vertical structure is a fundamental step to estimate at which depth and frequency the large scale circulation is affected by them. One advantage of the RAPID array at 26.5°N encompassing the midlatitude boundary and interior regions is to provide information on the evolution of these features as they approach boundary currents and the steep topography.

Eddies have been observed over the past few decades in the North Atlantic. Parker (1971) described Gulf Stream rings in the Sargasso Sea which were coherent over the full water column. Extensive research was conducted in the 1970s to understand their dynamics within the POLYGONE, MODE and POLYMODE projects (Richman et al., 1977; MODE group, 1978) and also to observe their first baroclinic mode structure over flat topography. The advent of altimetric missions such as TOPEX/Poseidon two decades ago considerably extended the global observations and understanding of eddy dynamics. Rossby waves were in the meantime first observed at the ocean surface (Chelton and Schlax, 1996) once the removal of tidal aliasing was made possible in altimetric data. Though eddies and Rossby waves are two distinct processes, their common

properties of westward phase speeds and surface and subsurface signatures render their observational distinction more challenging (Chelton et al., 2007).

Satellites confirmed the picture of a highly turbulent ocean containing westward propagating features able to transfer energy and hydrographic property anomalies across the ocean. The link between surface and subsurface variability became particularly relevant to understand these signals and their effect on the large scale circulation. The decomposition in normal modes can be applied to westward propagating processes of larger horizontal than vertical scale in order to facilitate their identification and characterisation. The first baroclinic mode was found to be the most representative mode of enhanced surface energy (Stammer, 1997; Wunsch, 1997). The RAPID mooring array provides a new dataset with which to investigate eddy and Rossby wave variability in three dimensions: zonal, vertical and time. Szuts et al. (2012) studied the vertical structure of fluctuations in the full-height RAPID mooring data and their correlation with SSHA. They observed a strong link between the first baroclinic mode and SSHA variability in the ocean interior; a link which weakened toward the boundary. It is still necessary to investigate zonal propagation to connect mooring observations with the altimetric signature of propagating signals.

In the present chapter a modal decomposition will be done on isopycnal displacements once the existence of propagating features have been confirmed from the altimetry and subsurface measurements. The zonal extent and phase speed of propagating features will be determined using altimetry. Their frequency and zonal wavelength will reveal a wave pattern which can be compared to linear Rossby wave theory. The frequency content associated with these anomalies will also be detected as they propagate throughout the mooring array.

2.2 Data

2.2.1 Hydrographic data

The array of full-depth moorings at the western boundary contains four moorings Wb2, Wb3, Wb4 and Wb5 located 20, 49, 108 and 500 km offshore along 26.5°, respectively. Each mooring is equipped with a set of SBE37 MicroCAT (Sea-Bird Electronics, Bellevue, WA, USA) CTD (Conductivity, Temperature, Depth) to measure temperature, salinity and pressure profiles from April 2004 to January 2011. The short record available at Wb4, which only started in 2008, limits the utility of Wb4 in most of our analyses. The vertical spacing is approximately 100 m in the top 500 m, 200 m from 500 to 1000 m and 500 m below 1000 m giving a total of about 15 instruments in the water column (Table 2.1). MicroCAT CTDs are calibrated before and after each deployment against a lowered CTD package to improve their accuracy to 0.001°C for temperature, 0.002 psu for salinity and 5-10 dbar for pressure. Data are sampled by the

	Mooring name	Start date	End date	Lat (°N)	Lon (°W)	Water depth (m)	CTD nb (≤1000 m)	Top CTD depth (m)
Wb5	mochae_1_362	24/3/2004	15/5/2005	26°29.4	71°58.2	5295	15 (6)	50
	mochae_2_368	17/5/2005	2/10/2006	26°30.10	71°58.28	5298	16 (7)	50
	mochae_3_373	5/10/2006	13/4/2008	26°30.000	71°58.300	5297	16 (7)	50
	mochae_4_383	14/4/2008	28/11/2009	26°30.33	71°58.230	5293	16 (6)	80
	mochae_5_392	29/11/2009	21/4/2011	26°30.16	71°58.70	5294	16 (7)	35
Wb4	wb4_5_200804	28/4/2008	27/4/2009	26°24.91	75°41.89	4705	15 (6)	105
	wb4_6_200908	26/4/2009	29/11/2010	26°21.180	75°43.320	4713	15 (7)	40
	wb4_7_201026	30/11/2010	23/4/2011	26°21.692	75°44.150	4715	15 (7)	35
Wb3	mochab_1_361	25/3/2004	11/5/2005	26°29.95	76°29.67	4846	14 (7)	50
	mochab_2_367	13/5/2005	6/10/2006	26°29.73	76°29.98	4840	14 (6)	100
	mochab_3_372	7/10/2006	17/4/2008	26°29.680	76°29.940	4840	16 (7)	50
	mochab_4_382	18/4/2008	1/12/2009	26°29.530	76°30.040	4858	16 (7)	60
	mochab_5_391	2/12/2009	25/4/2011	26°29.37	76°30.02	4840	15 (6)	50
Wb2	wb2_1_200419	26/3/2004	11/5/2005	26°30.92	76°44.46	3898	14 (6)	104
	wb2_2_200528	14/5/2005	9/3/2006	26°30.62	76°44.63	3893	11 (5)	250
	wb2_3_200606	23/3/2006	8/10/2006	26°30.5	76°44.5	3909	14 (6)	50
	wb2_4_200636	11/10/2006	27/3/2007	26°30.719	76°44.159	3909	16 (7)	85
	wb2_5_200702	29/3/2007	24/4/2008	26°30.618	76°44.604	3892	16 (7)	50
	wb2_6_200803	26/4/2008	29/4/2009	26°30.62	76°44.36	3890	16 (7)	50
	wb2_7_200907	29/4/2009	30/3/2010	26°30.800	76°44.420	3890	16 (7)	60
	wb2_8_201003	31/3/2010	27/4/2011	26°31.110	76°44.810	3900	15 (6)	75

Table 2.1: Mooring deployments at the western boundary (Wb2, Wb3, Wb4 and Wb5) of the RAPID mooring array from 2004 to 2011. Each deployment contains an array of MicroCAT CTDs distributed from the surface to the bottom.

CTDs every 30 mins. The data records are 2-day lowpass filtered using a 6th order Butterworth filter to remove tides and inertial oscillations and are then subsampled every 12 hours. Hydrographic data are interpolated to every 20 dbar using climatologies of vertical temperature and salinity gradients as a function of temperature, following the method described in Johns et al. (2005).

Using neutral densities (γ^n), isopycnal displacements $\zeta(z,t)$ are calculated following Desaubies and Gregg (1981) as the vertical displacement of isopycnals from their time-mean depth $\bar{z}(\gamma^n)$,

$$\zeta(\bar{z}(\gamma^n),t) = z(\gamma^n,t) - \bar{z}(\gamma^n)\ . \tag{2.1}$$

Linear interpolations are used to transfer initial measurements in depth space $\gamma^n(z)$ to density space $z(\gamma^n)$. As the focus is to characterise deep propagating features, isopycnal displacements below 200 m only will be considered, thereby reducing atmospheric effects. This choice defines a constant upper limit coherent between moorings as opposed to various shallowest instrument depths between deployments (Tab. 2.1). The shallow depth at Wb2 changed for the second deployment when the shallowest instrument was not functioning.

Neutral densities are preferred to potential densities for various reasons. Potential density reference at the surface (σ_θ) does not increase monotonically with depth and contains a deep maximum around 4000 dbar instead of at the seafloor in the western North Atlantic, as mentioned in Lynn and Reid (1968). The non-monotonic evolu-

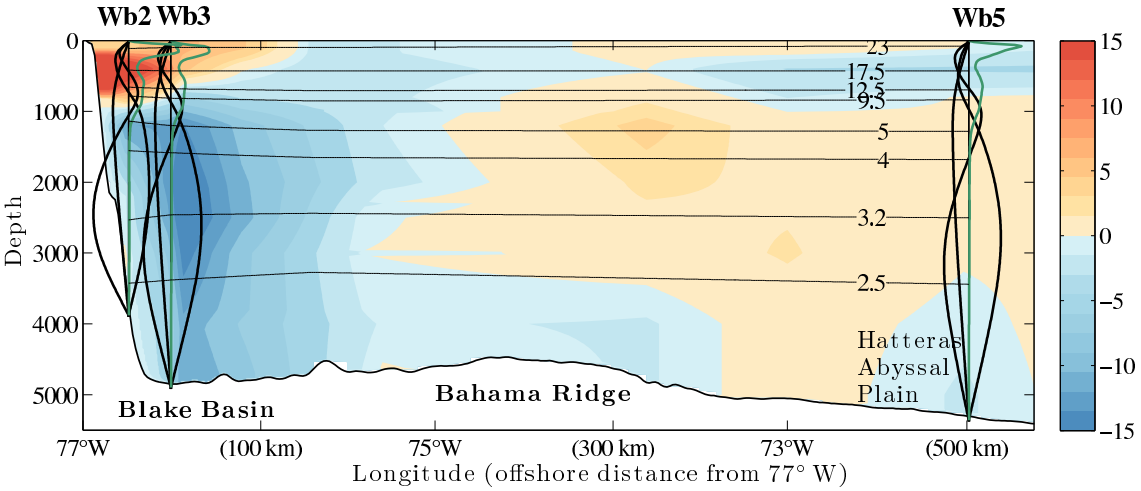

Figure 2.1: Bathymetry of the western boundary from ETOPO1 with the mean velocity (colors) from current meter arrays between 1986 and 1997 as described in Bryden et al. (2005a) and mean isotherms (black lines) from the RAPID array between 2004 to 2011. The three moorings of the boundary array Wb2, Wb3 and Wb5 are indicated with their mean buoyancy frequency profiles (green) and the modal structure of the first three baroclinic modes of isopycnal displacements (black).

tion prevents the calculation of isopycnal displacements from a mean potential density grid to a pressure grid with linear interpolation. A deeper reference level could be used (e.g. σ_4) but then shallow isopycnal displacements becomes less accurate. Neutral densities defined as continuous locally referenced potential density overcome the problem of having several references of potential density (Jackett and McDougall, 1997). In order to fit isopycnal displacement amplitudes with a vertical structure from modal decomposition it is essential to obtain continuity of pressure references. Neutral densities are computed using the package made available by CSIRO (`http://www.teos-10.org/preteos10_software/neutral_density.html`).

From temperature and salinity profiles, the specific volume anomaly (δ) relative to a specific volume of a standard water parcel with a temperature of 0°C and a salinity of 35 psu is calculated from the specific volume α ($1/\rho$) and CSIRO routines. The dynamic height is estimated by integrating the specific volume anomaly from the bottom to 200 dbar and is measured in dynamic centimeters (= 0.1 m^2s^{-2}). Omitting the top 200 dbar (Szuts et al., 2012) suppresses the impact of uneven sampling of the surface layer from deployment to deployment and minimises the effect of seasonal heat fluxes on our analysis (Gill and Niiler, 1973).

Data from western boundary current meter arrays (Bryden et al., 2005a) taken prior to RAPID from 1986 to 1997 were used to create a mean velocity section east of the Bahamas (Fig. 2.1). Unlike RAPID, which only uses current meters west of Wb3, these arrays extended 500 km offshore. These data come from the STACS (Subtropical Atlantic Climate Studies), WATTS (Western Atlantic Thermohaline Transport Study)

and ACCP (Atlantic Climate Change Program). They are made available by the World Ocean Circulation Experiment (WOCE) global data resource at `http://www.nodc.noaa.gov/woce/woce_v3/wocedata_1/cmdac/stranger/explist.htm`. As described in Bryden et al. (2005a) and Johns et al. (2008), the strong southward flowing Deep Western Boundary Current (DWBC) is observed from 1000 dbar to 4800 dbar with a maximum of 15 cm s^{-1} at 2000 m located 55 km offshore and a secondary maximum at 1200 m situated 20 km offshore. Two escarpments extending from the continental shelf at 26.6 and 26.7°N shelter Wb2 from the deep velocity maximum of the DWBC below 1600 m (Johns et al., 2008). The deep northward recirculation from 160 km to 580 km offshore balances a portion of the DWBC (Bryden et al., 2005a). The Antilles Current in the shallow 1000 m water with a maximum velocity of 40 cm s^{-1} is adjacent to the boundary and is compensated by an offshore shallow southward current.

The bathymetry of the North Atlantic comes from the ETOPO1 dataset provided by the National Geophysical Data Center found at `http://www.ngdc.noaa.gov/mgg/global/global.html`. This dataset is derived from satellite altimetry and hydrographic soundings (Amante and Eakins, 2009). Wb5 is located on the Hatteras Abyssal Plain (Fig. 2.1) approximately 5300 m deep which extends to 35°N (Richman et al., 1977). Wb2 is situated on the continental rise of the Bahamas escarpment and Wb3 in the Blake Basin. The Bahama Ridge is present between the Abyssal Plain and the Blake Basin; the Ridge shallows to approximately 4500 m and Wb4 is located on the western section of the Ridge.

2.2.2 Sea surface height anomalies

Sea surface height anomalies (SSHA) are produced by the Ssalto/Duacs multi-altimeter system (Ducet et al., 2000) available from the Aviso website (`http://www.aviso.oceanobs.com/duacs/`) with support from the CNES and are used for the period from October 1992 to January 2011. SSHA corresponds to anomalies of sea surface height relative to a mean sea surface. The 'reference' product is analysed to ensure homogeneity of data by merging up to two satellites Jason-2/Envisat or Jason-1/Envisat or Topex/Poseidon/ERS. The delayed-time product has 7-day temporal resolution with data projected on a 1/3° by 1/3° Mercator grid. Following Kanzow et al. (2009), a seasonal cycle was removed from the SSHA at each longitude along 26.5°N by subtracting the zonal mean of SSHA between 77°W and 14°W at each time step. This removes an approximate steric seasonal cycle from each longitude but leaves propagating or longitudinally-dependent SSH anomalies on seasonal time scales intact. SSHA is linearly interpolated onto the location of each mooring.

2.2.3 Rossby waves dispersion relation

For a wave of frequency ω such that $\omega \ll f$, a Rossby wave solution satisfies the quasi-geostrophic potential vorticity equation leading to the dispersion relation of a Rossby wave linking the wave frequency ω with the zonal k, meridional l wavenumbers, the mode number m, the Coriolis parameter f and its meridional gradient β

$$\omega_m = -\frac{\beta k}{k^2 + l^2 + \lambda_m^{-2}}. \tag{2.2}$$

The dispersion relation is obtained as described in Cushman-Roisin and Beckers (2011) in a continuously stratified fluid without topography and mean flow. The dispersion relation for each baroclinic mode is associated with a negative zonal phase speed (ω_m/k), indicative of westward propagation. The internal Rossby radius of deformation ($\lambda_m = c_m/f$) of each baroclinic mode is defined using the eigenvalue of the Sturm-Liouville system presented in 2.5.2. The Rossby radius at Wb5 (with $\lambda_1 = 47$ km), which is more representative of the western basin than Wb2 and Wb3 located in boundary-intensified currents, is used in the dispersion relation of the 2D spectrum. For long Rossby waves, the phase speed of each baroclinic mode is $c_m = \beta\lambda_m^2$. The maximum longwave frequency or cut-off frequency obtained for each baroclinic mode is $\omega_{m\_max} = -\beta\lambda_m/2$ assuming long meridional waves and zonal wavelength of $k_{m\_max} = \lambda_m^{-1}$. The cut-off frequency separates the nondispersive waves below ω_{m_max} from dispersive waves at higher frequencies.

2.3 Surface and subsurface variability of westward propagating signals

2.3.1 Sea surface variability

The global coverage of altimetry is first used to detect the presence and location of westward propagating anomalies in the North Atlantic. Their behaviour is studied at varying latitudes and longitudes and is related to the locations of bathymetric features such as the Mid-Atlantic Ridge (MAR) and the continental slope adjacent to the Bahamas. While observing westward propagating features it is essential to consider the location of the Gulf Stream (mostly restricted to the Florida Straits at midlatitudes) given its fundamental role in the decay and creation of eddies. The following analysis will assess whether propagating signals are purely westward at mid-latitudes. The focus will then be on the latitude of the RAPID array to determine if propagating signals are still observed at the westernmost mooring Wb2. The temporal variability of SSHA will be compared with subsurface variability, which will support a deeper analysis of the subsurface structure.

A methodology based on the lagged cross-correlation of SSHA similar to Fu (2006) is implemented to describe the mean propagation speed and direction of SSHA in the North Atlantic from March 2004 to January 2011. SSHA timeseries of the centre of

a 300-km diameter circle are lag-correlated with SSHA of each point within the circle with a maximum lag of 100 days. The maximum correlations are retained for each point if significant at 95% confidence levels. A speed is determined from the time lag of the maximum positive correlations and a direction from the position of each point relative to the circle centre. A mean speed and direction defining the arrow length and orientation in Fig. 2.2 can be attributed to the centre by averaging all the neighbouring values weighted by the maximum positive correlations.

Significance levels of the correlation coefficient are determinated at 95% confidence level from a test using Student′s t-distribution based on the degrees of freedom (Emery and Thomson, 2001). The test accepts or rejects the hypothesis of null correlation coefficient at the confidence interval. The effective degrees of freedom or the number of statistically independent variables is calculated from the number of measurements over the integral timescale. The integral timescale (T) is the integrated autocovariance function (C) to the first zero-crossing (T_0),

$$T = \frac{1}{C(0)} \int_0^{T_0} C(\tau) d\tau. \tag{2.3}$$

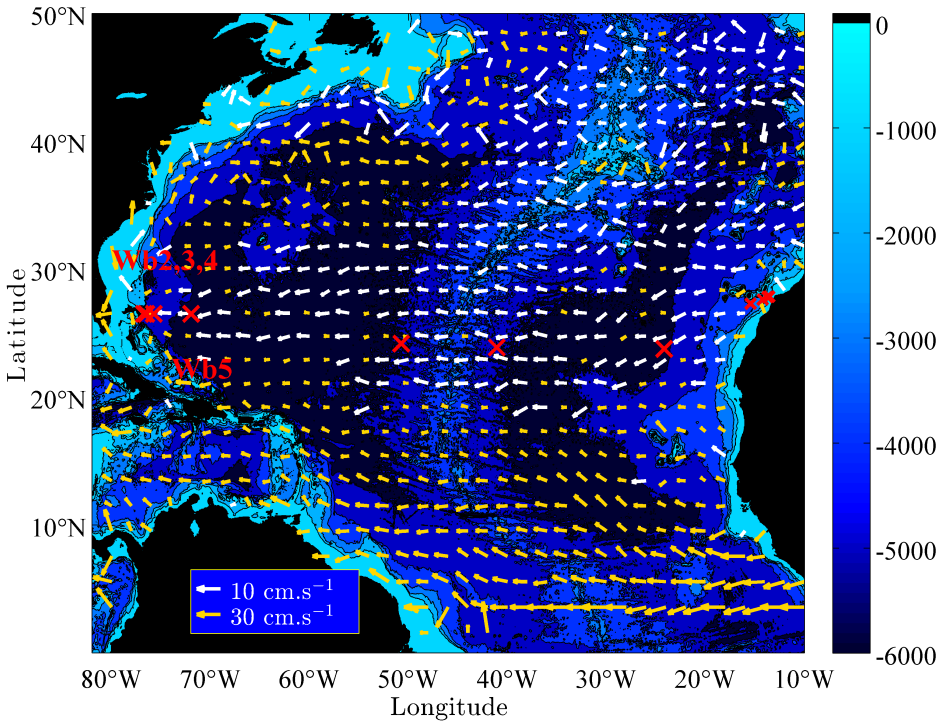

Figure 2.2: Speed and direction (arrows) of surface propagations in the North Atlantic inferred from time-space maximum lagged-correlation of sea surface height anomaly from Aviso between March 2004 to January 2011 over bathymetry in metres (colourscale). The Rapid array mooring positions are indicated in red crosses with the western boundary moorings Wb2, Wb3, Wb4 and Wb5.

In theory, with the presence of strong mean flow, generally aligned with topographic

features at the western boundary, eddies can be advected by mean currents. In the absence of strong mean flow, eddies and Rossby waves are expected to propagate to the west due to the latitudinal gradient of Earth's rotation (Chelton et al., 2011). Three main patterns emerge from Fig. 2.2 based mostly on the latitudinal variability: the first one in the subtropics equatorward of 20°N, then at mid-latitudes between 20 and 30°N and poleward of 30°N. The subtropics are characterised by fast westward propagating anomalies originating at the eastern boundary and slightly deflected northwestward when approaching the western boundary. This deflection may come mostly from the North Brazil Current orientated to the northwest along the South American coast and which creates rings that travel to the Lesser Antilles (Fratantoni and Richardson, 2006). In the midlatitudes, westward propagating signals are observed across the full Atlantic basin extending to the western mooring array without being deflected at the boundary. The Gulf Stream is restricted in these latitudes to the Florida Strait and propagating anomalies are near purely westward towards Wb5-Wb2. The phase speed dependence on β (β-effect) is apparent in decreasing speeds when moving from sub-tropics to mid-latitudes. In the latitudinal band from 30 to 40°N the eastern basin is characterised by westward propagating anomalies similar to the pattern at mid-latitudes but with widely varying directions particularly on the eastern side of the MAR. The influence of the Gulf Stream is seen in the western basin with propagating speeds higher than in the eastern basin and than at midlatitudes for similar longitudes. This location is comparable to the area of maximum eddy kinetic energy inferred from surface geostrophic velocities (Brachet et al., 2004) and may characterise creation and dispersion of Gulf Stream rings.

Having confirmed the presence of near purely westward propagating signals particularly relevant at mid-latitudes, the focus can now be on 26.5°N. SSHA are displayed in a Hovmoller plot with DHA added on the four moorings Wb2, Wb3, Wb4 and Wb5 (Fig. 2.3). This representation helps to interpret westward propagating features already observed at each mooring for the first year of measurements in SSHA and DHA in Bryden et al. (2009). High amplitudes of SSHA are found at the eastern boundary which propagate to the west, however, the highest amplitudes of the eastern basin are restricted to the eastern boundary. Overall the western basin contains larger SSHA amplitudes and faster speeds of propagating signal with the basin separation located at the MAR around 40–50°W. Additional variability also appears at the western boundary close to 65°W with maximum amplitudes before decreasing close to the boundary at 75°W. A first link can be established between surface and interior signals as expected from the decomposition of SSHA in dynamic height and bottom pressure (Gill and Niiler, 1973). The correlations of SSHA with DHA are 0.89, 0.8 and 0.64 at Wb5, Wb3 and Wb2 respectively (Fig. 2.3a). The decreased correlation indicates that signals at the surface are less coherent with subsurface integrated signals at Wb2 than at Wb5. In spite of the correlation decrease, the correlation is still significant at Wb2 sustaining the hypothesis that a meridional flow inferred from the geostrophic calculation should be affected by eddies and Rossby waves.

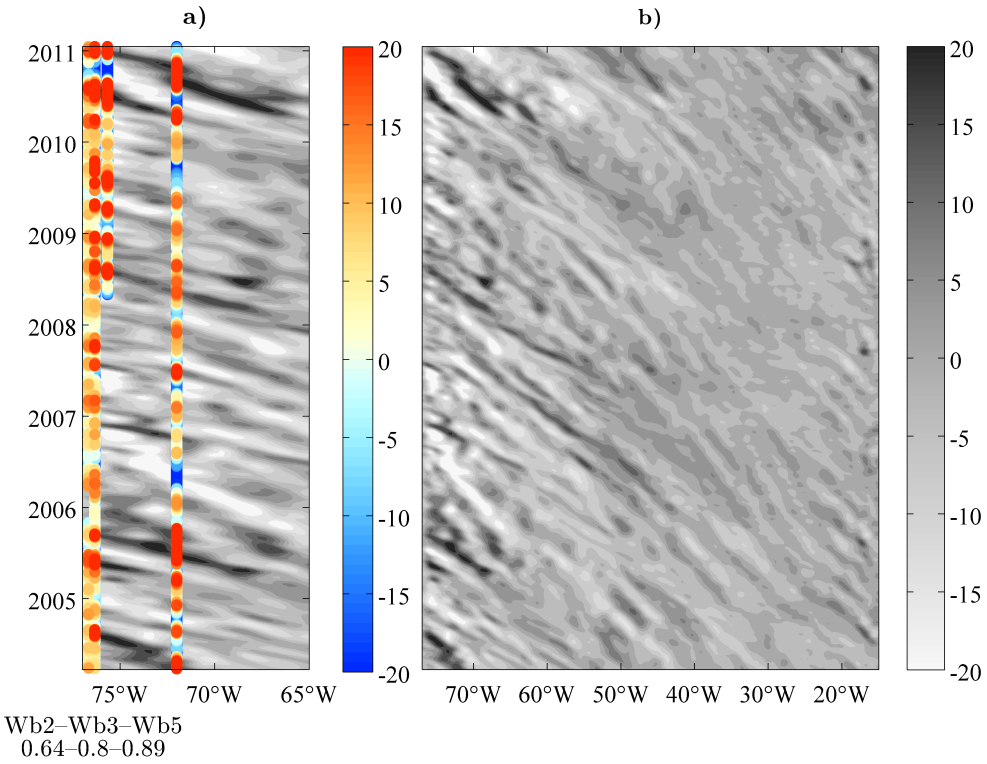

Figure 2.3: Dynamic height integrated from the bottom to 200 dbar (colors, dynamic cm) and sea surface height (grey, cm) anomalies at 26.5°N for (a) the westernmost section (77 to 65°W) with the four moorings of the western array Wb2, Wb3, Wb4 and Wb5; (b) the entire North Atlantic basin at 26.5°N from 77 to 14°W. The correlation between DHA and SSHA is indicated below Wb2, Wb3 and Wb5.

2.3.2 Spectra of sea surface height

The mooring array will be used to study a representation of the vertical structure and to define the frequency of westward propagating signals. The zonal wavelength of these signals can be added to the analysis using a 2D spectra of SSHA observed at one latitude in the Hovmoller plot (Fig. 2.3). This method has been used since the advent of altimetry to study Rossby waves (Cipollini et al., 1997). For Rossby waves, the meridional wavelength is supposed to be large compared to the zonal wavelength (Chelton et al., 1996); this assumption is expressed by setting $l = 0$. In the case of propagating eddies that are assumed to be isotropic, their zonal wavelengths become relevant to understanding the zonal extent of these signals.

A 2D frequency/zonal wavenumber spectrum of SSHA (Fig. 2.4) is obtained at 26.5°N using the Welch's overlapped segment averaging (WOSA) method (Emery and Thomson, 2001). The WOSA is used with two-year blocks and 67% overlap. The SSHA timeseries runs from October 1992 to January 2011 and is interpolated to 26.5°N. The entire width of the North Atlantic basin is considered, extending from 77°W to 18°W.

To focus on the signal of interest with the strongest effect on the SSHA variance, the spectra is displayed in a variance-preserving form. To preserve variance in both dimensions, the spectra multiplied by the frequency and zonal wavelength is displayed versus the logarithm of the frequency and of the zonal wavelength.

The energy of SSHA is displayed in Fig. 2.4 along with the dispersion relations of the barotropic and first baroclinic mode (Eq. 2.2). To visualise the peak in each dimension separately, the variance integrated over every zonal wavenumber and frequency are also displayed. A main peak of energy appears with wavelengths in the range 350–800 km and with periods of 80–200 days. A phase speed range is inferred from these wavelengths and periods of 4.6 cm s^{-1} for the long period and long wavelength limit of the main peak and 5.1 cm s^{-1} for the short period and small wavelength limit. The energy located in the low frequency and low wavenumber portion of the spectra indicates a phase speed in agreement with the dispersion relation of the first baroclinic mode Rossby wave. In these limits, i.e. above the cutoff period ($2\pi/w_{1\_max}$= 151 days) and wavelength ($2\pi/\lambda_{max}$= 295 km), the dispersion relation is nondispersive. Above these cutoffs, the energy is no longer in agreement with the dispersion relation and the features propagate faster than the linear first mode theory. Since the ridge of energy extends to the barotropic dispersion relation for high frequency and large wavenumber, this dispersive part of the spectrum may represent coupled baroclinic and barotropic motions.

2.3.3 Interior variability

Profiles of temperature anomalies from January 2010 to April 2011 relative to the temporal average at each depth and isopycnals of neutral density are displayed for the four moorings in the top 1100 m and for deeper waters in Fig. 2.5. At Wb5, some temperature and density anomalies seem to propagate mainly to the west and to occupy the full water column. Their vertical extent is reduced as they approach the boundary to become only coherent in the top 1200 m at 20 km from the shore. An anomaly of shallower isopycnals at Wb5 starting in mid-May 2010 arrives at Wb4 in September and within few days at Wb3 and Wb2 if we assume a westward propagating direction. The amplitudes of hydrographic anomalies are maximal at Wb4 and decrease when approaching the boundary in the last 110 km off the coast to Wb2. Propagating signals have a period of approximately three months at Wb5 varying from one to four months and they occupy the boundary at Wb2 for shorter periods. These anomalies are observed below the thermocline to 4000 m at Wb5 and to 3000 m at Wb4. They are not seen deeper than 1200 m at Wb2; below this level hydrographic anomalies are subject to strong variability almost coherent in the bottommost 2500 m. The deep variability at Wb2 is characterised by higher frequency than its shallower variability or than the deep variability at Wb5 away from the western boundary.

The average of absolute isopycnal displacements in the thermocline from the surface

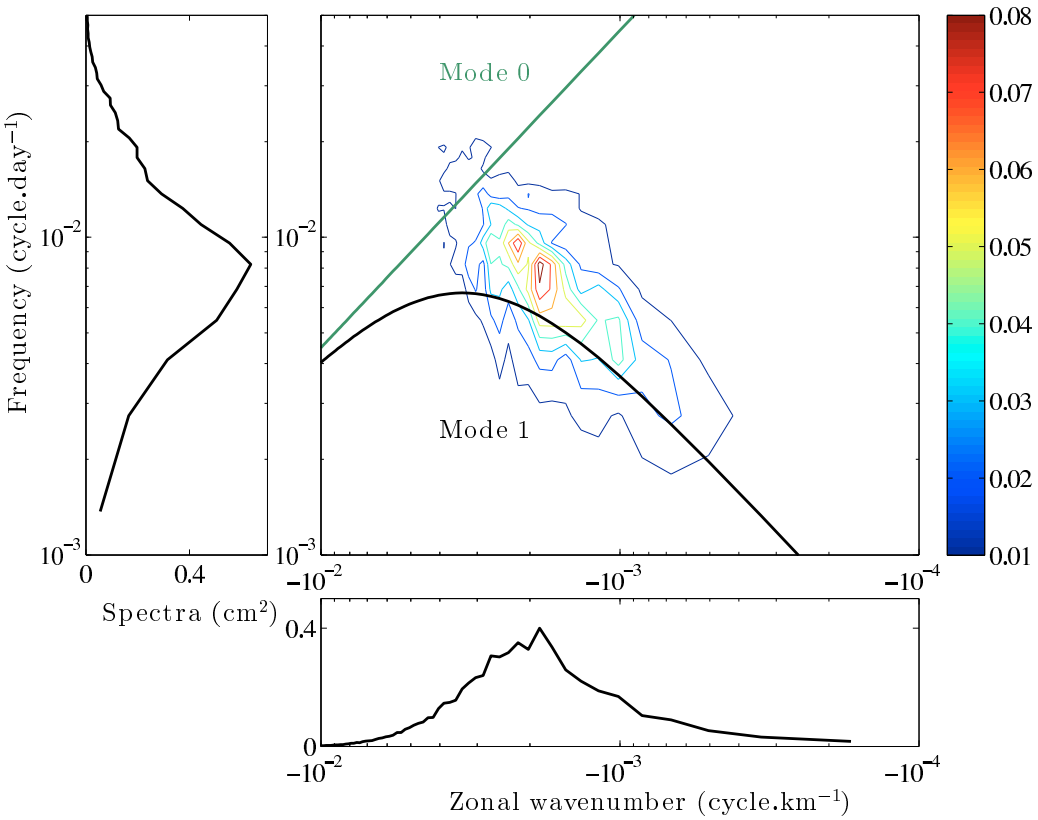

Figure 2.4: Frequency-zonal wavenumber variance-preserving spectra (middle) of sea surface height anomaly in the western North Atlantic basin (77 to 18°W) at 26.5°N from October 1992 to January 2011 using the Welch's overlapped segment averaging method with a 67% overlap. The dispersion relations of the barotropic and first baroclinic mode based on the linear theory are added (Eq. 2.2 with l=0). The 2D spectra is shown integrated over zonal wavenumber (left) and frequency (bottom).

to 1000 m is 35 m at Wb4 and is reduced to 15 m at Wb2. The maximal absolute values are within 200–300 m at Wb4 and 100–150 m at Wb2. A band of reduced temperature anomalies is observed in all moorings around 300–500 m corresponding to the depth of 18°C Mode Water. Despite the presence of this band, propagating anomalies are mostly coherent in the top 1000 m. In the simplified depiction of eddies through isopycnal displacements of the seasonal and permanent thermocline (McGillicuddy et al., 2007), the signals are mostly denoted by 'cyclone' or 'anticyclone', meaning both isopycnals have coherent displacements, instead of a Mode-water eddy with isopycnal displacements opposite in direction. The amplitude of the anomalies are reduced in the shallowest 150 m where other ocean dynamics may be present due to atmospheric buoyancy flux, wind effects and submesoscale dynamics. This reduction in amplitude is particularly evident at the boundary (Wb2 and Wb3) where signals shallower than 150 m evolve independently to the rest of the thermocline.

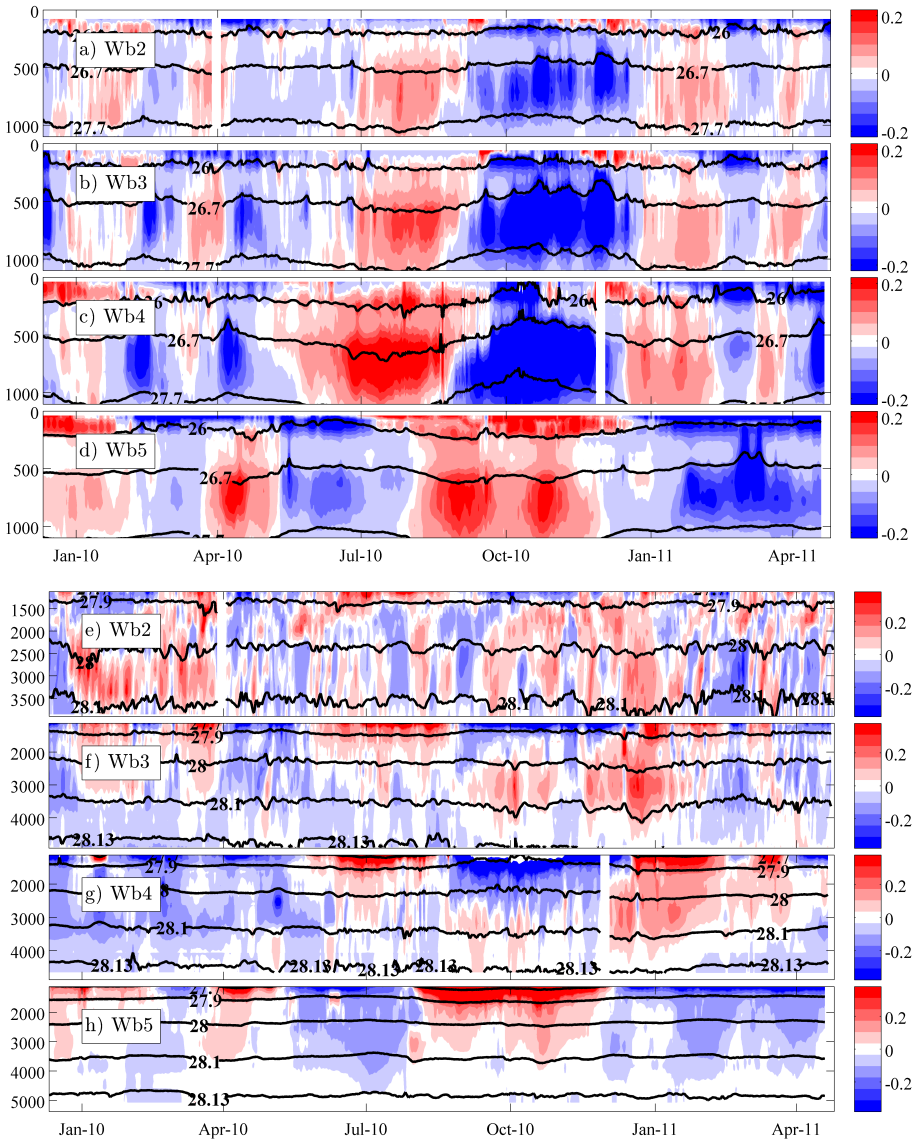

Figure 2.5: Temperature anomalies relative to the temporal average at Wb2, Wb3, Wb4 and Wb5 (top to bottom) in colours and isopycnals of neutral density in black for the shallow (top four panels) and deep water column (bottom four panels) from January 2010 to April 2011.

2.3.4 Link between surface and interior variability

Temperature and isopycnal timeseries (Fig. 2.5) indicate the presence of propagating signals for several months. To obtain accurate estimates of these timescales, autocorrelation functions of SSHA and isopycnal displacements are calculated (Fig. 2.6). Decorrelation and integral timescales can then be inferred. Autocorrelation functions should help to detect eddies and Rossby waves, assuming a presence of these signals in the range of several weeks to several months. The decorrelation timescales or first-zero crossings give lags at which SSHA or ζ becomes uncorrelated. The integral timescale (Eq. 2.3), used in the degree of freedom, is also defined from the autocorrelation function.

At Wb5 (Fig. 2.6 right) the decorrelation timescale increases gradually from the surface to the bottom in the range of 50–90 days. The gradual increase supports previous observations (Fig. 2.5) of the full water column affected by westward propagating processes. The reduced autocorrelation amplitude deeper than 2000 m is characterised by smaller integral timescales. Decorrelation timescales shorten at Wb3 and Wb2 relative to Wb5 (Fig. 2.6 middle and left) in the range 40–50 days and 30–50 days in the top 3000 m and 1000 m respectively. They are associated with enhanced autocorretation amplitudes and constant integral timescales. At Wb3 below 3000 m first-zero crossings increase to 70–100 days and integral timescales also lengthen. The deep decorrelation timescale at Wb3 may distinguish a different dynamic than the one reflected in the shallow decorrelation timescale. At Wb2 a similar depth separation between shallow and deep water affected by varying dynamics seems to appear. This separation at 1500 m is shallower than at Wb3 and is marked by a first-zero crossing maximum above the minimum from 1500 to 3900 m. The 20-day deep water integral timescale at Wb2 characterises rapid variations coherent in the bottommost 2500 m as previously described in Fig. 2.5.

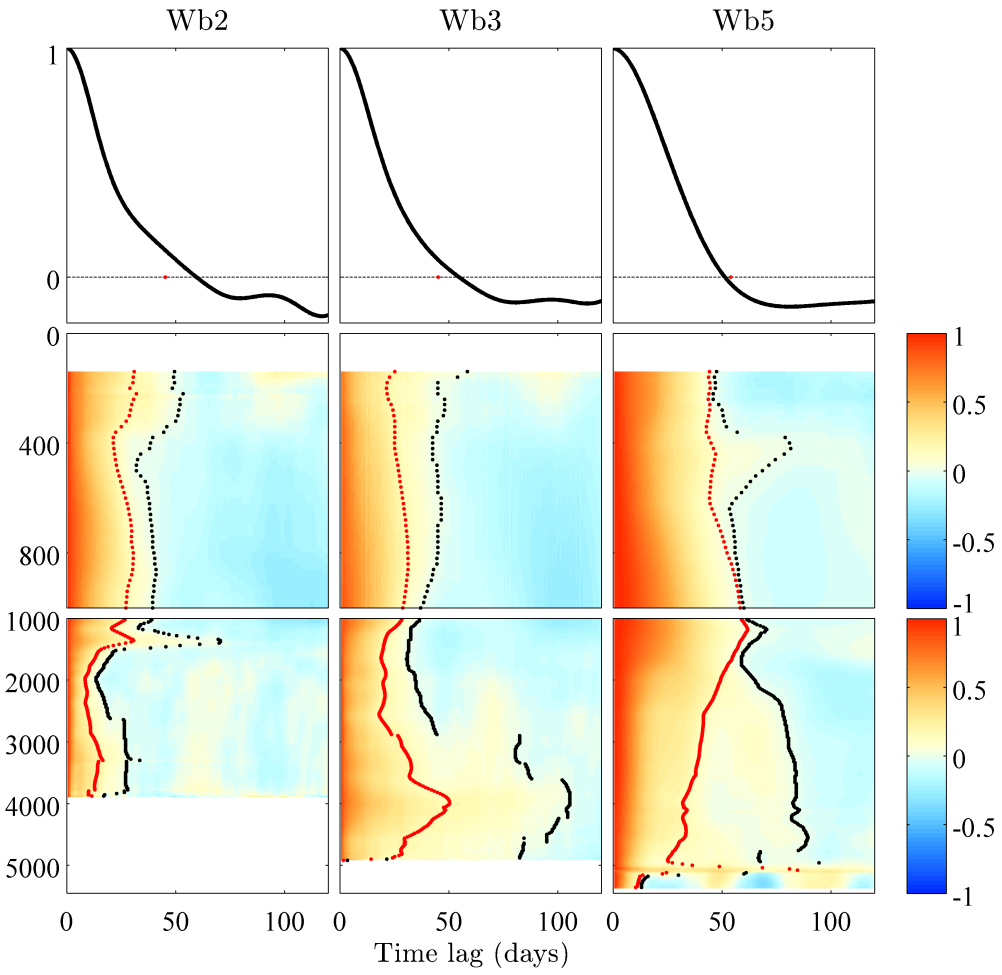

Figure 2.6: Autocorrelation function of SSHA (top panels), shallow (middle) and deep (bottom) isopycnal displacements from April 2004 to January 2011 at each depth for Wb2, Wb3 and Wb5. The first zero-crossing (black points) and integral timescales (red points) are added.

The presence of Mode Water seen in temperature anomalies (Fig. 2.5) is visible in the peak of first-zero crossing autocorrelation at 400 m at Wb5 (Fig. 2.6 right). Due to relatively low autocorrelation, this peak is no longer present in integral timescales and is also not visible at Wb2 and Wb3 (Fig. 2.6 left and middle). Decorrelation and integral timescales at Wb5 of SSHA are in agreement with ζ timescales in the top 1000 m. The correspondence is still true at Wb2 and Wb3 for the first-zero crossing, however the integral timescale is higher for SSHA. Conservative confidence levels for the correlation of SSHA and ζ will be kept by retaining the integral timescales of ζ.

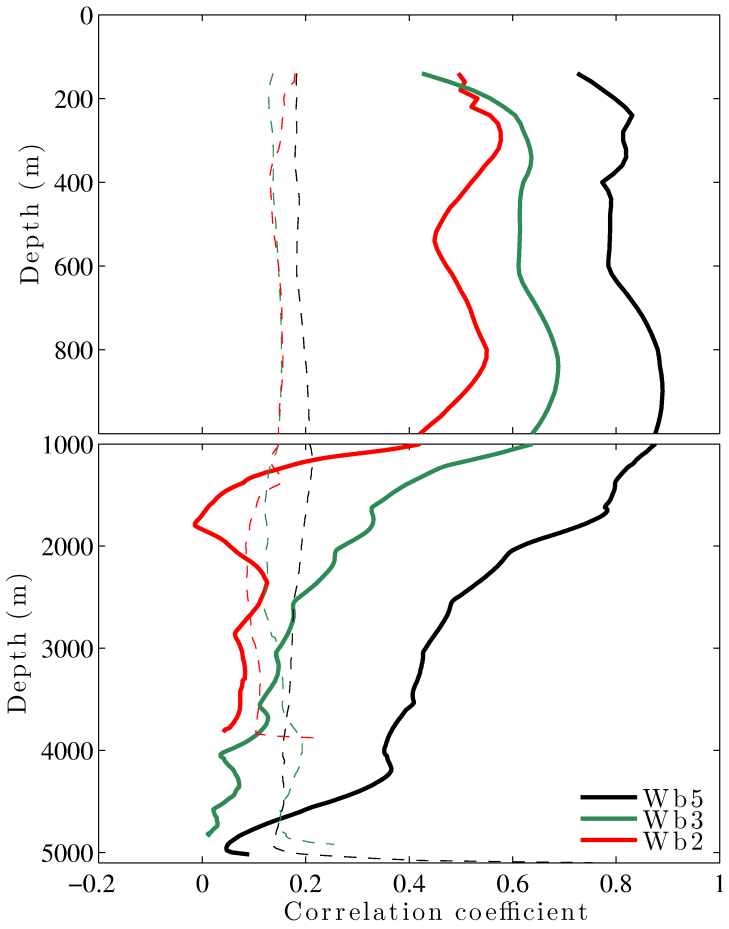

Figure 2.7: Correlation coefficient between SSHA and isopycnal displacements at Wb2 (red), Wb3 (green) and Wb5 (black). The 95% confidence intervals are indicated as dashed lines.

The depth to which sea surface variations are representative of the subsurface variability can be localized through the correlation coefficient of isopycnal displacements and SSHA (Fig. 2.7). Larger integral timescales (Fig. 2.6) are associated with less degrees of freedom and higher significance thresholds. At Wb5 the correlation is significant across the full water column shallower than 4500 m with a decrease in the coefficient below 1000 m and varies from 0.7 to 0.9 in the top 1000 m. At Wb3 and Wb2 the correlation is still significant above 1000 m but is lower than at Wb5 with values of 0.6 and 0.5 at Wb3 and Wb2, respectively. Below 1000 m at the western boundary, the correlation

decreases below the level of significance at Wb3 deeper than 3000 m. At Wb2 the decrease is more abrupt and the significance threshold is crossed around 1200 m. These deep low correlations at Wb3 and especially at Wb2 are consistent with observations of density anomalies coherent in the bottommost 2500 m (Fig. 2.5) and associated with the smallest decorrelation timescale (Fig. 2.6).

2.4 Decomposition in normal modes

To describe the vertical structure of propagating signals, a normal mode decomposition (Gill, 1982) is used. The main requirement to implement this method rests on the depiction of large-scale oceanic processes with horizontal scales larger than their vertical scales. It then becomes possible to do a separation of variables and to allocate a set of fixed vertical structures to describe propagating anomalies. These vertical structures, the normal modes, form a set of orthogonal functions. Applying the decomposition to several years of hydrographic data will allow us to study the frequency content of each mode. It will become possible to relate the frequency spectra of normal modes and SSHA and to follow propagating features between adjacent moorings through coherence spectra. The effect of these anomalies on the meridional geostrophic transport will be evaluated in the next chapter.

2.4.1 Buoyancy frequency at each mooring

The vertical structure of each baroclinic mode is extracted from the buoyancy frequency profile N. N is calculated at each mooring (Wb2, Wb3 and Wb5) using mean temperature and salinity profiles from 2004 to 2011 and gridded every 20 dbar. The N profile is obtained at mid-depth by differentiating adjacent potential densities referenced at mid-depth

$$N(z)^2 = -\frac{g}{\rho_0}\frac{\partial \overline{\rho}}{\partial z} \ , \tag{2.4}$$

where g is the acceleration due to gravity, ρ_0 is a reference density and the overbar indicates time mean. The buoyancy frequency profiles are displayed along with mean isotherms in Fig. 2.1. They are characteristic of the western North Atlantic with two peaks of strong stratification in the seasonal and main pycnocline (Siegel et al., 1999). The shallow peak (around 200 m) and the deeper peak (500–1000 m) have buoyancy frequencies of 0.008 s^{-1} and 0.005 s^{-1}, respectively. The deeper peak is shallower at the boundary and its vertical extent reduces to 500–900 m. The isopycnals around these depths correspondingly shoal as they approach the boundary from about 70°W. A stratification minimum is present between these two maxima around 300–400 m. This minimum is related to the presence of 18°C water occurring throughout the western subtropical region (Talley et al., 2011).

2.4.2 Normal modes of isopycnal displacements

The Sturm-Liouville system

The quasi-geostrophic formalism (Cushman-Roisin and Beckers, 2011) is used to describe small deviations from the geostrophic approximation. Based on the linear quasi-geostrophic potential vorticity (QG PV) equation, isopycnal displacements due to eddies and Rossby waves are decomposed as a sum of modal solutions to the QG PV equation as described in Chelton et al. (1998). Each solution represents a different baroclinic mode. The normal mode decomposition of isopycnal displacements (ζ) allows the separation of ζ into two variables for each mode (m): the modal amplitude ($\hat{\zeta}$) and the modal function (F_m) depending on time and depth respectively

$$\zeta(z,t) = \sum_{m=1}^{M} \hat{\zeta}_m(t) F_m(z) \ . \tag{2.5}$$

The QG PV equation can be separated into a system of two equations depending either on time or depth. One equation defines the modal structure of each mode given the buoyancy frequency profile

$$\frac{d^2 F_m(z)}{dz^2} + \frac{N^2(z)}{c_m^2} F_m(z) = 0 \ . \tag{2.6}$$

The eigenvalue c_m of this ordinary differential equation is the phase speed of mode-m gravity waves associated with the eigenfunction F_m. A flat bottom and the rigid lid approximation are considered as boundary conditions.

$$F_m = 0 \text{ at } z = 0, -H, \tag{2.7}$$

these conditions form a Sturm-Liouville system along with Eq. 2.6. Eigenfunctions which are obtained from the Sturm-Liouville equation (Eq. 2.6) and the boundary conditions are displayed in Fig. 2.1 for the first three baroclinic modes at Wb2, Wb3 and Wb5. The depth of the deep zero crossing of the 3rd mode and of the maximum amplitude of the 1st mode varies between locations. The depth of the 1st mode maximum ranges from 980 m at Wb2 to 1120 m at Wb3 and 1240 m at Wb5. The main factor influencing the depth of the maximum is the amplification of the shallower peak of the buoyancy frequency and the 1000 m change in water depth between Wb2 and Wb3. The mode structure diverges away from a sinusoidal profile, found with a constant stratification, when the shallow peak of stratification intensifies. The depth of the deep zero-crossing of the 3rd mode, 1060, 1460 and 1660 m for Wb2, Wb3 and Wb5, also becomes shallower closer to the coast. The hypothesis of no mean currents is made in the classic normal mode decomposition. This hypothesis along with the boundary conditions are not expected in the ocean particularly at the western boundary for Wb2 and Wb3 where intensified boundary currents and topographic gradients can be significant. Bearing these restrictions in mind, the normal mode decomposition seems to give a good representation of isopycnal variability and will be useful to relate the variability between various moorings.

An essential property of the modal decomposition (Gill, 1982) is the orthonormality of the normal modes weighted by the buoyancy frequency.

$$\int_{-H}^{0} N^2 F_m(z) F_n(z) dz = \delta_{mn} \text{ and } \quad \delta_{mn} = \begin{cases} 1 & \text{if} \quad m = n \\ 0 & \text{if} \quad m \neq n \end{cases} \tag{2.8}$$

The normal modes of each mooring are therefore normalised to respect the orthonormality property. The modal decomposition of isopycnal displacements can be equivalently applied to velocity and pressure measurements as described in Wunsch (1997) and Szuts et al. (2012) respectively. The eigenfunctions of ζ are related to the vertical derivatives of the velocity eigenfunctions. For the first mode the zero-crossing of the velocity eigenfunction corresponds to the maxima of the isopycnal displacements eigenfunction. Normal modes of isopycnal displacements are forced to zero at the boundaries (Eq. 2.7) as opposed to normal modes of velocity and pressure which are maximal at the surface. One limitation with normal modes of isopycnal displacements comes from the restriction to define the barotropic mode. A ζ barotropic mode derived from the vertical gradient of the velocity barotropic mode will not respect the orthonormality property and limit the definition of modal amplitudes and their associated variance explained as defined in the next section. The present study on the vertical structure of eddies and Rossby waves is focusing on baroclinic signals as opposed to a purely fast barotropic motion. The peak in correlation between SSHA and ζ was found around 700 to 900 m at Wb2, Wb3 and Wb5 (Fig. 2.7) along with a reduced correlation around 200 m at Wb2. The increased correlation at the base of the thermocline supports the assumption that westward propagating features are most likely represented by baroclinic modes. The upper limit of the normal modes is chosen at 140 m due to data availability. This limit will remove the atmospheric effect and should help to focus on the propagating signals of interest. Additional high frequency shallow processes are believed to be more frequent at the boundary as seen with current meters (Johns et al., 2008); the upper limit should reduce their effect.

The internal Rossby radius of deformation defines the horizontal scale of a perturbed system at which the rotation and buoyancy effects become comparable (Gill, 1982). This variable is present in the linear Rossby wave dispersion relation and in the phase speed of long Rossby waves. The Rossby radius can be obtained from the eigenvalues of the Sturm-Liouville system for each baroclinic mode (c_m/f). The Rossby radius of the first baroclinic mode at Wb2, Wb3 and Wb5 is 44, 46 and 47 km, respectively. The value found at Wb5 is mostly representative of the basin interior away from boundary currents and topographic features; McWilliams and Flierl (1976) found a similar first baroclinic Rossby radius in the Sargasso Sea using the MODE array. The radius was also approximated in Chelton et al. (1998) through the depth-integrated buoyancy frequency rendering its dependence on both the thermocline depth and the water depth apparent at one latitude. These effects reduce the radius when approaching the boundary from

Wb5 to Wb2 with the latter effect being stronger because the mean stratification was not observed to strongly differ between these two moorings.

Modal amplitudes of isopycnal displacements

Modal amplitude timeseries are calculated from the normalised vertical structure of the normal modes (Gill, 1982) applying the orthonormality property (Eq. 2.8) to the ζ decomposition (Eq. 2.5)

$$\hat{\zeta}_m(t) = \int_{-H}^{0} N^2(z)\zeta(z,t)F_m(z)dz. \tag{2.9}$$

This method is equivalent to a multivariate least-square fitting to obtain the amplitude of each mode. Modal amplitudes can equivalently be written in matrix form by minimising the residual squares of the ζ decomposition (Eq. 2.5). The present method of modal fitting varies from the Gauss-Markov method used in Wunsch (1997) and Szuts et al. (2012) which in their cases enabled them to formulate uncertainty of their modal amplitudes. The Gauss-Markov estimates rely on the a priori partitioning of the energy between the different modes. In the present case no a priori assumption is made and based on the energy partitioning from Parseval's theorem and with the good agreement between this methodology and the WKBJ decomposition, we believe that the present decomposition captures most of the signal seen in isopycnal displacements.

The percentage of variance explained by each mode can be estimated based on Parseval's theorem as described in Kundu et al. (1975). Starting from the ζ decomposition (Eq. 2.5) times the buoyancy frequency and integrating the square with depths we obtain

$$\int_{-H}^{0} (N(z)\zeta(z,t))^2 dz = \int_{-H}^{0} (\sum_{m=1}^{M} N(z)\hat{\zeta_m}(t)F_m(z))^2 dz. \tag{2.10}$$

The above equation can be transformed according to the orthonormality property. The orthonormality property is more strictly imposed by the construction of the normal modes on a 20 dbar grid as opposed to using only the number of instruments in the vertical column

$$\int_{-H}^{0} N^2(z)\zeta^2(z,t)dz = \sum_{m=1}^{M} \hat{\zeta_m}^2(t). \tag{2.11}$$

This equation provides the instantaneous depth-integrated energy as the sum of the contribution of each mode. It becomes possible to evaluate the contribution of each baroclinic mode to the total energy. This energy represents the depth-integrated available potential energy per unit area (APE)

$$APE = \frac{1}{2}\rho_0 \int_{-H}^{0} N^2(z)\zeta^2(z,t)dz. \tag{2.12}$$

Isopycnal displacements are calculated relative to their mean depths at each mooring, the energy extracted from these isopycnal displacements is an anomaly of available potential energy which could be partly attributed to westward propagating features or local anomalies. This quantity differs from the available potential energy seen in a longitudinal section and relative to the mean zonal depth of isopycnals which varies for each mooring. Parseval's theorem is applied instantaneously because the transformation from Eq. 2.10 to Eq. 2.11 is only true for each time interval and does not necessarily hold over the entire timeseries. This arises because modal amplitudes may not be uncorrelated in time between each other as phase-locking can exist between various modes (Wunsch, 1997). In theory, normal modes should represent propagating anomalies with varying and decreasing phase speed as the baroclinic mode number increases. However some signal may be present in adjacent normal modes and may not be expected to propagate according to the theory. A coherence study of modal amplitudes between neighbouring moorings in the next section will detect where true propagating signals is believed to happen.

By applying Parseval's theorem to the modal amplitude, it is possible to obtain a first estimate of how good the fit of the modal decomposition is in reconstructing the energy contained in isopycnal displacements (Fig. 2.8). By comparing the total energy level between the three moorings, it appears that Wb5 and Wb3 have similar average energy (1214 and 1205 J/m^2) more important than at Wb2 (891 J/m^2). In spite of this similitude, Wb3 and Wb2 contain strong high-frequency variability lasting less than a month and not observed at Wb5. In addition to the high frequency variability, the total energy at Wb2 and Wb3 is still affected by signals with longer periods than a month which seem to prevail at Wb5.

The individual instantaneous contribution of the first mode to the total energy is displayed in Fig. 2.8 and the time-mean variance explained of the first five modes is quantified in Fig. 2.9 and Table 2.2. The first mode at Wb5 recovers most of the energy and explains 52% of the total variance. Comparing mode-1 and total energy timeseries shows that the first mode is affected by signals of similar frequency as the total energy. Most of the total energy is captured by the first mode for events with amplitudes larger than 2000 J/m^2 and this observation is not true for events of smaller amplitude. At the boundary, the mode-1 signal becomes less important than at Wb5 and represents a smaller fraction of the total variance, decreasing to 30 and 15% at Wb3 and Wb2 respectively. At Wb3 the events with the largest amount of energy are still well captured by the first mode. Events of similar frequency are seen in the first mode at Wb2 but they capture a reduced fraction of the total energy. Considering the first three modes instead of the first mode only provides a significant increased variance explained at Wb2. The timeseries of the first three modes is affected by higher frequency variability than mode 1 at Wb2. This supports previous observations that the deep section of Wb2 is characterised by smallest integral timescales (Fig 2.6). A strong deep temperature

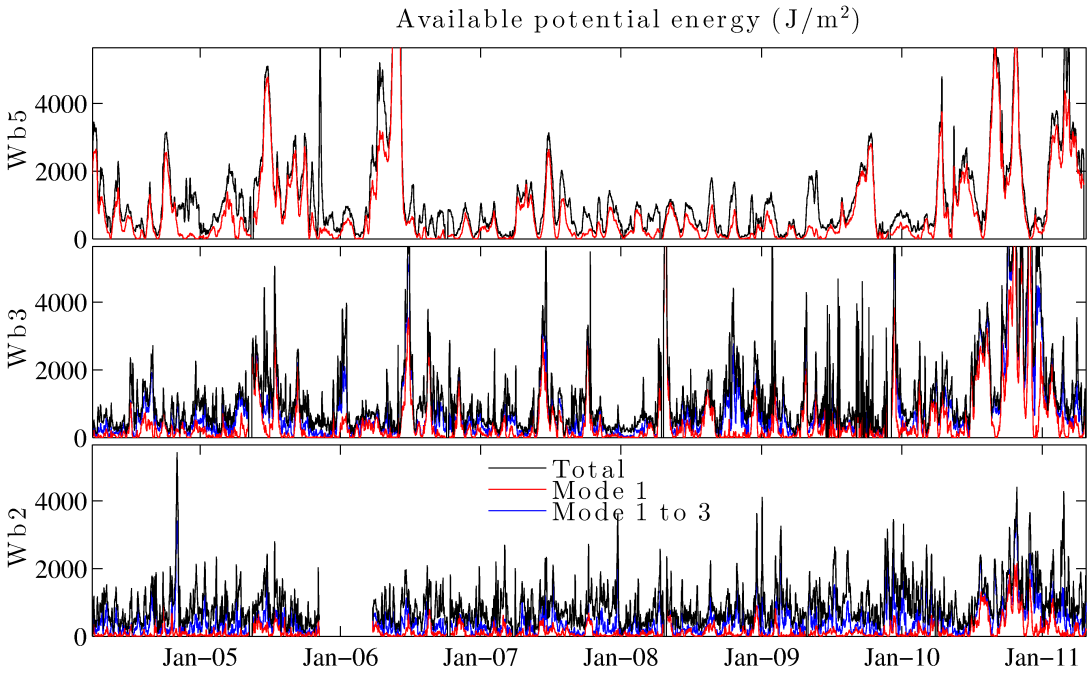

Figure 2.8: Available potential energy per unit area (J/m^2) at Wb5, Wb3 and Wb2 of the observed isopycnal displacements (black), the first baroclinic mode (red) and the first three baroclinic modes (blue).

anomaly below 2000 m was observed at Wb2 in November 2004 in Cunningham et al. (2007) and Johns et al. (2008). This anomaly is seen in the total energy at Wb2 and in the energy of the first three modes but not in the energy of the first mode supporting the fact that the deep anomaly is well captured by the third mode. The percentage of variance explained by the first three modes is 45%, 60% and 72% at Wb2, Wb3 and Wb5 respectively (Table 2.2). Calculating the variance and the cumulative variance explained by the first 20 modes (Fig. 2.9) demonstrates the fact that more modes are necessary to recover the total variance at Wb2 than at Wb5. The modal decomposition with 20 modes improves the variance explained to 95% of the total energy at all the moorings including Wb2 (Fig. 2.9).

As observed from the mode structure (Fig. 2.1) the first baroclinic mode intensifies at the base of the thermocline within 200 m of 1000 m for the three moorings. This depth corresponds approximately to the depth of maximum correlation coefficients between isopycnal displacements and SSHA observed to increase from the surface (Fig. 2.7). Isopycnals displacements at each mooring coherent within the top 1000 m are therefore more likely to be represented by the 1st baroclinic mode than higher baroclinic modes. This mode must capture most of the vertically coherent variability localised in the shallowest 1000 m and observed to propagate between Wb2, Wb3 and Wb5 (Fig. 2.5). In the ocean interior at Wb5, propagating features are not expected to be influenced by strong topography and mean currents. This may explain the vertical coherence of density anomalies over the full water column (Fig. 2.5) associated with significant correlation

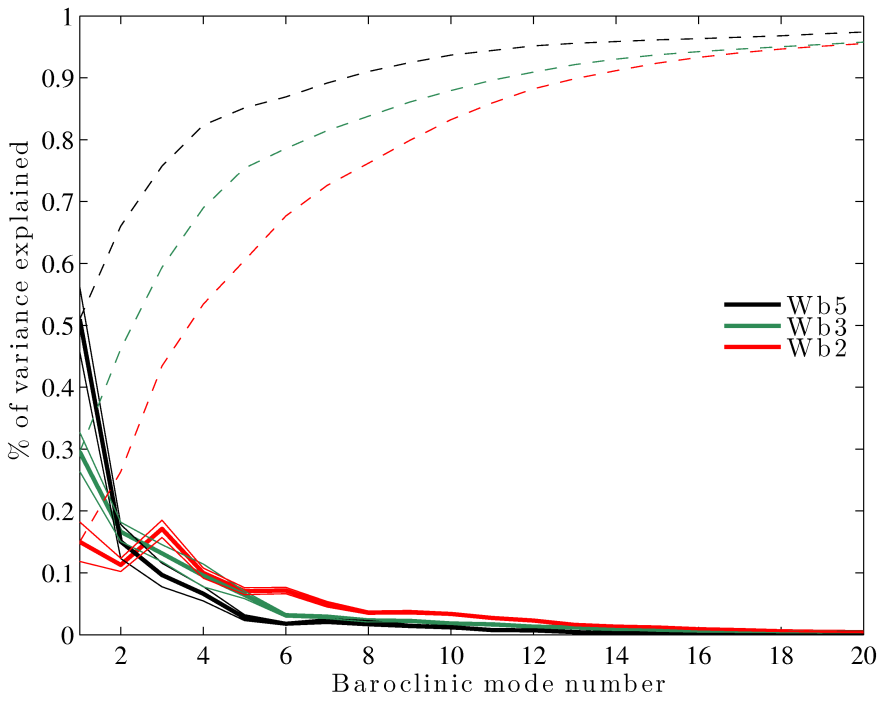

Figure 2.9: Percentage (lines) and cumulative percentage (dashed) of variance explained of the first 20 baroclinic modes of isopycnal displacements at Wb2 (red), Wb3 (green) and Wb5 (black). 95% confidence intervals are calculated from the Student's t-distribution.

with SSHA (Fig. 2.7) and with a strong representation of the variance explained by the first mode (Table 2.2). At the boundary (moorings Wb2 and Wb3), the 1st mode still contains some energy but higher baroclinic modes are necessary to resolve the additional deep water variability represented by more complex vertical structures. The origins of this added variability may be multiple and the presence of the steep topographic wall and strong mean currents in this region should account for some of this variability. The topography and mean currents may interact between each other and also interact with westward propagating anomalies. These questions will be developed in the discussion and one aspect of the interaction of westward propagating anomalies with the topography will be addressed in the last chapter.

Baroclinic mode	Wb2	Wb3	Wb5	Vertical wavelength	Wb2	Wb3	Wb5
1	15%	30%	51%	2*H	16% (0.99)	30% (1)	54% (1)
2	11%	17%	15%	(2*H)/2	13% (0.98)	17% (0.99)	15% (0.97)
3	17%	13%	10%	(2*H)/3	13% (0.98)	12% (0.98)	9% (0.87)
4	10%	10%	7%	(2*H)/4	11% (0.99)	11% (0.99)	6% (0.93)
5	7%	6%	3%	(2*H)/5	8% (0.99)	6% (0.96)	4% (0.86)

Table 2.2: Percentage of variance explained for the first five baroclinic mode used in the modal decomposition and for the first vertical wavelength depending on the water depth (H) used in the WKBJ method. Correlation coefficient between modal amplitudes and WKBJ coefficients are indicated in brackets.

2.4.3 The WKBJ method

Another method to describe the vertical structure of propagating signals is to account for the variation of stratification before analysing isopycnal displacements. The aim of this section is to support the methodology of the modal decomposition by using a different methodology which may confirm the results already found. The WKBJ (Wentzel-Kramers-Brillouin-Jeffreys) analysis is used to transform velocities and isopycnal displacements into a space of constant stratification. This method is particularly useful for the spectral analysis of internal waves which are strongly influenced by the stratification as depicted in Leaman and Sanford (1975). The WKBJ method is also relevant in the present study to depict the vertical structure of westward propagating features. Isopycnal displacements are first scaled by the buoyancy frequency profile to adjust the thermocline strong stratification onto small displacements and the small stratification below the thermocline to the large displacements.

$$\zeta^\star(z,t) = \zeta\sqrt{\frac{N(z)}{N_0}} \tag{2.13}$$

A vertical mean buoyancy frequency N_0 is extracted from the profiles averaged over the full deployment (Eq. 2.4). The corresponding values are 2.2, 1.8 and 1.7×10^{-3} s^{-1} for Wb2, Wb3 and Wb5 respectively. The vertical coordinate is stretched by the stratification ($z^\star$)

$$z^\star = \int_z^0 \frac{N(z')}{N_0} dz'. \tag{2.14}$$

The transformed displacements on the stretched space $\zeta^\star(z^\star,t)$ are interpolated onto a regular 20 $s$dbar grid ($s$dbar are the stretched decibars). The vertical modes after this transformation become sinusoids. A spectral analysis can be performed on the vertical wavenumber of the displacements scaled and stretched and compared with the normal mode method. Transformed displacements are extended using zero-padding to match the vertical wavelength of mode 1 which is twice the water depth. To match the boundary conditions of zero displacements at the surface and bottom only the sine component of the fast Fourier transform is considered.

The correlation coefficients between modal amplitudes and WKBJ coefficients are displayed in Table 2.2 along with the variance explained of each vertical wavelength. The two methods are in good agreement at Wb2 and Wb3 providing a correlation between the amplitudes above 96% for the first five modes. At Wb5 the agreement is still good for the first two baroclinic modes but the correlation drops to 87 and 86% at mode 3 and 5. Comparing the percentage of variance explained also provides agreement between the two methods, the variance explained of the first five modes using the WKBJ method are not varying by more than 2% compared to the modal decomposition. At Wb2 the

agreement seems less good particularly on the third baroclinic mode with a variance of 13% using the WKBJ method as opposed to 17% for the mode and its lower limit of 15% within the confidence interval despite the elevated correlation of 0.98.

2.4.4 Spectral analysis of modal amplitudes

The temporal variability of propagating features was addressed using decorrelation and integral timescales of density anomalies. The integral timescale seems to evolve in the same range in the thermocline at Wb2, Wb3 and Wb5 but to differ between these moorings below the thermocline. The modal decomposition allows us to attribute a vertical structure to propagating features. The 1st mode is observed to explain a high percentage of variance in the ocean interior at Wb5 and to decrease gradually when approaching the boundary. Approaching the western boundary the 3rd baroclinic mode is becoming more significant. Despite the change in modal representation, the 1st mode is still expected to describe westward propagating features at Wb2 based on the significant correlation of density anomalies with SSHA in the top 1000 m (Fig. 2.7). The frequency content of modal amplitudes can be analysed and compared between each mooring (Fig. 2.10). Based on seven years of data the aim is mainly to capture the subannual and annual variability attributed to westward propagating features. The statistical significance of the peaks is increased by averaging spectral estimates using the weighted overlapped segment averaging (WOSA) method. Two-year blocks and a 67% overlap (Antoni and Schoukens, 2009) are chosen to concentrate on the timescales of interest and a Hanning window is applied in Fig. 2.10. The equivalent degrees of freedom is fourteen as inferred from the percentage of overlap and the window type in Percival and Walden (1993).

The decline of mode-1 energy in the mooring array, 500 km to 20 km offshore, is seen in the modal amplitude spectra (Fig. 2.10) as presented in the percentage of variance explained (table 2.2). At Wb5 (Fig. 2.10) a peak in mode 1 is observed above 80 days which is significant at the 95% level. The spectrum is red and levels off at periods above 200 days. At Wb3 and Wb2, 45 and 20 km from the boundary, a maximum is observed around 180 days. Variability rolls off at long periods (above 200 days) at both Wb2 and Wb3. On the third baroclinic mode, a distinctive period as found for the first mode across the three moorings or across the two boundary moorings (Wb2 and Wb3) is not defined. The decorrelation timescale in the thermocline of the three moorings was observed in a range of 40–60 days (Fig. 2.6). Assuming that this timescale is related to a propagating wave, its associated period will be 80–120 days. This period is within the frequency of the energy peak of the first mode in the three moorings and supports previous observations that this peak should characterise westward propagating features.

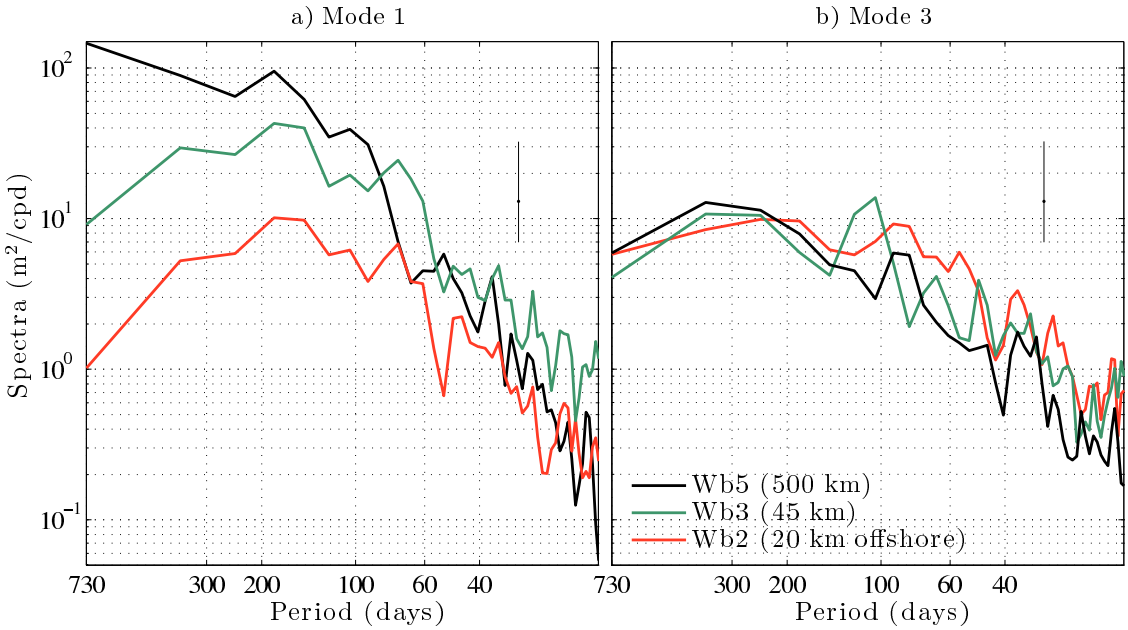

Figure 2.10: Power spectra of modal amplitudes of isopycnal displacement (m^2/cpd) for the first (a) and third (b) mode at Wb2 (red), Wb3 (green) and Wb5 (black) from March 2004 to January 2011. Vertical lines are the 95% confidence intervals.

2.5 Propagating features between moorings

Common energy at periods of 80-200 days is found in both mooring and altimetric measurements. To determine whether the surface and subsurface signal is truly propagating westward, a cross-spectra and coherence analysis between Wb2 and Wb3 and between Wb3 and Wb5 is performed. The phase is interpreted as the lag for purely westward/eastward propagating signals. Cross-spectral analysis is used to link the signal at varying frequencies of two timeseries, in our case located on two adjacent moorings. The cross-spectrum is the product of the Fourier transform of one timeseries with the complex conjugate of the Fourier transform of the other timeseries. The cross-spectrum contains the co-spectrum and quadrature spectrum which characterize the contribution to the in-phase and out of phase covariance respectively (Emery and Thomson, 2001). The coherence is the absolute value of the cross-spectra squared normalised by the energy in the individual spectra at each frequency. Coherence does not reflect the phase information. As a consequence, in interpreting coherence, we focus on peaks in coherence that are also present in the individual spectra, thereby only considering a high-degree of phase-locking at frequencies with significant energy.

The cross-spectra of modal amplitudes and SSHA in Fig. 2.11 are calculated with a block averaging using the WOSA method as presented for the study of modal amplitudes. The 95% confidence interval of the coherence of modal amplitudes is estimated from the equivalent degrees of freedom (Emery and Thomson, 2001). The cross-spectra of SSHA and of the first mode between Wb3 and Wb5 shows two peaks, one main peak from 150 to 250 days and another peak at 730 days. These two peaks are still seen in

the coherence with an additional peak at 60 days. The peak at 60 days does not reflect high energy in both spectra and in the cross-spectra so it is not considered further. The peak at 730 days was observed on the first mode of Wb5 but not at Wb3 (Fig. 2.10). Therefore this two-year signal is not likely to be important at the boundary. The peak at 150 to 250 days was observed in both SSHA and 1st mode spectra and this peak extends to 80 days in the coherence as also observed in the 1st mode spectra. The phase is however not clearly defined between 80 and 150 days but the positive phase between 150 and 250 days describes a westward propagating signal of constant phase speed. A constant phase speed of 7.3 cm s^{-1} is observed in the period range from 150 to 250 days with phases of 3 and 1.8 rad respectively.

In the Wb2-Wb3 section, the coherence of the first mode has two major peaks of positive phase at 110–180 days and at 80 days. The 180-day peak of mode 1 has a phase speed of 4 cm s^{-1} (with a phase of 0.3 rad) at the boundary between Wb2–Wb3 which is slower than the value observed in the interior between Wb3–Wb5 (7.3 cm s^{-1}). Comparing this speed (7.3 cm s^{-1}) to those inferred from the 2D spectrum of SSHA (4.6–5.1 cm s^{-1}) over the whole basin, the mooring measurements suggest an acceleration of the speeds in the western edge of the basin. The phase–speed decrease at the boundary may partly be due to a blocking effect caused by the western boundary. Because the spatial resolution of the gridded SSHA altimetry product is coarser than the distance between Wb2 and Wb3, SSHA interpolated to the two mooring positions appears coherent at all periods. Coherence of the third mode between Wb2 and Wb3 has a major peak at a 110-day period with a negative phase, which is consistent with eastward propagating signals.

Westward propagating signals with periods of 80–250 days have been identified from altimetry and in situ moorings. The offshore mooring (Wb5) additionally indicates that the energy is in the first baroclinic mode, with translational speeds (7.3 cm s^{-1}) higher than those predicted by the linear nondispersive Rossby wave dispersion relation ($\beta\lambda_1^2 = 4.5$ cm s^{-1} using $\lambda_1 = 47$ km). This period range has previously been identified. From sea surface temperatures, Halliwell et al. (1991) observed a peak at a 200-day period in the North Atlantic Subtropical Convergence zone (59.5 to 75.5°W and 22.5 to 33.5°N). Osychny and Cornillon (2004) used zonal wavenumber/frequency spectra of SSHA, and identified two peaks: a 180-day peak was primarily in the latitude band of 25–41°N, while a 700-day peak was present equatorward of 25°N. This latitude, where the RAPID array is located, has been described as a transition between a linear Rossby wave-dominated region equatorward, and a turbulent regime of nonlinear eddies poleward of 25°N (Chelton et al., 2007; Tulloch et al., 2009) with higher phase speeds than predicted by the linear Rossby wave theory. Because the RAPID array is located right at this transition latitude, the peaks we observe may be a mix of eddies and Rossby waves.

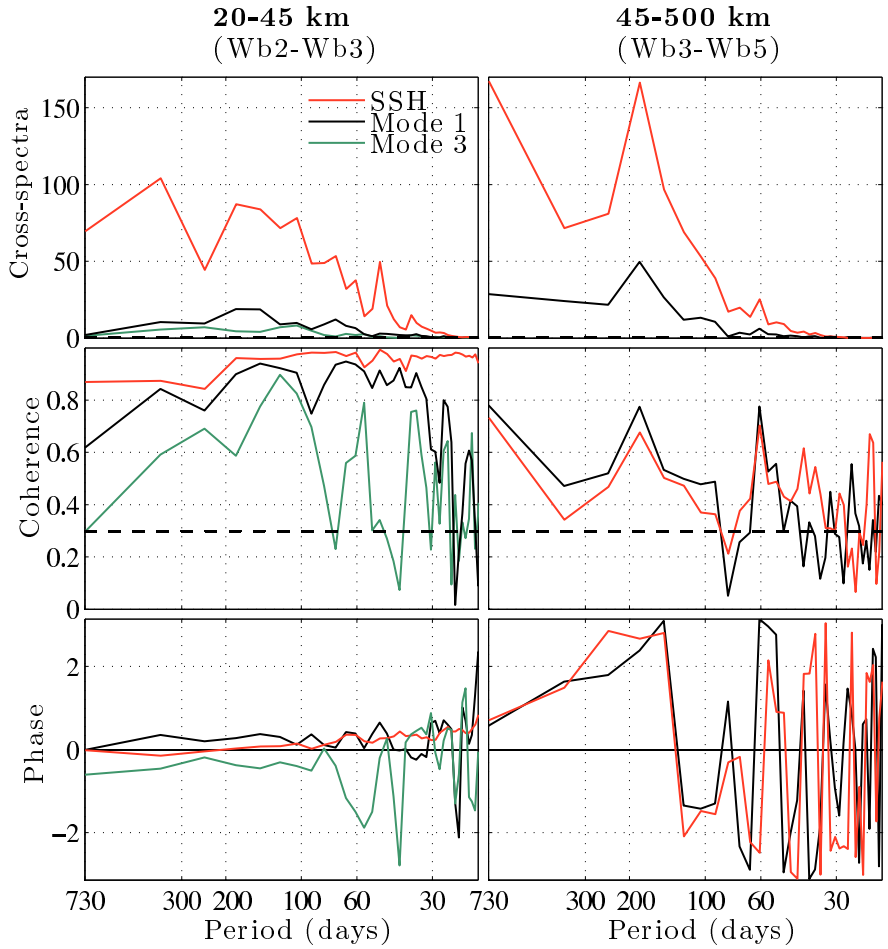

Figure 2.11: Cross-spectra (top), coherence (middle) and phase (bottom) between Wb2 and Wb3 (left) and between Wb3 and Wb5 (right) for sea surface height anomaly (red), modal amplitudes of the first baroclinic mode (black) and third baroclinic mode (green). The 95% significance level of the coherence is indicated by the black dashed line.

2.6 Discussion

Having detected a region of purely westward propagating features at midlatitudes from altimetry, the observed surface variability of SSHA was firmly associated with the first baroclinic mode. This result was expected from the significant correlation of SSHA with DHA and the expectation that DHA mainly represents the first baroclinic mode (Siegel et al., 1999). Dynamic height integrates density anomalies with depth and this quantity is expected to be maximal for the first mode which contains either positive or negative density anomalies. Stammer (1997) and Wunsch (1997) previously related the first baroclinic mode with sea surface variability with various methods. Stammer (1997) found a significant correlation between the SSH eddy spatial scale, calculated from the first-zero crossing of SSH spatial autocorrelation, and the Rossby radius of the first mode. Wunsch (1997) found that elevated interior kinetic energy of the first mode measured by deep current meters was related to regions of enhanced surface kinetic energy. Both studies observed three areas of varying dynamics from SSH spectra and from velocity

normal modes: regions of boundary currents, tropical and extratropical region in the ocean interior. In the present study the first mode was observed in the midlatitude interior ocean but also at the western boundary region, despite the increased importance of higher baroclinic modes. The variability of the first mode in the range 80–250 days was observed in all moorings located at the western boundary and in the ocean interior. This range is in agreement with period of mesoscale variability (100 days) previously detected in Lee et al. (1996) from current meters above 800 m using STACS and WATTS data or from the MODE array (Richman et al., 1977; the MODE Group, 1978). Closer to the boundary, the relative importance of the third baroclinic mode arises at periods shorter than 150 days, suggesting the local generation of this mode either by rough topography, interactions with the boundary, or from meridionally-propagating waves. An additional frequency spectrum from the Wb4 location (75.70°W) over rough topography shows no peaks at mode 3 (not shown), suggesting that rough topography is not the cause.

While we concentrated on purely westward propagating signals, the origin of these anomalies is not firmly localised. At different points along the zonal RAPID array, additional variability may be added to the observations by anomalies originating from different latitudes. This is seen in Fig. 2.2, where the non-zonal direction of anomaly propagation is shown, as well as in Fig. 2.3, where additional variability is present in the eastern boundary due to local wind stress curl (Chidichimo et al., 2010), and west of 60°W from Gulf Stream rings (Parker, 1971). In the eastern basin, eddies are created by trade winds and Canary Current anomalies and transported to 25°N before travelling westward (Sangrà et al., 2009). Sangrà et al. (2009) observed however, that only 10% of these eddies are long-lived, the rest enter the background turbulence around 25°W and do not seem to contribute significantly to variability in the western basin. The speed increase observed in the western basin (Fig. 2.3) was attributed to the deepening of the thermocline by Chelton et al. (1998) and also to topographic interactions with the MAR (Tailleux and McWilliams, 2000). There is also the potential for eddies shed from the North Brazil Current to make their way to the RAPID latitude (Jochumsen et al., 2010). These additional sources of variability may degrade the coherence between anomalies generated at the eastern boundary and propagating all the way to the west, as suggested in Kanzow et al. (2010).

In the ocean interior at Wb5, mode 1 dominates the variability with density fluctuations of the same sign over the entire water column, and maximum amplitude at the thermocline. In contrast, at the boundary, anomalies are still present in the thermocline but added variability appears in the less stratified region below 1200 m at Wb2 (Fig. 2.5). These depths are below the deeper zero crossing of the third mode at 1100 and 1500 m, explaining the intensification of this mode by deep anomalies. The reduced energy in the first mode associated with less deep coherent anomalies could be due to interactions with the DWBC (Lee et al., 1996), a hypothesis that will be further developed in the next chapter. The energy origins of the third baroclinic mode may involve multiple

processes and require further study to thoroughly disentangle them. In a two-layer simulation, the presence of rough topography was shown to increase the eddy baroclinicity (Rhines, 1977) as opposed to the typical inverse energy cascade to larger vertical and horizontal scales of stratified oceanic simulations (Fu and Flierl, 1980; Smith and Vallis, 2001). The rougher topography of the Bahama Ridge and Blake Basin compared to the Hatteras Abyssal Plain (Fig. 2.1) may contribute to the separation of the thermocline variability from that at deeper depths (the MODE Group, 1978) but the absence of mode-3 energy at Wb4 (not shown) seems to contradict this hypothesis.

In addition to the DWBC and rough topography effects, the steep slope at the western boundary may be important to support topographic waves or reflection of incoming signals. The importance of the third baroclinic mode energy at Wb2, hidden from the DWBC, compared to Wb3 suggests that the continental wall is involved. Topographic Rossby waves propagating southward and excited by incoming eddies (Louis and Smith, 1982) may also be present due to a larger topographic β-effect over planetary β. Additional meridional signals may also be detected from eddies travelling along the coast driven by the image effect (Shi and Nof, 1994). Further study on nonlinear interactions (Fu and Flierl, 1980) may show whether the eddy energy pathway to modes of smaller vertical wavelengths is active as demonstrated in Dewar and Hogg (2010).

2.7 Conclusions

The presence of purely westward propagating features at the mid-latitudes was confirmed with altimetry. The zonal extent of these features is in the range of 350–800 km with a period of 80–200 days. The propagating features respect the dispersion relation of linear Rossby waves at their lowest frequencies and lowest wavenumbers. The main ridge of energy is, however, located above the first baroclinic mode dispersion relation and contains a faster phase speed than the linear theory of Rossby waves. This property happens to be especially true at the mid-latitude interior and western boundary where surface anomalies are less affected by boundary currents such as the North Brazil Current or the Gulf Stream. Having detected these surface features at the latitude of the mooring array, the vertical structure of eddies and Rossby waves was studied. Anomalies of isopycnal displacements in the ocean interior away from the western boundary are observed across the full water column. They are characterised by an integral timescale of 50 days in the thermocline and are significantly correlated with SSHA from the surface to 4500 m. Approaching the western boundary and the strong DWBC with observations 50 km and 20 km offshore, these anomalies are still observable but restricted to the top 3000 m and 1200 m respectively and are associated with shorter integral timescale of 30 days. Below 1200 m at 20 km offshore, additional variability uncorrelated to SSHA and with the shortest timescale is observed.

Using a normal mode decomposition and a WKBJ analysis, it became possible to relate a fixed vertical structure to isopycnal displacements associated with westward propagating features. The first mode captures most of the coherent signal in the thermocline and explains an important fraction of the variance in the ocean interior. This result supports the strong correlation of SSHA and isopycnal displacements extending to 4500 m at Wb5. Approaching the western boundary the available potential energy and the variance explained by the first mode decreases, the presence of the continental wall and the DWBC can strongly affect these features. Density anomalies at the boundary are represented not only by the first baroclinic mode but also by higher baroclinic modes. The increased complexity of the vertical structure at the boundary contributes to the reduction of correlation between SSHA and dynamic height anomalies. Despite the reduced variance explained by the first mode at the boundary, a peak of energy is observed at 80–250 days in all moorings, which supports the period already identified in the SSHA spectrum. Westward propagating anomalies are expected to travel all the way to the boundary where most of their energy can be dissipated.

A coherence study of modal amplitudes and SSHA confirms the presence of westward propagating signals at the identified period range. Similar phases in the coherence spectra are found in both datasets and indicate a propagation speed of 7.3 cm s^{-1} between Wb3 and Wb5, also higher than predicted by the linear theory (4.6–5.1 cm s^{-1}). The speed inferred from the phase spectra reduces between Wb2 and Wb3 (4 cm s^{-1}), this decrease may partly be due to the blocking effect of propagating anomalies by the western boundary.

Having localised along the mooring array the range of depths affected by eddies and Rossby waves, it is possible to establish their contribution to the large scale circulation (chapter 3). Overall the energy associated with propagating features is decreasing at the boundary, and several pathways may produce this loss of energy. The identification of these features at the boundary will facilitate the study of their interaction with internal waves over large topographic anomalies (chapter 4).

Chapter 3

The effect of westward propagating anomalies on the meridional overturning circulation

3.1 Introduction

Based on five transatlantic sections at 24°N in the Atlantic, Bryden et al. (2005b) found a 30% decrease in the MOC from 1957 and 2004. The reduction was observed in an increased southward upper-mid ocean transport, and a decreased southward lower North Atlantic deep water (LNADW). Although the amplitude of the change was close to the eddy uncertainty ± 6 Sv estimated in Ganachaud (2003) using inverse calculations from similar hydrographic sections, the existence of a temperature anomaly in the thermocline within several longitude degrees of the western boundary and an uneven deep compensation led Bryden et al. (2005b) to discard an eddy-induced explanation.

The continuous measurements of the MOC provided since 2004 by the RAPID program enable the subannual variability of MOC to be examined in detail (Cunningham et al., 2007). Kanzow et al. (2010) attributed most of the decline observed in Bryden et al. (2005b) to the seasonality of the MOC. The seasonality of 5.9 Sv is visible in the upper mid ocean and mostly originates from density changes at the eastern boundary following wind-stress curl anomalies (Chidichimo et al., 2010). Although the 2004 transport anomaly is reduced by taking into account the seasonalilty of the upper mid-ocean transport, the anomaly in the thermocline was located at the western boundary which is a region of more important eddy activity than the eastern boundary (Kanzow et al., 2009). The exact contribution of eddies to geostrophic transport at subannual periods remains an open question. Based on the vertical structure of propagating features analysed in the previous chapter, these processes are expected to contribute to the thermocline variability but not directly to the deep water transport variability.

The influence of Rossby waves on the MOC was estimated by Hirschi et al. (2007) in an eddy-permitting model. The authors attributed 3-4 Sv of the MOC variability to Rossby waves through the thermal wind relation. Despite the presence of eddies and Rossby waves at the boundary, Kanzow et al. (2009) suggested that the MOC variability is not strongly affected by these features because their energy decreases with proximity to the boundary. Particularly on interannual to decadal timescales, Kanzow et al. (2009) determined that eddies do not dominate the MOC variability. Their main argument, reinforced by Bryden et al. (2009), comes from the observation of a threefold decrease of rms sea surface height anomaly (SSHA) and dynamic height anomaly (DHA) from 100 km to 20 km offshore of the western boundary. The reduction of both SSHA and DHA variability was hypothesized to originate from the export of anomalies through boundary-trapped waves. Using SSHA to characterise the decrease of eddy variability, Kanzow et al. (2009) calculated the upper bound of the transport variability attributed to eddies to be 4.2 Sv between 1992 and 2008. This is in contrast to Wunsch (2008) who found 16 Sv without taking into account the observed SSHA rms decrease at the western boundary.

The aim of the present chapter is to assess the influence of westward propagating features on the MOC. Having identified the vertical structure of these features in the previous chapter and their surface signature with the altimetry, their effect on the upper mid-ocean can be estimated. The calculation of the upper mid-ocean transport within the RAPID program is first presented. The upper mid-ocean transport combines with Gulf Stream and Ekman transport to give the upper ocean component of the MOC. The mid-ocean transport is partially composed of the geostrophic transport and a barotropic component inferred from an imposed transport conservation. The influence of eddies and Rossby waves on the baroclinic transport will be evaluated by focusing on first baroclinic mode processes. A distinction will be made between subannual and interannual timescales to determine the temporal extent of their influence. This should contribute in the future to discern the origins of processes affecting the MOC.

3.2 Methods

3.2.1 MOC calculation

According to the RAPID methodology detailed in Rayner et al. (2011), the MOC is defined as the northward transport which is integrated from the surface to the level of maximum transport. The depth of maximum transports occurs roughly at 1100 dbar and corresponds to the interface between Antarctic Intermediate Water and North Atlantic Deep Water. The northward MOC transport arises from the sum of the Gulf Stream (T_{GS}), the Ekman (T_{EK}) and the upper mid-ocean transport (T_{UMO}). The Gulf Stream transport is inferred from telephone cable measurements in the 800-m deep Florida Strait

between the Bahamas and the Florida coast (Baringer and Larsen, 2001). The Ekman transport is obtained from zonal wind stress from the Cross-Calibrated Multi Platform (CCMP) wind product. The upper mid-ocean transport, integrated from the surface to the depth of maximum transport (z_{max}) around 1100 dbar, is composed of internal transport ($\mathrm{T_{INT}}$), western boundary wedge transport ($\mathrm{T_{WBW}}$) and external transport ($\mathrm{T_{EXT}}$) as described in Kanzow et al. (2007).

The internal transport ($\mathrm{T_{INT}}$)

$$T_{INT}(p,t) = \int_{x_E}^{x_W} v_{geo}(p,t)dx \tag{3.1}$$

is the zonally integrated geostrophic velocity (v_{geo}) which is given by

$$v_{geo}(p,t) = \frac{1}{f(x_W - x_E)} \int_{p_{ref}}^{p} (\delta_W(p',t) - \delta_E(p',t))dp' \tag{3.2}$$

between the eastern boundary (E) and Wb2 at the western boundary (W), with f the Coriolis parameter, x the horizontal distance, δ the specific volume anomaly and p_{ref} the reference pressure at 4820 dbar.

The western boundary wedge ($\mathrm{T_{WBW}}$) is measured directly from current meters and acoustic Doppler current profilers located between the Bahamas and Wb2 (Johns et al., 2008). The external transport ($\mathrm{T_{EXT}}$) is a depth-independent flow which is computed in order to conserve mass transport across the section between the Gulf Stream, Ekman and mid-ocean transports

$$\int_{p_{bottom}}^{0} (T_{GS}(p,t) + T_{EK}(p,t) + T_{INT}(p,t) + T_{EXT}(p,t) + T_{WBW}(p,t))dp = 0\ . \tag{3.3}$$

The external transport is distributed uniformly over the area of the section and its profile of transport per unit depth is proportional to the zonal width of the basin at each depth. The vertical profile of $\mathrm{T_{EXT}}$ is almost uniform in the top 4000 dbar and decreases to zero below 4000 dbar because the longitudinal extent is not greatly affected by the sloping boundaries or by the presence of the MAR. Applying the mass conservation, the upper mid-ocean transport ($\mathrm{T_{UMO}}$) can be calculated

$$T_{UMO}(t) = \int_{z_{max}}^{0} (T_{INT}(p,t) + T_{EXT}(p,t) + T_{WBW}(p,t))dp. \tag{3.4}$$

3.2.2 Density anomalies attributed to westward propagating signals

Building upon a baroclinic mode decomposition used in Chapter 2 to characterize the vertical structure of propagating anomalies, here the baroclinic modes are used to calculate their impact on geostrophic transport. The first step is to transform back from mode-space into density anomalies. Starting from isopycnal displacements of neutral

densities $\zeta(z,t)$, the corresponding density anomalies are obtained from the density equation neglecting nonlinear terms

$$\gamma^n(z,t) = \overline{\gamma}^n(z) - \zeta(z,t)\frac{\partial\overline{\gamma}^n(z)}{\partial z}. \tag{3.5}$$

The density equation assumes constant density following a fluid particle and density anomalies are only governed by the vertical advection of the background density (Kundu et al., 2012). The difference between in-situ and neutral density at each depth, which depends on compression due to the water column, is constant in time. The previous equation can therefore be rewritten for in-situ density instead of neutral density

$$\rho(z,t) = \overline{\rho}(z) - \zeta(z,t)\frac{\partial\overline{\gamma}^n(z)}{\partial z}. \tag{3.6}$$

Large displacements of isopycnals with maximal values in the range 100–150 m are observed at Wb2 within the thermocline. The stratification of the thermocline has two maxima, a larger one in the upper 600 m and a weaker secondary maximum from 800–1200 m (Fig. 2.1). To account for varying stratification, the last term in Eq. 3.6 is calculated separately for every 20 db. This discretisation is particularly relevant in depths of strongly varying buoyancy frequency. To assess the reconstruction method of density anomalies, observed and reconstructed isopycnals using the first 20 baroclinic modes are presented in Fig. 3.1. The reconstructed isopycnals using 20 modes capture relatively well the observed variability and explains 95% of the variance. One limitation of the method is apparent during an event in November 2010 where the stratification at 400 m in mooring data was significantly different from the time-averaged stratification used in Eq. 3.6.

3.3 Effect of westward propagating processes on the MOC

Before assessing the effect of westward propagating features on the transbasin geostrophic transport, the transatlantic section taken in 2010 is presented. From this section different water masses can be localised and their depth range, potential temperature and mean transport are identified. Looking at SSHA properties across the basin may provide information on the evolution of propagating processes given the local topography. Having defined the background through which eddies and Rossby waves propagate, it becomes possible to estimate whether these features influence the geostrophic transport or not. From the knowledge of their vertical structure, we will quantify this effect.

3.3.1 Transatlantic section of 2010

A transatlantic section was measured in January-February 2010 (Atkinson et al., 2012) to study the large-scale decadal circulation and to supplement the previous five hydrographic sections of 1957, 1981, 1992, 1998 and 2004 discussed in Bryden et al. (2005b).

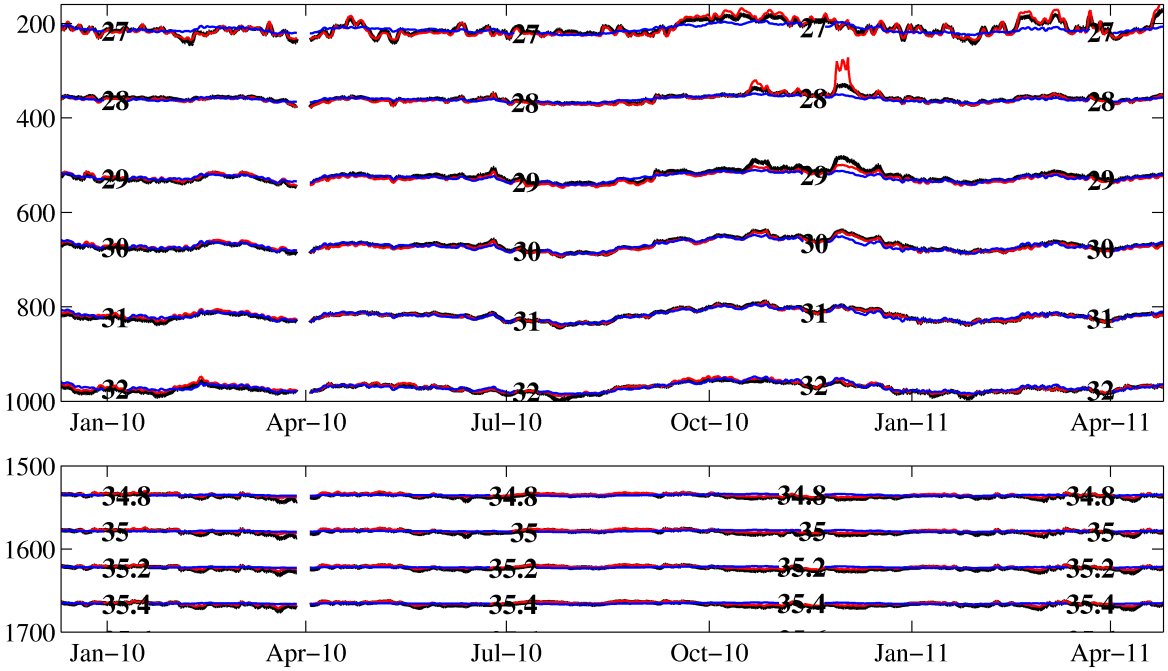

Figure 3.1: Observed isopycnals at Wb2 (black) and reconstructed isopycnals attributed to the first (blue) and the first 20 (red) baroclinic modes above 1000 m (top) and zoomed in the deep layer between 1500 to 1700 m (bottom). The time-period shown is a subset of the entire record chosen as a representative example.

The 2010 transatlantic section of temperature is displayed with the mean associated transport from the Rapid section (Fig. 3.2). The different water masses and layer names composing the section are identified from the surface to the bottom based on their depth and potential temperature following Longworth (2007). The thermocline waters are above 800 m ($\theta > 9.5$°C) and contain the surface, thermocline and lower thermocline waters. The mean mid-ocean transport and standard deviation from the RAPID section between April 2004 to April 2011 are -17.9 $\pm$ 3.4 Sv above 800 m. The intermediate layer contains Antarctic Intermediate Water (AAIW) and Mediterranean Water (MW). They are located between 800 and 1100 m ($5 < \theta < 9.5$°C) with a mean transport of 0.4 $\pm$ 0.6 Sv. The upper mid-ocean transport defined in section 3.2.1 is integrated from the surface to approximately 1100 m and so comprised the thermocline and intermediate layers. The upper mid-ocean transport contains the entire transport including the wedge and the barotropic compensation. The mean of the Gulf Stream and Ekman transports are 31.6 $\pm$ 3.1 Sv and 3.2 Sv $\pm$ 3.5 Sv respectively. In the right panel of Fig. 3.2, the mean mid-ocean transport calculated from the RAPID array is displayed. Below the intermediate layer, the southward flowing Upper North Atlantic Deep Water (UNADW) is located between 1100 to 3000 m ($2.5 < \theta < 5$°C) and includes Labrador Sea Water (LSW), the North Atlantic Interior Water (NAIW) and Iceland Scotland Overflow Water (ISOW). The mean transport of the UNADW is -12 $\pm$ 2.7 Sv. Deep waters also contain the densest NADW called the Lower North Atlantic Deep Wa-

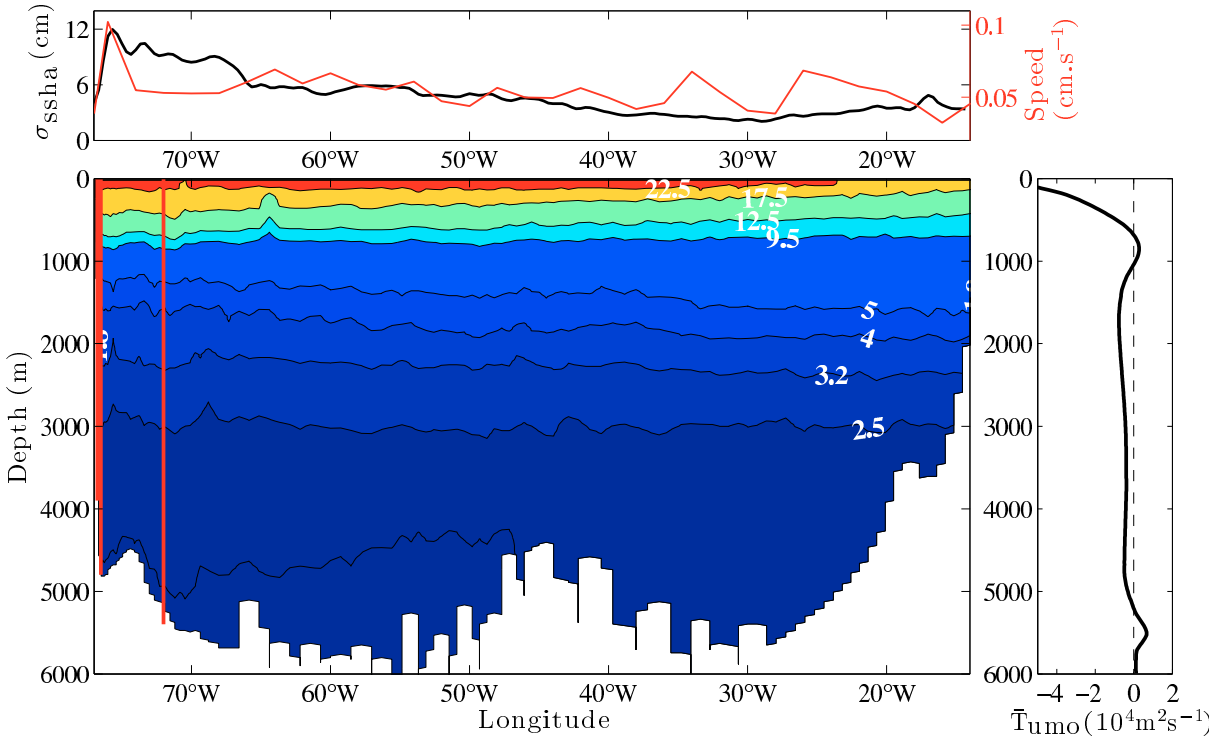

Figure 3.2: Standard deviation of SSHA at 26.5°N (black) and mean phase speed (red) of westward propagating features obtained from lagged-correlation of SSHA within a 300-km diameter circle centred every 2 degrees of longitude (top panel). Transatlantic section of potential temperature in 2010 (bottom left panel), the location of Wb2, Wb3 and Wb5 is indicated by vertical red lines. The mean upper mid ocean transport calculated from the RAPID array per unit depth is displayed (right panel).

ter (LNADW) between 3000 and 5000 m comprising Denmark Straits Overflow Water (DSOW). The average transport of LNADW is -7.1 ± 3.1 Sv. The deepest waters below 5000 m ($\theta < 1.8$°C) are the Antarctic Bottom Water (AABW) with a mean transport of 2 ± 0.6 Sv.

Eddies and Rossby waves are responsible for an important part of SSHA variability as described from their 2D spectra. Past studies find that SSHA variability increases gradually towards the western part of the basin, but then decreases sharply (11 to 5 cm) within 100 km of the western boundary (from 75.8 to 76.75°W, Kanzow et al., 2009). The SSHA standard deviation is displayed along the full section with the phase speed of propagating features determined from SSHA lagged correlations in Fig. 3.2. The SSHA variability increases continuously from 30°W to 76.75°W with an intensification around 66°W before decreasing to the western boundary. The phase speed of propagating signals varyies around 7 cm.s^{-1} in the western basin east of 68°W and is constant at 5 cm.s^{-1} from 68°W to 74°W. At the boundary from 74 to 76°W the phase speed strongly increases and decreases in the same longitude range as the rms SSHA decrease. The increased rms SSHA and decreased phase speed both located around 66°W indi-

cate that this location has an important dynamical effect on propagating features. The DWBC is not expected to contribute much to this shift of variability observed at 66°W as the DWBC is located westward of 66°W at this latitude. In addition a northward recirculation, which is located offshore of the DWBC (Bryden et al., 2005a), may influence westward propagating features at this longitude. However, the profile of propagating features which extends almost throughout the full depth at Wb5 (500 km offshore) in Fig. 2.7 discards the hypothesis that the northward recirculation may strongly affect the structure of these features.

Westward propagating processes may be affected by the steep shallowing topography moving from 68°W to 74°W which is co-located with a reduced phase speed and increased rms SSHA. The phase speed of long Rossby waves depends on the Rossby radius of deformation and β. Based on the definition of the Rossby radius through the depth-integrated buoyancy frequency (Chelton et al., 1998), the phase speed is expected to decrease over shallowing topography, which is consistent with our observations westward of 68°W (Fig. 3.2). Further analysis on the interaction of westward anomalies with the boundary will be developed in the fourth chapter.

The period, zonal wavelength and vertical structure of westward propagating features have now been identified. Upon arriving at the boundary, these features will either deepen or shoal the isopycnals at the thermocline, changing the incline between the eastern and western boundary. In this wave pattern, each crest and trough is associated with a positive or negative anomaly, but across a full period of crest and trough, the transport anomaly is essentially zero. The effect on the MOC is strongest when an eddy or the wave arrives at the boundary, loses its symmetry, and thus causes a net meridional transport.

3.3.2 Reconstruction of first mode anomalies

Having identified the signature of westward propagating features in the first baroclinic mode, their effect on the geostrophic transport can be evaluated. The density field attributed to the first mode (ρ_1) is constructed by replacing isopycnal displacements in Eq. 3.6 by their first mode contribution ($\hat{\zeta}_1 F_1$). Density anomalies attributed to the first mode are visualised in Fig. 3.1. The observed variability is especially well-reproduced by the first mode above the lower boundary of the thermocline around 1000 m. Large displacements that are vertically coherent and last several months are represented by first mode isopycnals. Closer to the surface ($\sim$200 m), additional high-frequency isopycnal variability is observed and is not captured by the first mode. Isopycnal displacements go to zero at the surface because of the boundary condition of normal mode. The surface boundary condition implies that eddies and Rossby waves have small signatures near the surface, and thus are unable to represent near-surface signals measured by the array. Different representations incorporating the surface buoyancy anomalies through a sur-

face quasi-geostrophic mode to the normal modes have been developed to represent the shallow variability (Lapeyre, 2009). However, because our moorings are not designed to measure shallow or surface hydrographic properties, which would significantly decrease mooring durability and recovery rates, surface quasi-geostrophic modes can not be accurately assessed. From the insignificant correlation of SSHA and isopycnal displacements below 1200 m, the first mode is not expected to reproduce the deep signal as observed in Fig. 3.1. The inclusion of higher baroclinic modes is necessary to recover the deep variability as seen from the agreement between isopycnals and the isopycnal variability attributed to the first 20 modes.

In the process of evaluating the geostrophic transport variability assigned to westward propagating features, we rely on the hypothesis that the first mode reasonably captures these features. This assumption is comparable to the method of Wunsch (2008) who projected SSHA variability to the first mode before assessing its contribution to the geostrophic transport. In the previous chapter we observed that the variance of isopycnal displacements is only partially explained by the first mode at the boundary. The reduction of variance explained by the first mode when approaching the western boundary supports the decrease of eddy amplitude in SSHA rms already found in Kanzow et al. (2009).

The assumption that the first mode mainly represents westward propagating features may not be fully accurate. The first mode could also represent hydrographic variability coherent within the thermocline and extending horizontally in the same water mass. The westward movement seen in the coherence spectra suggests that mode 1 represents mainly eddy and Rossby wave activity in a defined frequency range. The coherence associated with a strong percentage of variability in the first mode in the range of 80 to 250 days supports this hypothesis. The mode 1 variability for periods over 250 days may contain the interannual signal associated with different large scale processes such as varying deep water formation rates or atmospheric forcing of the ocean, such as through the North Atlantic Oscillation. Our choice of block averaging on a seven-year timeseries led us to focus on subannual processes. The interannual signal is not expected to be well captured in our spectral analysis and it may be aliased in other frequencies. Longer measurements in the future should render spectral analysis of other large scale features easier.

Another limitation of using only the first mode to represent eddies and Rossby waves is that their signatures in higher modes are not considered. This arises from the fact that higher baroclinic modes may be excited by the interaction of westward propagating features with the topography and DWBC. We specifically focus on anomalies directly observed to propagate in surface and subsurface data knowing that including higher baroclinic modes could enhance or diminish the effect of propagating features on the geostrophic transport.

3.3.3 Geostrophic transport of first mode signals

We focus here on the western boundary which could give information on anomalies travelling from various locations. For example Gulf Stream rings are observed to travel southward to 25°N in Parker (1971). The multiple origins of westward propagating features will be studied in more details in the fourth chapter. The contribution of the first mode to dynamic height at the western boundary can be calculated by vertically integrating the specific volume anomaly

$$\delta_{1\_W}(p) = \frac{1}{\rho_1(S,p,T)} - \frac{1}{\rho(35,0,p)}. \tag{3.7}$$

The resulting geostrophic velocity is computed by keeping the eastern boundary unchanged in Eq. 3.2. The internal transport is the zonal integral of the geostrophic velocity (Eq. 3.1) obtained using the mode 1 dynamic height profile at the western boundary.

In the RAPID methodology, hydrographic data below 3900 m are not measured by Wb2 and are obtained from additional adjacent deep moorings WBH1-WBH2 from 2004 to 2005 and from the full depth mooring Wb3 starting in 2005 (Kanzow et al. 2009). The construction based on the first baroclinic mode at Wb2 limits the vertical resolution to the depth of Wb2. This arises from the boundary condition of the normal modes at the bottom. The mode 1 assumes no variations of isopycnal displacement below 3900 m. To obtain a transport coherent with the normal mode construction we impose a mean density below 3900 m. This would not change any interpretation of the time variability, which is the focus of any eddy/wave investigation. This is one limitation of the methodology but several remarks make this hypothesis reasonable. Firstly, the westward propagating signal shown in the correlation of isopycnal displacements with SSHA is not believed to exist below 1200 m at Wb2, so the signature of propagating features is not expected to be seen deeper than 3900 m in the proximity of Wb2. This is confirmed by the fact that the correlation is not significant below 3000 m at Wb3 located only 29 km from Wb2. Secondly, the deep resolution of propagating features is not as essential at the boundary as it would be at Wb5 which contains a significant correlation between isopycnal displacements and SSHA until 4500 m (Fig. 2.6). The density profile attributed to the first mode at Wb3 could be added to the deep profile representing the western boundary. This will however add discontinuities in the density field mostly due to varying modal representations at Wb2 and Wb3.

The difference introduced in the calculation of the internal and upper mid-ocean transports by using Wb2 only for the western boundary instead of Wb2, Wb3, WBH1 and WBH2 is evaluated in Fig. 3.3. The error is seen mainly in the deep water geostrophic flow below 3900 m according to the two different methods. Wb2 partially failed from

November 2005 to March 2006 and so this period lacks data for the mode 1 reconsruction. The internal transport temporal anomaly is calculated in Fig. 3.3 using Wb2 only at the western boundary (T'_{INT_Wb2}) and according to the RAPID methodology (T'_{INT}) as described in Kanzow et al., (2010). The results are shown integrated for the top 1100 m and the section deeper than 1100 m. The significant correlation of 0.96 below 1100 m means that we do not introduce a large error using Wb2 at the western boundary compared to the observed deep geostrophic transport. The interval between 1100 to 3900 m represents most of the deep variability compared to the section from 3900 to 4800 m. Despite the significant correlation below 1100 m attributed to anomalies of similar frequency in T'_{INT} and in T'_{INT_Wb2}, the two timeseries have different amplitudes. The standard deviation of T'_{INT} and T'_{INT_Wb2} are 5.2 and 4.3 Sv respectively. This indicates that the deep section from 3900 to 4800 m amplifies the transport between 1100 to 3900 m and both sections are mostly affected by similar anomalies.

The upper mid-ocean transport using both methods is also displayed in Fig. 3.3 and the two transports have a correlation coefficient of 0.96. The difference between the upper mid-ocean transport and the internal transport is introduced by a varying barotropic compensation given a similar western wedge transport in both methods. Considering only Wb2 at the western boundary will redistribute the underestimation of the deep geostrophic transport represented in the 3900-4800 m section through the barotropic component. Overall from the significant correlation (0.96) we do not expect to introduce a large error in the calculation of the upper mid-ocean transport by considering Wb2 only. The estimation of the geostrophic transport attributed to the variability of the first mode at Wb2 is calculated in the following section.

3.3.4 Effect of westward propagating processes on the geostrophic transport

The geostrophic internal transport is calculated by taking into account mode 1 anomalies at the western boundary. To reflect eddy and Rossby wave activity at the western boundary only, the dynamic height at the eastern boundary is fixed to its temporal mean for the transport attributed to mode 1 as done in previous studies (Kanzow et al., 2010; Chidichimo et al., 2010). The geostrophic transport anomaly attributed to the first mode ($T'_{INT\ mode1}$) is calculated and compared to the observed transport (T'_{INT}) integrated in the top 1100 m (Fig. 3.4). The variability attributed to mode 1 captures a significant amount of the observed shallow geostrophic transport on subannual timescales. The correlation between the two transports of 0.77 is significant at 95%. The variance of the geostrophic transport explained by the first baroclinic mode above 1100 m is 59%. The phases of the subannual variability in both transports are mostly in agreement but the amplitudes of the anomaly varies. This is reflected in the standard deviation of 5.5 Sv for T'_{INT} being higher than 3.5 Sv for $T'_{INT\ mode1}$. Using a mode 1 structure to represent eddies and Rossby waves, an upper limit of their effect on the

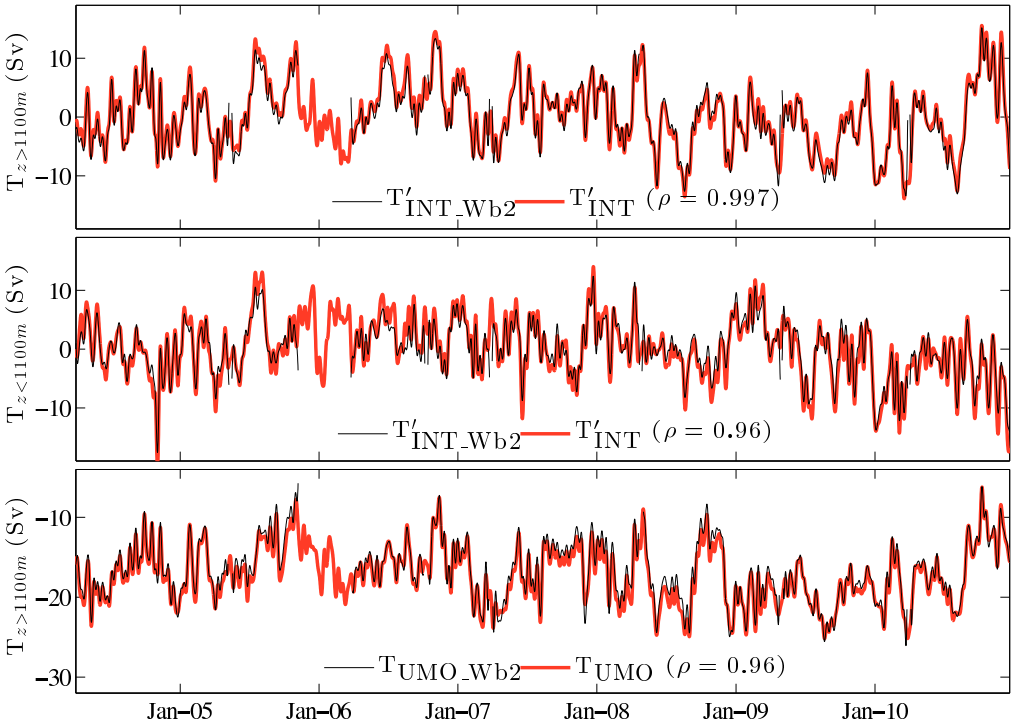

Figure 3.3: Top: geostrophic meridional internal transport anomaly (T'_{INT}) for the top 1100 m using Wb2, Wb3, WBH1 and WBH2 at the western boundary in red, and internal transport anomaly using Wb2 only in black (T'_{INT_Wb2}). Their correlation coefficient (ρ) is indicated in the label. Middle: same as top panel but for water deeper than 1100 m. Bottom: upper mid-ocean transport (T_{UMO}) for the top 1100 m using Wb2, Wb3, WBH1 and WBH2 at the western boundary in red, and upper mid-ocean transport using Wb2 only in black (T_{UMO_Wb2}).

variability of the geostrophic transport is therefore believed to be about 3.5 Sv.

The influence of propagating signals on interannual timescales is evaluated by comparing 1-year lowpass filtered transports ($T'^{\,t>1\ year}_{INT}$ versus $T'^{\,t>1\ year}_{INT\ mode1}$) in Fig. 3.4. The mode 1 interannual transport does not have any significant variability with a standard deviation of 0.6 Sv. This transport differs from the observed interannual transport which contains larger anomalies and a standard deviation of 2.4 Sv. The correlation between the two interannual transports of 0.41 supports the reduced effect of westward propagating features on interannual transports. This correlation is not significantly different from 0 with 95% confidence because of the reduced degrees of freedom of low-passed filtered transports. This reduction of low frequency variability was expected from the mode 1 spectrum at Wb2 which did not contain much signal at interannual timescales. The reduction was observed in the interval 250 to 730 days based on the choice of block averaging. Using the modal identification of eddies and Rossby waves, these processes are not expected to affect the geostrophic interannual transport. From the low frequency limit used in the block averaging, we cannot rule out large-scale Rossby waves of lower frequency. In a regime of varying midlatitude interannual eddy dynamics, the non-stationarity of these processes may be reflected in the interannual geostrophic transport. This hypothesis

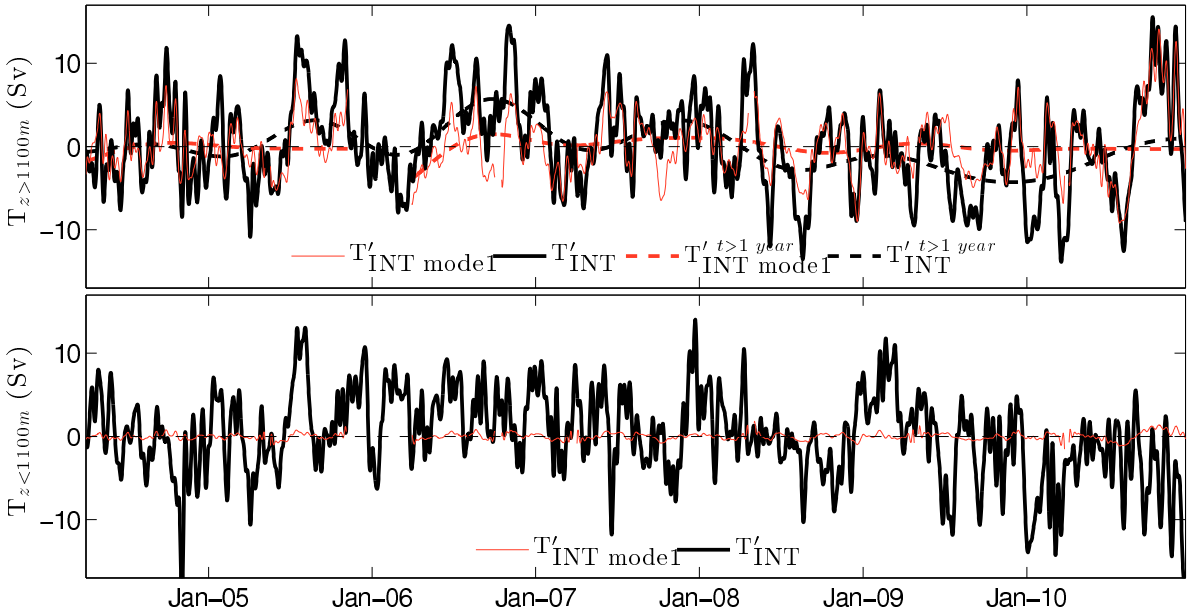

Figure 3.4: Geostrophic meridional transport anomaly observed (T'_{INT}, black line) and attributed to the first baroclinic mode ($T'_{INT\ mode1}$, red line) at the western boundary for the upper 1100 m (top) and below 1100 m (bottom). The correlation coefficients between the observed (T'_{INT}) and first mode ($T'_{INT\ mode1}$) internal transports are 0.77 in the upper layer and 0.09 in the deep layer. The dashed lines in the top panel indicate the interannual (1-year low-pass filtered) observed upper transport ($T'^{\ t>1\ year}_{INT}$) and upper transport attributed to mode 1 ($T'^{\ t>1\ year}_{INT\ mode1}$). The correlation between the two low-pass filtered upper transports is 0.41.

may have to be considered in the presence of interannual variability in longer timeseries than currently measured. Below 1100 m, the transport attributed to mode 1 contains small variations which are an order of magnitude smaller than the observed variability (standard deviation of 0.4 Sv against 5.1 Sv) in Fig. 3.4; both transports are not significantly correlated. This is expected from the increased importance of high baroclinic modes to represent the deep boundary variability, and is also noticed in the insignificant correlation between isopycnal displacements and SSHA below 1200 m at Wb2 (Fig. 2.7).

3.3.5 Effect of westward propagating processes on each layer and on the MOC

To study the effect of propagating anomalies on each layer, the variability added by these processes is first analysed in the velocity profile. The barotropic compensation is then presented. The temporal mean specific volume anomaly and dynamic height integrated from the reference pressure at 4820 dbar are displayed in Fig. 3.5. The mooring considered at the western boundary is Wb2. At the eastern boundary, an array of aggregated mooring (EB1–EB3, EBH1–EBH5 and EBM1–EBM7) is used within the RAPID methodology as further described in Rayner et al. (2011). The mean specific

volume anomaly profiles show a higher density at the western boundary than at the eastern boundary from 4820 to 3300 dbar and from 1800 to 900 dbar. From 3300 to 1800 dbar and above 900 dbar, the eastern boundary density is higher than the western boundary density. From the construction of density anomalies attributed to mode 1, the observed density anomalies are mostly captured above 1000 m (Fig. 3.1). The effect of westward propagating features will be strongest in the top 900 m where the mode 1 dynamic height horizontal gradient is strongest.

The profile of mean meridional geostrophic velocity referenced at the bottom is shown in Fig. 3.5. The velocity contains a maximum around 900 m encompassed by a local minimum between 1600–2000 m and a strong decrease in velocity above 900 m. The standard deviation of the velocity is added for the observed velocity and for the velocity due to the mode 1 variability at the western boundary. The standard deviation of the observed velocity is larger than 0.05 cm s^{-1} above 1100 m and larger than 0.02 cm s^{-1} above 3500 m. The standard deviation of the velocity attributed to the first mode is two times smaller than for the observed velocity above 1000 m with a value of 0.02 cm s^{-1} but is strongly reduced below 1500 m ($<5\times10^{-3}$ cm s^{-1}). The vertical extent in the top 1000 m of the large standard deviation attributed to mode 1 is expected from the mode 1 structure and also from the presence of higher baroclinic modes at the boundary. The importance of first mode processes is largest in the transport above 1100 m. Below 1100 m higher baroclinic modes contribute to the observed transport variability.

The influence of westward propagating features on the internal transport in the top 1100 m is significant at subannual timescales from the correlation of 0.77 between T'_{INT} and $T'_{INT\ mode1}$. The transport variability attributed to these features is 3.5 Sv, the standard deviation of $T'_{INT\ mode1}$. This large and direct effect on the geostrophic transport motivates us to estimate the influence of propagating features on the upper mid-ocean transport (T_{UMO}). This will define the effect on the basinwide transport, which also includes the wedge, Ekman and barotropic transports and is directly related to the MOC. The main step to obtain T_{UMO} is to provide a reference to the geostrophic internal transport T_{INT} defined relative to 4820 dbar in Fig. 3.5. The internal transport is shifted by the external transport to reflect the mass conservation (section 3.2.1). The compensation is uniformly distributed over the area of the cross section. The variability attributed to first mode features is similarly redistributed in each depth layer. The compensating process of eddy and Rossby wave signature in T_{INT} was believed to explain a part of the significant correlation observed between the internal and external transport in Kanzow et al. (2007). Knowing the location where geostrophic transport imbalances are created may indicate where the barotropic adjustment is most likely to take place in the longitudinal section.

To localise only the effect of westward propagating features on the upper mid-ocean transport, the Gulf Stream, Ekman and wedge transports are fixed to their temporal

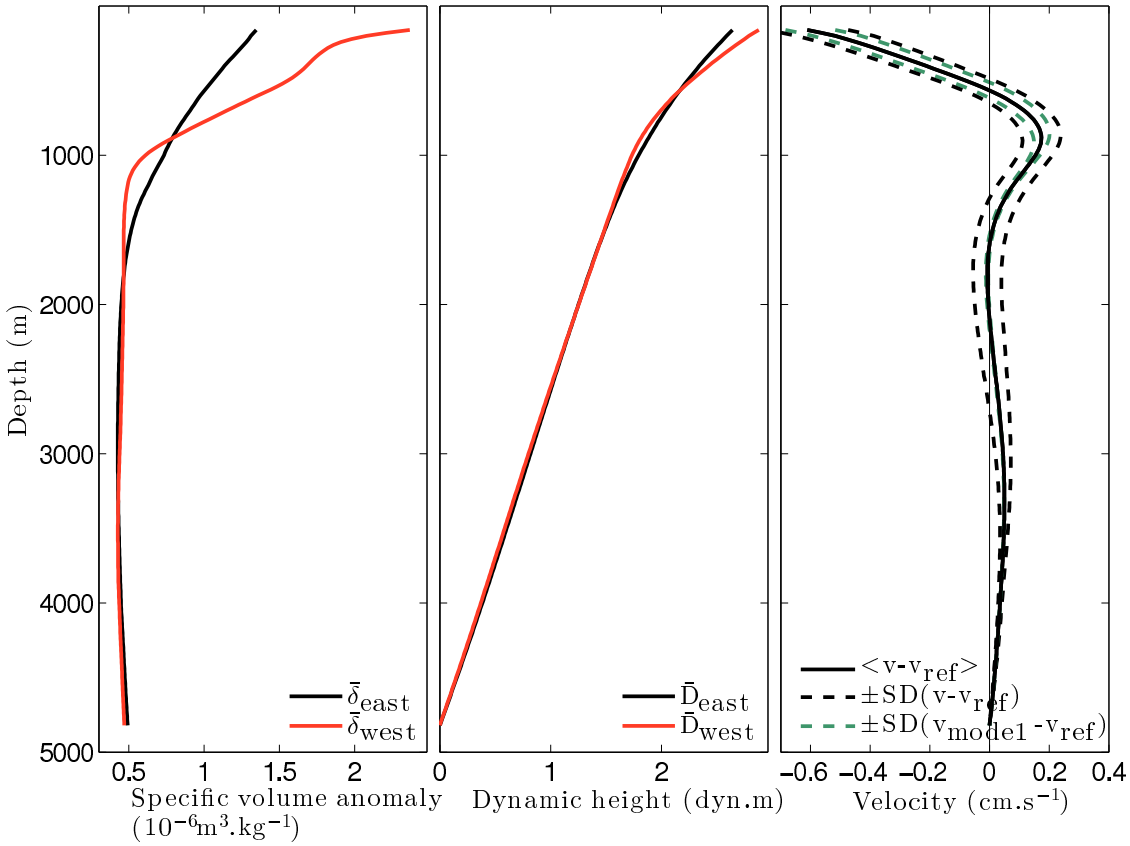

Figure 3.5: Left: Mean profiles of specific volume anomaly at the western (red) and eastern boundary (black). Middle: Mean profiles of dynamic height at the western (red) and eastern boundary (black). Right: Mean (black) and ± the standard deviation (dash black) of the geostrophic meridional velocity between the western and eastern boundary. Standard deviation of the geostrophic meridional velocity using mode 1 density profile at the western boundary and a mean density profile at the eastern boundary (green).

mean and the obtained $T_{UMO\ mode1}$ is compared to the observed T_{UMO} (Fig. 3.6). The upper mid-ocean transport considers mode 1 density anomalies at the western boundary and a mean density profile at the eastern boundary ($T_{UMO\ mode1}$). A significant correlation of 0.65 is found between the two transports. The upper mid-ocean transport contains the internal, the wedge and the external transport. A reduction in the correlation between the observed and mode 1 transport is thus expected moving from T_{INT} to T_{UMO}. The small reduction from 0.77 to 0.65 indicates that eddies and Rossby waves are still important and able to explain 42% of the variance of T_{UMO}. As for T_{INT}, the amplitude of T_{UMO} variability attributed to mode 1 (2.6 Sv) is smaller than observed (3.4 Sv). A significant percentage of the variance explained of the mid-ocean transport of the MOC is related to westward propagating features.

The variability created from mode 1 anomalies directly affects the geostrophic transport shallower than 1100 m in Fig. 3.4 and Fig. 3.5. The geostrophic transport below 1100 m does not contain much variability attributed to westward propagating processes.

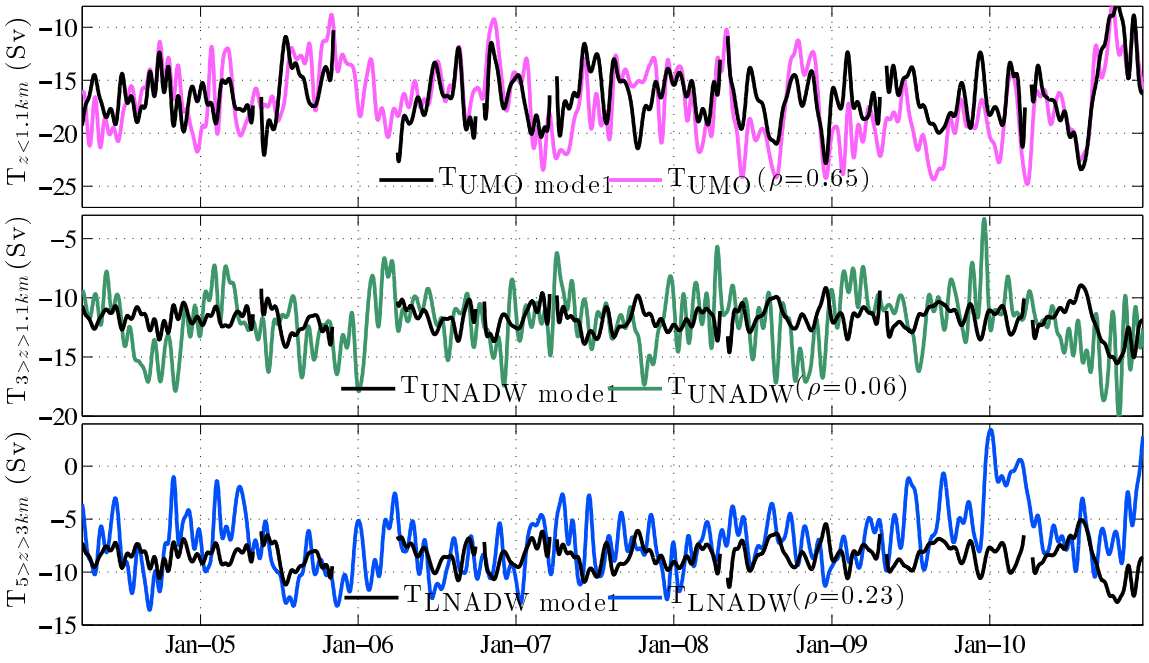

Figure 3.6: Upper mid-ocean transport observed (T_{UMO}, magenta) and attributed to the first baroclinic mode at the western boundary ($T_{UMO\ mode1}$, black). Upper North Atlantic Deep Water transport observed (T_{UNADW}, green) and attributed to the first baroclinic mode at the western boundary ($T_{UNADW\ mode1}$, black). Lower mid-ocean transport observed (T_{LNADW}, blue) and attributed to the first baroclinic mode at the western boundary ($T_{LNADW\ mode1}$, black).

The external transport is however redistributing the anomalies present in T_{INT} which produces some variability in T_{UNADW} and T_{LNADW}. The calculation of T_{UNADW} and T_{LNADW} is similar to T_{UMO} but integrated in the depth range of 1100–3000 m and 3000–5000 m respectively. T_{UNADW} and T_{LNADW} are composed of the internal, external and wedge transports. The external transport in each deep layer is expected to be twice as large as in the thermocline layer based on their vertical extent. In the deep layers, the mode 1 does not significantly contribute to the variance of the observed layers from the correlation of 0.06 and 0.23 in the upper and lower layers, respectively. Despite these low correlations, the standard deviations are not negligible as opposed to the deep T_{INT}. The standard deviations of T_{UNADW} and $T_{UNADW\ mode1}$ are 2.4 and 1.1 Sv respectively. In the lower NADW, the standard deviations are 2.9 and 1.2 Sv for T_{LNADW} and $T_{LNADW\ mode1}$. These deep contributions to T_{UNADW} and T_{LNADW} arise from the indirect effect of mode 1 processes on the shallow geostrophic transport given that the other components influencing T_{EXT} (e.g. T_{GS} and T_{Ek}) remained fixed.

To link the mode 1 variability to the MOC, we compare the upper geostrophic transport attributed to mode 1 ($T_{UMO\ mode1}$) and the observed MOC where Ekman is held constant. Ekman transport is fixed in order to isolate the geostrophic components of the MOC from the direct wind effects. A significant correlation of 0.30 is found, explaining 9% of the variance. This result underlines the importance of localized eddies and Rossby

waves in explaining some of the subannual variability of the MOC as opposed to longer timescale processes such as deep water formation rates.

3.3.6 Meridional extent of subannual transport anomalies due to westward propagating processes

The question arises as to what extent subannual variations of the MOC are meridionally coherent. From the zonal RAPID array, we cannot directly estimate meridional coherence. However we have shown that the dynamic height at Wb2 shows a high correlation (0.64) with nearby SSHA, while the mode-1 amplitude at Wb2 correlates slightly better (0.67) with SSHA. Using the reconstruction of interior transport from the first mode (first three modes) with correlations of 0.77 (0.81) with the observed interior transport, we see that mode-1 fluctuations are the primary drivers of meridional transport variability. This suggests that sea surface height variability can be used to explain some meridional transport variability along the western boundary of the Atlantic. By calculating the meridional coherence of sea surface height variations extracted along the 3900 m isobath (results not shown), we find that the sea surface height quickly becomes decorrelated with latitude. At three degrees north or south, the correlation is 0.2 which corresponds to the significance level (95%), suggesting that subannual variations of the MOC at 26.5°N quickly become decorrelated with latitude. The meridional scale (600 km) obtained from the north and south decorrelation scales is consistent with the zonal wavelength of 350–800 km of the 2D SSHA spectra assuming isotropic eddies.

3.4 Discussion

The question of the impact of eddies on the MOC arose from a series of prior papers on the topic. To evaluate the effect of eddy variability on the MOC transport, Wunsch (2008) relied on the covariability of SSHA and density anomalies to link the observed rms SSHA to the dynamically important first baroclinic mode. By assuming SSHA fluctuations of 16 cm near the Bahamas, which is characteristic of the maximum values found in the western basin, Wunsch (2008) predicted an rms transport (16 Sv) many times larger than found in the observations (3.1 Sv; Cunningham et al., 2007). Kanzow et al. (2009) attributed the transport variability difference to the decrease of SSHA and DHA variability approaching the boundary and estimated that at most 4.2 Sv of the transport variability could be attributed to westward propagating signals. Kanzow et al. (2009) calculated the upper limit of the effect of westward processes on the transport by interpolating the transport variability based on 2-year timeseries knowing the 15-year SSHA variability.

While the present study also observed a decrease in variability of the first baroclinic mode close to the boundary at 26.5°N, westward propagating anomalies are still responsible

for a substantial portion of the meridional transport variability above the thermocline. The influence of westward propagating signals on the meridional transport was thus assessed: 59% of the variance of the internal transport and 42% of the variance of the upper mid-ocean transport can be attributed to first baroclinic mode eddies and Rossby waves at periods of 80–250 days. These anomalies also explain 9% of the variance of the MOC in the absence of Ekman variability. The upper mid-ocean transport standard deviation attributed to mode 1 processes was found to be 2.6 Sv instead of the upper limit of 4.2 Sv found in Kanzow et al. (2009). By comparing eddy-permitting and non-eddying global ocean models, Hirschi et al. (2013) estimated that 20 to 30% of the MOC variability could be attributed to the unpredictable chaotic variability of eddies, Rossby and Kelvin waves. They expected to find a larger percentage attributable to chaotic signals if they were to use a model that is fully eddy-resolving. This result needs to be compared cautiously to our findings as the percentage of MOC variability in Hirschi et al. (2013) is defined as the ratio of chaotic MOC over total MOC standard deviations.

The effect of westward propagating signals on meridional transport matters when anomalies encounter the western boundary and displace isopycnals from their average depth. Eddies having mode-1 structure directly modulate the northward Antilles current and indirectly affect the southward DWBC mostly through the barotropic compensation. Previous studies also analysed the effect of eddies on the DWBC in Lee et al. (1996) and Johns et al. (2008). The presence of an anticyclone at the boundary for example may enhance the northward Antilles current and shift the DWBC offshore (Lee et al., 1996). This would be translated into an anticorrelation of the inshore vs offshore transports as found in Bryden et al. (2005a) and Meinen et al. (2013). In the present study focusing at the boundary, the effect on the deep geostrophic transport was reduced because propagating processes do not extend below 1200 m at the boundary. The interplay of westward propagating signals with the DWBC seems to be twofold. DWBC meanders are related to eddy events but the modal structure of anomalies may also be affected by the presence of strong shear between the Antilles Current and the DWBC. The DWBC is therefore partly responsible for the decrease in the vertical coherence of propagating anomalies limited to the shallowest 1200 m after they encounter it. In addition, baroclinic transport anomalies of propagating features may be transferred through the barotropic component into layers deeper than 1200 m. This compensation mechanism was identified by Bryden et al. (2009) through a significant correlation between the observed bottom pressure at Wb2 and the bottom pressure inferred from dynamic height anomalies. They demonstrated the presence of a barotropic compensation to baroclinic anomalies which is only significant at Wb2. The analysis of the western boundary dynamic is essential to understand at which longitudes the meridional barotropic compensation prevails.

The primary effect of westward propagating features was found on subannual timescales in a specified period range (80–250 days); interannual variability is less affected by mode

1 anomalies. This temporal distinction may facilitate the detection of large scale oceanic anomalies with important climatic effect from more localised transport variability attributed to inherently chaotic ocean dynamics. In this regard, the 30% MOC decline described by McCarthy et al. (2012) from early 2009 to mid-2010 and observed in the Ekman, upper mid-ocean and LNADW transports does not appear to be associated with westward propagating features. This can be seen from the anomalies present in T_{UMO} and T_{LNADW} in Fig. 3.6 but not in $T_{UMO\ mode1}$ and $T_{LNADW\ mode1}$. This event was associated with a strengthening of the southward thermocline transport and a decline in the southward LNADW, neither of which were captured by the mode 1 transports (Fig. 3.6). The temporal extent of the 2009–2010 event is longer than the period of maximum low-frequency energy (200 days) at Wb2 (Fig. 2.10). The longest period (250 days) that exhibits westward propagation may also help to disentangle and interpret any expected slowdown trend of the MOC, as predicted in the oceanic circulation of a changing climate with increasing greenhouse gases. The upper limit of the transport variability attributed to propagating features is 2.6 Sv. Any decadal variability or trend that may be found using extended continuous measurements as noticed in Smeed et al. (2014) and that is higher than the upper limit, may confidently be distinguished from the effect of propagating anomalies. This result assumes that eddy and Rossby wave regimes do not change with time, which may not be entirely true within a changing climatic system composed of increasingly extreme events.

The present study highlights the importance of considering eddies and Rossby waves to describe the subannual variability of the MOC and confirms their effect on the overturning circulation calculated within the RAPID program. Westward propagating anomalies play a significant role in the MOC variability at the latitude of the RAPID array and may modulate divergence/convergence of the meridional transport on short timescales (Sinha et al., 2013). The meridional coherence of the transport will be influenced by this variability and is found to decorrelate within three degrees of latitude. This analysis suggests that much of the subannual variability at 26.5°N will be local, as suggested by Bingham et al. (2007). In addition to the role of eddies in the export of nutrients, heat and hydrographic properties, the understanding of their effect on large scale circulation and on the climate system is of major importance to the current improvement of global circulation models ranging from eddy-permitting to eddy-resolving (Marsh et al., 2009; Hirschi et al., 2013). Further study on the interaction of westward propagating signals with the boundary may provide insight into the pathways of conversion or destruction of mesoscale energy in the ocean.

3.5 Conclusions

The large scale wave pattern identified by its period and wavelength is expected to influence the meridional geostrophic transport at the western boundary where the wave

loses its regular oscillatory structure. From the previous chapter the effect was predicted to be maximal in the shallowest 1200 m. The RAPID methodology was presented to calculate the internal and upper mid-ocean transports. The focus was done on $T_{INT\ mode1}$ and $T_{UMO\ mode1}$ considering only the effect of mode 1 propagating features at the western boundary. Propagating features of mode 1 structure are important for the geostrophic internal transport at subannual timescales in the thermocline layer but not below 1100 m. A correlation of 0.77 was found between T'_{INT} and $T'_{INT\ mode1}$. Including the barotropic compensation lowers the correlation between T_{UMO} and $T_{UMO\ mode1}$ to 0.65. The barotropic adjustment is redistributing some of the baroclinic variability to the deep layers which are not directly affected by the propagating features. This compensation is believed to happen around Wb2 where baroclinic anomalies affect the geostrophic transport. The standard deviation of the mid-ocean transport attributed to mode 1 processes is estimated to be 2.6 Sv whereas the observed variability of T_{UMO} is 3.4 Sv. A further study based on eddy tracking will help to determine more specifically their properties which evolve as they approach the boundary. This should in the future supplement our knowledge of the eddy heat transport and may help to refine its estimation knowing that most of its variability is attributed to the western boundary shallower than 700 m (Johns et al., 2011) which is the region of dynamical interest in the present chapter.

Chapter 4

Generation of internal waves by eddies impinging on the western boundary of the North Atlantic

4.1 Introduction

Mesoscale eddies in the ocean are ubiquitous and characterised at mid-latitudes by lengthscales of ∼100 km and timescales of days to months. Eddies are believed to play a central role in the redistribution of energy input by wind stress (1 TW), which is extracted from the oceanic circulation via baroclinic and barotopic instabilities before being dissipated through small-scale turbulence. The understanding of the link between energetic mesoscale processes and small-scale turbulence is fundamental to close energy budgets and refine mesoscale parameterisations.

The eddy energy can be dissipated through the bottom interaction which is believed to be the main process to remove eddy energy. According to the theory of geostrophic turbulence, which assumes no lateral boundaries, bottom drag is the primary mechanism dissipating energy from mesoscale eddies. Energy is input to the first baroclinic mode, then transfers to the barotropic mode at a horizontal scale close to the Rossby radius of deformation, before transferring to larger scales through an inverse cascade (Salmon, 1978). Recent observations from altimetry call this cascade into question (Scott and Wang, 2005), while estimates of dissipation from geostrophic flow by bottom drag are uncertain (0.2–0.8 TW, Sen et al., 2008). Another mechanism is considered in our work, which is the generation of internal waves by eddy geostrophic flow over a topographic rise at the western boundary within the thermocline. The first baroclinic mode flow is intensified in the thermocline; this mode is dominant in the open ocean and is still important at the boundary.

Eddies propagate westward at the linear Rossby wave speed in oceans which are not affected by strong currents such as the Gulf Stream, Kuroshio or ACC (Chelton et al.,

2011). Relying on the hypothesis of westward propagating eddies, Zhai et al. (2010) was able to quantify an eddy energy sink at the western boundary to be 0.1–0.3 TW from a reduced-gravity model. The prevailing mechanism by which eddy dissipation occurs was not determined in Zhai et al. (2010). The authors used a 1.5-layer model which excludes by initial assumption any potential interactions between flow and topography. The chaotic behaviour of eddies, which interact, disappear and merge between each other, hinders the observation of dissipation processes. The availability at the western boundary of two years of ADCP measurements associated with vertical profiles of current meters from the boundary to 100 km offshore associated with the altimetry renders possible the analysis of both internal waves and eddies.

One mechanism by which energy can be drained from the mesoscale eddy field is the generation of internal waves, which promotes dissipation and diapycnal mixing upon breaking. Internal waves may be generated when a geostrophic current flows over rough topography (Liang and Thurnherr, 2012; Brearley et al., 2013) in a process described by the linear theory of lee waves over small-scale abyssal hills (Bell, 1975). For steeper and taller topography, nonlinearities arise that render the energy transfer from geostrophic flow to internal waves less predictable (Baines, 1995; Klymak et al., 2010). Additionally, at the western boundary, internal waves may be radiated by hydraulic jumps resulting from the interaction of strong northward flow with Kelvin waves (Hogg et al., 2011).

At 26°N the Gulf Stream travels through the Florida Strait. Eddies are then not strongly affected by the Gulf Stream at this latitude and are able to propagate to the western boundary where they should dissipate some of their energy over the topography and where they encounter the southward deep western boundary current (DWBC) and northward Antilles current (Lee et al., 1996). Our focus will be on the 600 m deep topographic rise adjacent to the deep North Atlantic basin. The present study investigates the lee wave generation by eddy geostrophic flow within the thermocline, where eddy flows are stronger than abyssal currents, and so where the eddy energy removal should be stronger. Eddy pathways at the western boundary are first analysed from an eddy tracking product in section 4.3. An anticyclone-cyclone eddy decay at the western boundary is then studied from the altimetry and mooring array data in section 4.4. A dependence to the eddy polarity of the deep flow amplitude is found. The shear spectra and dissipation rate are analysed in section 4.5 given the eddy polarity. The internal wave frequency and direction of propagation are then analysed in section 4.6. Anticyclones are found to enhance the generation of lee waves. Additionally the anticyclonic background vorticity, known to trap near-inertial waves, is demonstrated to allow a larger frequency range of near-inertial waves following the passage of a storm in the vicinity of the ADCP.

4.2 Data and methods

4.2.1 The western boundary region

Current meters

A mooring array at the western boundary of the North Atlantic at 26.5°N is used from May 2010 to November 2011. The array is composed of 5 moorings (Fig. 4.1) Wba, Wb1, Wb2, Wb3 and Wb4 located at 13, 17, 25, 49 and 108 km from the coast in waters of 595, 1394, 3796, 4840 and 4713 m, respectively. The latitude of the array is 26.5°N but Wba is shifted slightly northward onto the top of a topographic rise at 26.53°N. Current meters are deployed on Wb1, Wb2, Wb3 and Wb4 including Aanderaa RCM-7s/RCM-11s, NorTek Aquadopps, InterOcean S4s and SonTek Argonaut and sampled every 30 minutes. One Broadband (75 kHz) upward looking R.D. Instruments Acoustic Doppler Current Profiler (ADCP) is deployed in waters of H = 595 m at Wba. Velocities are estimated every 30 minutes in 16-m bins from the instrument depth at 595 m to 59 m. Above 59 m is the shadow zone where reliable velocities are not retrieved due to sidelobe contamination by the surface reflection. Sound speed and magnetic variation corrections are applied to the ADCP data which are also despiked. Using full depth velocity measurements at Wba, the barotropic and baroclinic components are calculated at each time step as the vertically averaged velocity and as the anomaly to this average for each depth, respectively.

Hydrographic data

Buoyancy frequency profiles are calculated from Sea-Bird Electronics CTD (Conductivity, temperature and depth) casts from nine cruises in the North Atlantic western boundary from 2006 to 2012 (Table 4.1) and are made available by the National Oceanic & Atmospheric Administration (NOAA) through the WBTS (Western Boundary Time Series) data (`ftp://ftp.aoml.noaa.gov/phod/pub/WBTS/Global_Class/`). The description of the pre-cruise calibrations, data acquisition and processing using SEABIRD SBE Data Processing are fully described in the cruise reports also available on the data portal. Post-cruise sensor calibrations are applied to correct for the sensor drifts. Post-cruise CTD data processing removes the spikes and density inversions due to package movements. The average profile (Fig. 4.2) is used for the buoyancy frequency mean $\bar{N}(z)$ which has two peaks in stratification of (0.012 and 0.09 s^{-1}) at 50-150 m and 200-250 m respectively and a bottom value of 0.004 s^{-1}. The standard deviation of the buoyancy frequency is added showing a large variability around the first peak in the top 150 m where the atmospheric influence is expected to be the largest.

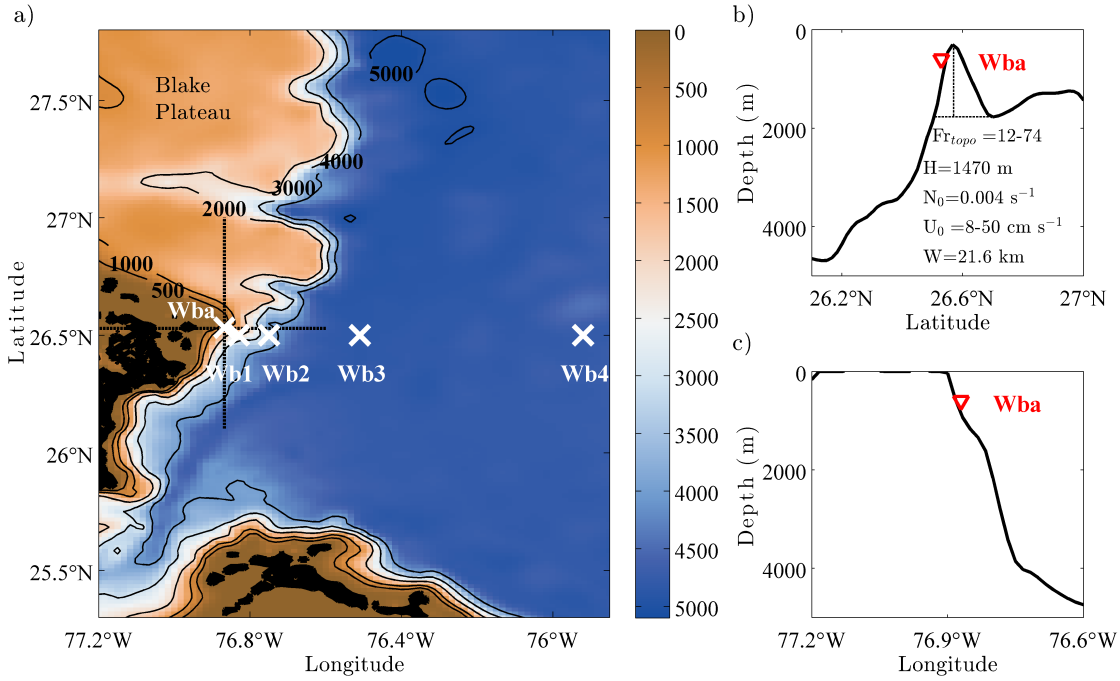

Figure 4.1: (a) Bathymetry of the western boundary of the North Atlantic around 26.5°N with Great Abaco and Eleuthera island at the west and south respectively. The mooring array (Wba, Wb1, Wb2, Wb3 and Wb4) is marked in white crosses. The two black dashed lines indicate the 1D cross sections around Wba displayed in (b) and (c) across the longitude 76.87°W and the latitude 26.53°N, respectively. The bathymetry is extracted from ETOPO1 provided by NOAA.

Wind data

The wind speeds at 10 m from the sea surface are taken from the global atmospheric reanalysis ERA-interim (Dee et al., 2011) made available by the European Centre for Medium-Range Weather Forecasts (ECMWF) at `http://data-portal.ecmwf.int/data/d/interim_daily/`. Zonal and meridional components of wind stress are selected at the closest data point to Wba, at 26.5°N, 76.5°W.

Topography

The topography at the western boundary of the RAPID array at 26.5°N is displayed in Fig. 4.1. The continental slope east of Great Abaco at 26.5°N is particularly steep deepening from 200 m to 4500 m over 25 km (from 76.93°W to 76.68°W). Wba is located on the topographic rise of the Bahamas escarpment which is 21 km long in the meridional direction as defined by the 2000 m isobaths. North of Wba the 2000–4000 m isobaths run north to south but south of 26.5°N the direction of maximum gradient is shifted in the southwest-northeast direction. The presence of two escarpments with shallower depths of 1600 m at 26.63°N and 26.73°N blocks the Deep Western Boundary Current (DWBC) in the Wba–Wb2 section as described in Johns et al. (2008). These same

Cruise	Station	Date	Depth (m)	Latitude (°N)	Longitude (°W)
Ronald H. Brown AB0603	30	19 Mar 2006	597	26.516	76.899
R.V. Seward Johnson AB0609	14	28 Sept 2006	307	26.525	76.892
Ronald H. Brown AB0703	34	31 Mar 2007	300	26.527	76.890
Ronald H. Brown AB0709	23	18 Sept 2007	310	26.525	76.891
R.V. Seward Johnson AB0804	13	8 Apr 2008	520	26.516	76.876
Ronald H. Brown AB0904	1	18 Apr 2009	312	26.525	76.892
RRS Discovery D345	9	23 Nov 2009	463	26.513	76.893
Ronald H. Brown AB1202	28	24 Feb 2012	313	26.525	76.892
UNOLS ship Endeavor AB1209	8	26 Sept 2012	449	26.525	76.885

Table 4.1: Cruise from 2006 to 2012 with corresponding cast taken close to Wba.

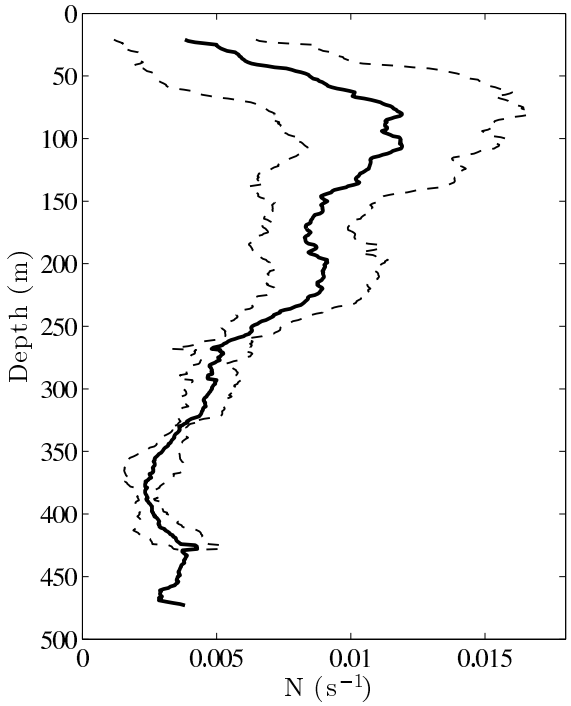

Figure 4.2: Average N profile (thick line) and $\pm$ one standard deviation (dashed lines) at the ADCP location (Wba) obtained from 9 CTD casts during western boundary cruises provided by the Western Boundary Time Series data. The bottom value of $N_0 = 4 \times 10^{-3}$ s^{-1} is used for the deepest 100 m at Wba.

escarpments will limit the influence of southward flow associated with cyclonic eddies at the boundary.

4.2.2 Internal waves and parameterisation of the dissipation rate

Lee wave generation

The linear theory of lee waves, developed by Bell (1975) and Gill (1982), is first presented assuming a small scale hill before extending the theory to nonlinear behaviour in the case of increased topographic steepness and scales. The linear theory holds in the deep ocean where abyssal hills have horizontal scale W of $\mathcal{O}(10$ km), and vertical scale H of

$\mathcal{O}(100$ m). In this case, lee wave solutions are linearly dependent on the topography. Lee wave solutions must satisfy the dispersion relation, which for a rotating ocean is

$$m^2 = k^2(N^2 - U^2k^2)/(U^2k^2 - f^2), \tag{4.1}$$

where m and k are the vertical and meridional wavenumbers, respectively and N and U are the buoyancy frequency and horizontal velocity at the bottom. This dispersion relation is two dimensional in z and y only, where the y direction is perpendicular to the crests of the abyssal hills. Once the waves are created, they transport energy upwards from the boundary for the positive m solution as opposed to the evanescent solution in the case of negative m. In the present study, lee waves can transport eddy energy from depths neighbouring the topographic hill to shallower depths which will then affect the lee wave source, i.e. the eddy mean current. The restriction on the vertical wavenumber imposes a condition on the meridional wavenumber $U/N < k^{-1} < U/f$. The lower (U/N) and higher (U/f) limits compare the horizontal wavelength with the distance travelled during one buoyancy and one inertial period, respectively.

A high pressure region appears on the side of the topographic hill facing the current. The vertical component of the current is hindered by the stratification. In the lee of the hill, a low pressure arises due to the acceleration of the restoring buoyancy. A force results on the topography from the pressure gradient which is balanced by a drag on the mean flow. This drag is attributed to the internal wave field. The form drag in N m^{-2} is defined by integrating the pressure anomaly multiplied by the topographic slope over the area of the hill. The vertical energy flux (E_z) or the vertical transport of horizontal momentum by the lee wave in W m^{-2} corresponds to the drag multiplied by the velocity (Gill 1982), with ρ_0 being a reference bottom density

$$E_z = \frac{1}{2}\rho_0 U h_0^2[(N^2 - U^2k^2)(U^2k^2 - f^2)]^{1/2}. \tag{4.2}$$

The linear theory applies in the presence of subcritical topography ($\mathrm{Fr}_{\mathrm{topo}} << 1$) and in the case of a gentle slope ($H << W$). The topographic Froude number ($\mathrm{Fr}_{\mathrm{topo}} = NH/U$) — also referred to as the steepness parameter — allows us to identify when the transport is able to overcome the topography and the stratification to generate lee waves. This parameter can be defined by applying the Bernouilli equation over the seamount (Gill, 1982) which gives an upper limit for the pressure increase over the mountain related to a maximum vertical displacement of U/N. This vertical displacement limit means that water deeper than the maximum displacement from the top of the hill cannot flow over the seamount and is blocked by the feature. In our case on a ridge, this water may then flow around the eastern side of the feature for a northward eddy flow.

Nonlinearities in the lee wave theory arise mostly for critical ($\mathrm{Fr}_{\mathrm{topo}} \sim 1$) and supercritical topography ($\mathrm{Fr}_{\mathrm{topo}} > 1$). In these cases the flow can be blocked on the upstream but also downstream sides and some instabilities and wave breaking appear on the lee

side (Baines 1995). The upstream blocking may disturb the stratification and upstream flow rendering the lee wave generation less predictable. Lee waves over large topography have been studied from tidal flow over knife-edge topography (Llewellyn Smith and Young, 2003) or from steady flow over a Gaussian shape feature (Klymak et al., 2010). Despite the supercritical Fr_{topo} (12–75) found here for velocities above 8 cm s^{-1} and with $N = 0.004$ s^{-1} and $H = 1470$ m, high-mode lee waves (vertical wavelength m shorter than H or D) may still be generated over the topographic rise (Klymak et al., 2010).

The propagation of internal waves can also be linked to the existence of a hydraulic jump (Baines, 1995). This is evaluated through the internal Froude number ($\mathrm{Fr}_{\mathrm{int}}$) defined as the ratio of the flow speed over the internal wave phase speed. In addition to the generation of lee waves analysed with the topographic Froude number, the internal Froude number may provide some information on the direction of wave propagation. The criticality of the flow can be estimated from $\mathrm{Fr}_{\mathrm{int}}$ with a subcritical, critical and supercritical flow corresponding to $\mathrm{Fr}_{\mathrm{int}} < 1$, $\mathrm{Fr}_{\mathrm{int}} = 1$ and $\mathrm{Fr}_{\mathrm{int}} > 1$, respectively. In the case of a subcritical flow, the waves can propagate either upstream or downstream whereas they only propagate downstream for a supercritical flow (Baines, 1995). In our case, flow measurements over an extended period associated with the presence of internal waves will indicate whether waves are expected to propagate upstream over the ADCP. The critical internal Froude number will be linked to a critical flow speed if the wave phase speed is unknown or if no assumption is made of the wave modal structure.

Finescale parameterisation

The wind and tidal energy enters the oceanic system at large scales before being dissipated at small scales. The energy dissipation can be directly measured or inferred from a parameterisation given the characteristics of the internal wave field. The rate of dissipation of turbulent kinetic energy (ϵ) can be estimated from measurements at centimetre scale of velocity shear using microstructure profilers (Oakey, 1982). Subsequently, turbulent mixing is defined from the dissipation rate via the diapycnal diffusivity as in Osborn (1980). In the absence of such measurements, the knowledge of the background internal wave field can be used in a finescale parameterisation to compute ϵ (Gregg, 1989; Polzin et al., 1995; Polzin et al., 2014). The parameterisation relies on the energy transfer from internal waves of large vertical scales ($\mathcal{O}$(100 m)) to smaller scales ($\mathcal{O}$(10 m)) via wave-wave interaction as modelled by Henyey et al. (1986). At small scales, the waves break and dissipate the energy at a similar rate to the energy transfer. In this model the shear spectrum is quantitatively compared to the Garrett and Munk (GM) spectrum as defined in Garrett and Munk (1975) and Gregg and Kunze (1991) which is used to represent a constant background internal wave field in the open ocean. The GM vertical wavenumber spectrum is almost flat and has a sharp decrease at a roll-off vertical wavenumber around 10 m.

The dissipation rate (ϵ) in W kg^{-1} is obtained as in Gregg et al. (2003) from the finescale parameterisation using the shear to strain variance ratio (R_ω) and the latitudinal correction term ($j(f/N)$), such that

$$\epsilon = \epsilon_0 \frac{< V_z^2 >^2}{< V_z^2 >_{GM}^2} h_1(R_\omega) j(f/N) \tag{4.3}$$

$$h_1(R_\omega) = \frac{3(R_\omega + 1)}{2\sqrt{2} R_\omega \sqrt{R_\omega - 1}} \tag{4.4}$$

$$j(f/N) = \frac{f \cosh^{-1}(N/f)}{f_0 \cosh^{-1}(N_0/f_0)} \tag{4.5}$$

with $\epsilon_0 = 6.73 \times 10^{-10}$ W kg^{-1} and $N_0 = 5.2 \times 10^{-3}$ rad s^{-1} being the canonical GM dissipation rate and buoyancy frequency, respectively, and f_0 the inertial frequency at a latitude of 30°N. N is taken as the depth averaged profile displayed in Fig. 4.2. The shear-to-strain variance ratio gives an indication of the internal wave's aspect ratio and its frequency content (Polzin et al., 1995). Near-inertial waves contain a high shear which corresponds to a near vertical wavevector, whereas internal waves with frequency close to the buoyancy frequency have a higher strain with a near horizontal wavevector. This ratio also represents the horizontal kinetic energy of the wave divided by the potential energy (Fofonoff, 1969). Due to the absence of strain estimates, the canonical GM value of R_ω=7 is assumed. Our aim is to relate variations in dissipation rate to mesoscale conditions. The sensitivity of the absolute dissipation rate to the shear-to-strain ratio is further discussed in the results section. Variations to this ratio will undoubtedly lead to different estimates of the dissipation rate as described in Kunze et al. (2006). The latitudinal correction provides a sharp reduction of the dissipation rate and diffusivity when approaching the Equator (Gregg et al., 2003) but is close to the 30° reference at the 26.5°N latitude of this study.

The shear (V_z) is calculated at each 16 m bin and is normalised by the time-average stratification $\bar{N}(z)$. Following Kunze et al. (2006), the buoyancy frequency normalized shear variance is defined by integrating the shear spectrum $S[V_z/\bar{N}]$ from a minimum to a maximum vertical wavenumber (k_1 and k_2, respectively)

$$< V_z^2 > /\bar{N}^2 = \int_{k_1}^{k_2} S[V_z/\bar{N}](k_z) dk_z, \tag{4.6}$$

where $< \cdot >$ denotes the integration over vertical wavenumber. A first guess for the vertical wavelength limits (λ_1=500 m and λ_2=33 m) is determined from the fundamental (k_1=0.013 rad m^{-1}) and Nyquist wavenumbers (k_2=0.19 rad m^{-1}), respectively given by the the ADCP range and resolution and also in order to avoid the roll-off part of the spectrum. Inspection of the wavenumber spectra refines the estimates from 80 to 500 m without strongly affecting the dissipation rate. The shear variance can be compared to the GM value

$$< V_z^2 >_{GM} / \bar{N}^2 = (3\pi/2) E_0 b j_\star \int_{k_1}^{k_2} k_z^2 (k_z + k_{z^\star})^{-2} dk_z \tag{4.7}$$

with the reference wavenumber $k_{z^\star} = (\pi j_\star N)/(bN_0)$, the mode number $j_\star$=3, the scale depth of the thermocline b=1300 m and the dimensionless energy level E_0=6.3×10^{-5}.

The diapycnal eddy diffusivity K_ρ is inferred from the dissipation rate (Eq. 4.3) as in Osborn (1980)

$$K_\rho = \Gamma \epsilon / N^2. \tag{4.8}$$

This relation is obtained from the turbulent energy equation assuming a steady-state which provides a relation between the production of turbulent kinetic energy by the vertical shear with the dissipation rate and the buoyancy flux. The mixing efficiency Γ is taken at 0.2 in order to infer the diapycnal mixing of the buoyancy flux from the calculated dissipation rate.

4.2.3 Eddy tracking and eddy census

Eddy tracking methodology

The detection and the tracking of eddies from satellite altimetry have been implemented based on various contours of dynamical fields. For example, several methods have been developed using contours of SSH or contours of the Q parameter, which is derived from the relative vorticity calculated from SSH (Isern-Fontanet et al., 2003). The Q parameter is decomposed in a deformation and vorticity terms and allows the detection of areas with relatively important rotation (Isern-Fontanet et al., 2003). The Okubo-Weiss parameter (W), which is equivalent to the Q parameter for a horizontally nondivergent flow (Chelton et al., 2007), is defined from the spatial derivatives of the surface geostrophic velocity terms u and v. Eddies are characterised by regions of negative W, which means that the vorticity is higher than the strain. As discussed in Chelton et al. (2011), there are several limitations of this method. Firstly a threshold needs to be defined to detect W contours and the optimal threshold might differ in various parts of the ocean. An inappropriate choice of threshold might lead to under or over eddy detection. Another problem concerns the noise in the method which comes from the double differentiation of SSH in the calculation of the W parameter. The last limitation arises from the different results of detected eddies obtained using W contours or SSH contours. Chelton et al. (2011) implemented a procedure of eddy tracking based directly on the SSH Aviso Reference product to overcome the three shortcomings of the Okubo-Weiss method. The procedure is implemented on SSH with a 1/4°×1/4° resolution every 7 days from October 1992 to April 2012. Large-scale signals (larger than 20° of longitude and 10° of latitude) are filtered out before applying the eddy tracking (Chelton et al., 2011). This tracking product, which is made available on `http://cioss.coas.oregonstate.edu/eddies/`, will be used throughout the present study.

The eddy amplitude and radius are both defined in the tracking product. The eddy amplitude is calculated from the absolute difference of the SSH maximum/minimum with the averaged height of the outermost eddy contour. The algorithm searches for closed contours of SSH by using SSH thresholds from -100 to 100 cm incremented every 1 cm. The identified contours satisfy criteria on the size, shape and amplitude of the regions to ensure the coherence of the closed contours with an eddy structure. The outermost eddy contour is determined from the structure which satisfies these criteria. The eddy radius is calculated as the radius of a circle with the same area as the SSH contour with the maximum averaged geostrophic speed. This method is selected in Chelton et al. (2011) because of its independence from any assumption on the eddy shape.

The tracking product does not deal with reappearing eddies, which are in part due to eddy interaction affecting the eddy shape (Chelton et al., 2011). The exact proportion of reappearing eddies is not known and the estimated eddy lifetime is considered to be at the lower limit of the true eddy lifetime. Our aim is to study eddies before their decay, and for this reason it is fundamental to know what is the minimal eddy scale or how the decay of an eddy is defined in the tracking method. A radius minimum of 36 km is found within a week before the eddy decay for all the detected eddies at the western boundary in section 4.3.3. The amplitude minimum for the same eddy ensemble is 1 cm. These two minima agree with the amplitude minimum of 1 cm defined in the tracking product criterion and with the lowest detected eddy radius estimated to be 40 km at 30° of latitude in Chelton et al. (2011). The radius minimum is inherent to the spatial filtering applied in the objective analysis to produce SSH in the AVISO product.

Eddy census

A vertical profile of temperature and salinity anomaly (θ' and S') can be estimated for each anticyclone and cyclone detected in the neighbourhood of the RAPID moorings. Similar results have been obtained in the past from CTD transects (Simpson et al., 1984) using a method of differential anomaly, which estimates hydrographic anomalies relative to the distance to the eddy centre. The development in the last decade of Argo floats associated with altimeters allowed the study of the eddy vertical structure in the top 1500 m (Qiu and Chen, 2005; Chaigneau et al., 2011; Souza et al., 2011). In this section, we will also define a differential anomaly method but referenced against the temporal means ($\bar{\theta}$ and $\bar{S}$) at the mooring instead of using a climatology as in Simpson et al. (1984). The several years of measurements, 8 years at Wb5 and Mar1 and 4 years at Wb4, allow this referencing. Our method estimates the eddy structure at one location for a varying distance to the eddy centre. Considering full-depth moorings also allows the analysis of the entire eddy vertical extent without being restricted to 1500 m. In our case a symmetry is assumed in the meridional direction and θ and S profiles are projected on the eddy zonal direction. This last assumption is mainly motivated by our

interest in studying the eddy meridional heat flux at 26°N. The temporal evolution of the eddy lengthscale is taken into account by defining the radial distance in percentage of the eddy radius as the distance from the mooring to the eddy centre normalised by the instantaneous eddy radius (r).

The eddy tracks defined by the tracking product are retained to estimate θ and S profiles when the eddy centre is within a distance of $1.5r$ from the mooring. The number of profiles during anticyclonic (cyclonic) conditions at Wb5 are 134 (126) when an eddy centre detected by SSHA is within 1.5 eddy radius from the mooring from March 2004 to November 2012. These profiles correspond to the passage of 16 anticyclones and 18 cyclones identified close to Wb5. The number of profiles are reduced to 66 (39) if a distance of one radius between the mooring and eddy centre is considered. The θ and S profiles for each eddy are first linearly interpolated radially in each eddy section. For a number of profiles which represents at least 40% of the radius in each leg, a fitting is then computed at each depth on θ and S using a 7th degree Lagrange polynomial as in Souza et al. (2011). This polynomial choice provides a Gaussian shape to the mesoscale structure. The geopotential height referenced to the bottom is determined from the θ and S profiles. The geostrophic velocity is calculated from the thermal wind relation assuming a null reference velocity at the bottom of each mooring.

4.3 Eddy pathways and census at the western boundary

In this section, the eddy tracking product is first used to identify eddies which travel at the western boundary. This analysis will inform us on the eddy pathway and on their decay location. In addition, the eddy amplitude and radius are analysed before the eddy decay. Composite eddies are also constructed at two locations (Wb4 and Wb5) using the eddy tracks.

4.3.1 Pathways of mesoscale processes

To study the characteristics of mesoscale processes which affect the hydrography around Wb4 and Wb5, the eddy tracks that travel through the area delimited from 25.5 to 27.5°N and from 71 to 77°W are analysed. In previous studies (Sangrà et al., 2009; Kurian et al., 2011), eddy tracks were used to follow eddy pathways subsequent to their generation known to be mostly at the eastern boundaries (Chelton et al., 2011). In the present chapter, the focus is instead at the western boundary; the interest is then on eddy characteristics prior to their decay. The eddy pathways are first studied from SSHA for the full period between May 1992 and December 2012 in Fig. 4.3. The locations of their birth and decay relative to their lifetime are also summarised in Table 4.2. The temporal extent will then be reduced to the mooring deployment from March 2004 in the section 4.3.4. During the 20 years of coverage by altimetry, a total of 182 eddies are observed in this area with 97 cyclones and 85 anticyclones. From the total

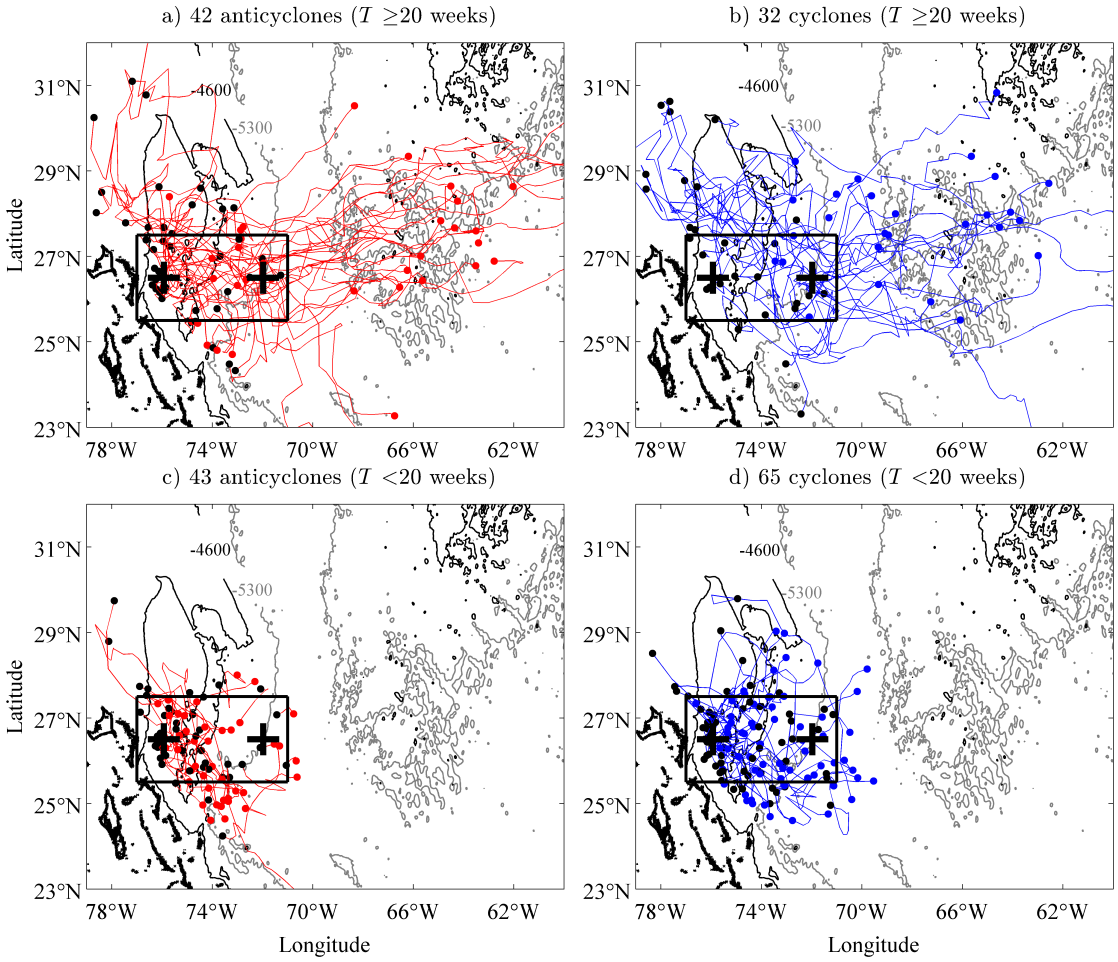

Figure 4.3: Eddy paths of anticyclones (red, a and c) and cyclones (blue, b and d) which travelled within the area identified by the black rectangle (from 25.5 to 27.5°N and from 71 to 77°W) between May 1992 and December 2012. Eddies with a lifetime longer (shorter) than 20 weeks are displayed in top (bottom) panels. The last and first eddy locations are marked (black and red/blue points, respectively). The 4600 m contour (thin black line) indicates the Blake-Bahama outer ridge located between the mooring Wb4 and Wb5, both marked by the black crosses.

number of cyclones/anticyclones, the equipartition of the eddy polarity seems to prevail.

The eddy tracks in Fig. 4.3 suggest that most eddies (58%, Table 4.2) are created locally close to the western boundary within 77 and 72°W. Unexpectedly the majority (82%) of these eddies are short-lived with a lifetime less than 20 weeks. Most of the short-lived eddies (64%) are created within the latitudinal band of 25 to 27°N with a significant amount of cyclones (28%) created north of this latitudinal band. These eddies should not contribute considerably to the water mass properties as they decay within several latitudinal and longitudinal degrees from their generation area. However the knowledge of their region of disappearance is informative and helps to illuminate the pathway of eddy energy as studied in section 4.5. Despite the large proportion of short-lived eddies

decaying within the latitudinal range around Wb4 from 25 to 27°N (67%), most short-lived eddies created southward of this band propagate northward as only 3 of the 12 eddies created in this region decay southward of 25°N. This observation is independent of the eddy polarity. The northward propagation of decaying eddies is not restricted to short-lived eddies as longer lived eddies also disappear poleward of 27°N. This remark is particularly true for very long-lived eddies defined with a lifetime greater than 50 weeks. Out of these 22 eddies, 74% of them decay northward of 27°N whatever their latitude of generation, given that they have to travel southward of 27°N in their lifetime.

The tendency of eddies of both polarities to propagate northward at the boundary is indicative that the image effect is not the dominant process in the eddy propagation at the boundary. Under the image effect, anticyclones and cyclones would be expected to propagate northward and southward, respectively (Kundu et al., 2012). Instead the influence of the Antilles Current may partly contribute to the northward advection of these eddies. At 26.5°N the mean Antilles Current extends to ∼100 km offshore to 76°W (Fig. 2.1). It was found in previous studies (Gunn and Watts, 1982; Lee et al., 1996) that the mean Antilles Current is highly dependent on the presence of eddies. The use of the zonal mooring array may not be sufficient to elucidate the effect of the Antilles Current on the eddy paths.

A large number of eddies (45%) vanish eastward of 75°W. This longitude, 200 km off the coast, is close to the mean DWBC limit (Figure 2.1) and to the location of the Blake-Bahama Ridge (Fig. 4.3). These eddies may interact with the mean DWBC as found in Lee et al. (1996). This interaction might be independent of their lifetime as eddies from each temporal bin decay eastward of 75°W. On the other hand, 55% of the eddy ensemble decay west of 75°W which means that these eddies may reach the western boundary and interact with the topographic rise described in Fig. 4.1. The interaction of eddies with the topography at the western boundary is the subject of the next sections.

4.3.2 Meridional drift of eddy pathways

Despite the equipartition of cyclones/anticyclones in the eddy ensemble, eddies classified by their duration do not follow the same pattern. For example, very long-lived eddies created east of 65°W are mostly anticyclonic (67%) rather than cyclonic (33%). On the other hand, short-lived eddies generated west of 65°W follow an opposite distribution with more cyclones (60%) than anticyclones (40%) as also seen in Fig. 4.3c and d. Two processes may be responsible for the non equipartition of short and very long-lived eddies detected within the box around Wb4 and Wb5. First anticyclones and cyclones are expected to be created north and equatorward of the Gulf Stream, respectively because of the negative and positive vorticity associated with meanders of the mean current (Chelton et al., 2011). Eddies pinching off southward of the Gulf Stream would preferentially be cyclonic and may contribute to the cyclonic over representation

		Cyclone	Anticyclone	Cyclone t<20 weeks	Anticyclone t<20 weeks	Cyclone 50>t>20 weeks	Anticyclone 50>t>20 weeks	Cyclone t>50 weeks	Anticyclone t>50 weeks
	Total	97	85						
Created	East of 65°W	11 (11%)	17 (20%)	0	0	5	5	6	12
	72 to 65°W	31 (32%)	17 (20%)	16	6	12	10	3	1
	77 to 72°W	55 (57%)	51 (60%)	49	38	6	13	0	0
Created	South of 25°N	6 (6%)	12 (14%)	5	7	0	4	1	1
	25 to 27°N	51 (53%)	41 (48%)	42	28	7	12	2	1
	North of 27°N	40 (41%)	32 (38%)	18	9	16	12	6	11
Decay	East of 75°W	44 (46%)	38 (45%)	31	21	11	10	2	7
	77 to 75°W	42 (43%)	40 (47%)	31	21	7	13	4	6
	West of 77°W	11 (11%)	7 (8%)	3	2	5	5	3	0
Decay	South of 25°N	4 (4%)	5 (6%)	2	1	2	1	0	3
	25 to 27°N	57 (59%)	45 (53%)	44	29	11	15	2	1
	North of 27°N	36 (37%)	35 (41%)	19	14	10	12	7	9

Table 4.2: Number of cyclones and anticyclones created in three longitudinal and latitudinal bands and decaying in these bands. These eddies travel through the box 25.5 to 27.5°N and from 71 to 77°W from May 1992 to December 2012.

of short-lived eddies. The significant amount of these short-lived eddies created between 77 and 65°W, which are generated northward of 27°N, support this hypothesis. Their generation is however southward of 30°N, whereas the Gulf Stream is expected to flow northward of this latitude around 70°W, this process may thus not be fully responsible for the greater number of cyclones in the short-lived populations.

A second process, which can account for the large proportion of anticyclones in long-lived eddies, results from the beta effect (Cushman-Roisin and Beckers, 2011). This effect deflects meridionally the eddy propagations from a zonal direction as observed in the eastern regions of Indian, Atlantic and Pacific Oceans in Morrow et al. (2004). The beta effect arises for large scale eddies affected by the meridional gradient of planetary vorticity. In a cyclone, a particle displaced to the west (east) from the north (south) regions of the eddy will experience a decrease (increase) of planetary vorticity. To conserve its potential vorticity, this particle will acquire cyclonic (anticyclonic) relative vorticity which will subsequently deflect the cyclone poleward. The opposite effect in anticyclones will deviate eddies equatorward. The equatorward shift of the 6 long-lived anticyclones, which originate northward of 27°N around the Mid-Atlantic Ridge (Fig. 4.3), can be a consequence of the meridional gradient of planetary vorticity.

4.3.3 Eddy radius and amplitude

The eddy radius and amplitude are displayed against the number of days prior to the decay for varying eddy lifetime and polarity in Fig. 4.4. Long-lived eddies, with a lifetime greater than 20 weeks, have a larger radius and amplitude than short-lived eddies. The enhanced strength of long-lived eddies compare to short-lived eddies seen in the mean amplitude of 9 and 6 cm, respectively might be reflected in the amplitude of the eddy-generated internal waves around Wba. As the eddies decline, their radius and amplitude evolve differently. The decrease of the radius from its long-term mean starts at around 40 days whereas the decrease of the amplitude starts later at 15 days. This

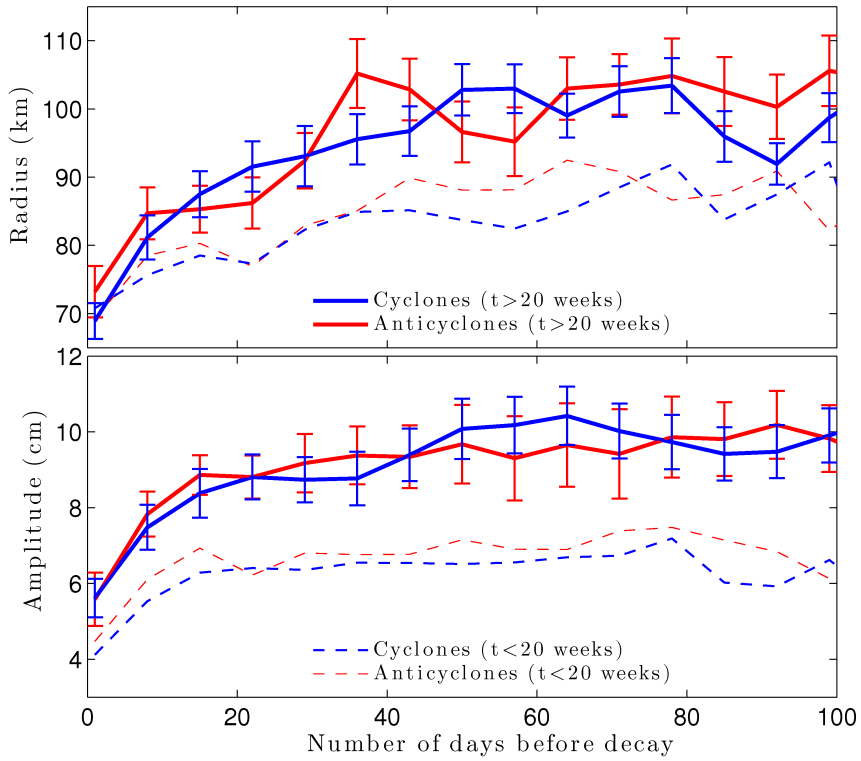

Figure 4.4: Eddy radius (km, top) and amplitude (cm, bottom) of anticyclones (red) and cyclones (blue) which travelled within 25.5 to 27.5°N and 71 to 77°W from May 1992 to December 2012. The averages are displayed for an eddy lifetime below (thin dashed lines) or above (thick lines) 20 weeks against the number of days before the eddy decay. Standard errors are indicated by the vertical lines for long-lived eddies.

period of 25 days is characterised by an acceleration of surface geostrophic velocities as the constant eddy amplitude is associated with a decreasing eddy radius, which has the effect of increasing the SSHA lateral gradient. The faster reduction of eddy radius compared with the amplitude might partly be a consequence of the constant movement of incoming eddies, which could reduce the length scale of the blocked eddy at the boundary.

4.3.4 Eddy census

Having detected eddy tracks around Wb4 and Wb5, an eddy composite of θ and S is constructed from the identified tracks. The vertical structure of a composite cyclone and anticyclone at Wb5 for θ' and the corresponding geostrophic velocities inferred from the thermal wind relation are displayed in Fig. 4.5. The radial distance of the composite eddy in Fig. 4.5 is defined in percentage of the instantaneous radius calculated by the tracking product. The anticyclonic composite at Wb5 reveals an anomaly of 1.4°C in the main thermocline from 600 to 800 m and another maximal anomaly of 1.6°C in the seasonal thermocline from 100 to 200 m. The deeper maximum is shifted to the western

section of the anticyclone but its extent is elongated further away from the eddy centre in the eastern section. The seasonal thermocline maximum follows the same pattern than the main thermocline maximum. For the cyclonic deep maximum (-1.4°C), the same westward shift is observed as for the anticyclone. The shallow maximum (-2.2°C) is however stronger and more elongated in the composite western section of the cyclone. An anomaly of ±0.1°C is still found at 2000 m in both composites.

An eddy composite is also computed for the salinity (not shown) at Wb5. In the main thermocline, maxima of ±0.19 are observed for both polarities and these maxima have a similar radial extent as for θ'. The upper (400 m) and lower (1000 m) limits of the maxima are more strongly defined than for θ' and S' is reduced below 0.02 deeper than 1000 m. A S' maximum is not observed in the seasonal thermocline of the anticyclone as found in θ'. For the cyclone however, a peak of -0.12 is found around 100 to 300 m. This minimum is deeper than the peak in θ' and weaker than the main thermocline peak of S'. From θ and S, the geostrophic velocity is calculated with the caveat that ageostrophic and centrifugal components may also affect the eddy centre in the case of large Rossby number (Kurczyn et al., 2013). Geostrophic velocities referenced to the bottom are displayed for both composites in Fig. 4.5. The meridional geostrophic velocities are within 10 cm s^{-1} for the cyclone with the maxima found at the edges of the eddy centre. The largest velocities around 30 cm s^{-1} are found in the western section of the anticyclone.

The eddy profile at Wb5 is expected to be representative of the eddy behaviour in the ocean interior. At this longitude, 500 km from the coast, western boundary currents comprises of the DWBC and Antilles Current should not strongly affect the eddy path and structure. An eddy composite at Wb2 or Wb3 would provide some information on the varying vertical structure found to be mostly represented by higher baroclinic modes than the first one in the second chapter. Unfortunately, their proximity to the coast prevents the implementation of a full composite, particularly its eastern section. At Wb4, however, located 100 km from the coast in water 700 m shallower than at Wb5, an eddy composite may still bring some information on how an eddy evolves as it approaches the boundary. In addition, by following the method of meridionally projecting eddy profiles onto a zonal transect, the eastern eddy section at Wb4 would be expected to interact with the mean DWBC observed to extend ∼100 km offshore from the mean current profile in Fig. 2.1.

The reduced temporal extent of Wb4 against Wb5 of 4 and 8 years, respectively, will lower the number of detected eddy profiles. However, the location of Wb4 closer to the boundary than Wb5 renders this mooring more likely to be affected by eddies identified in Fig. 4.3. In fact, any eddy created east of 73°W should in theory follow a westward track and in that case only affect Wb4. A number of 7 (11) anticyclonic (cyclonic) tracks (Fig. 4.6) are identified to travel within a distance of $1.5r$ of Wb4, which corresponds

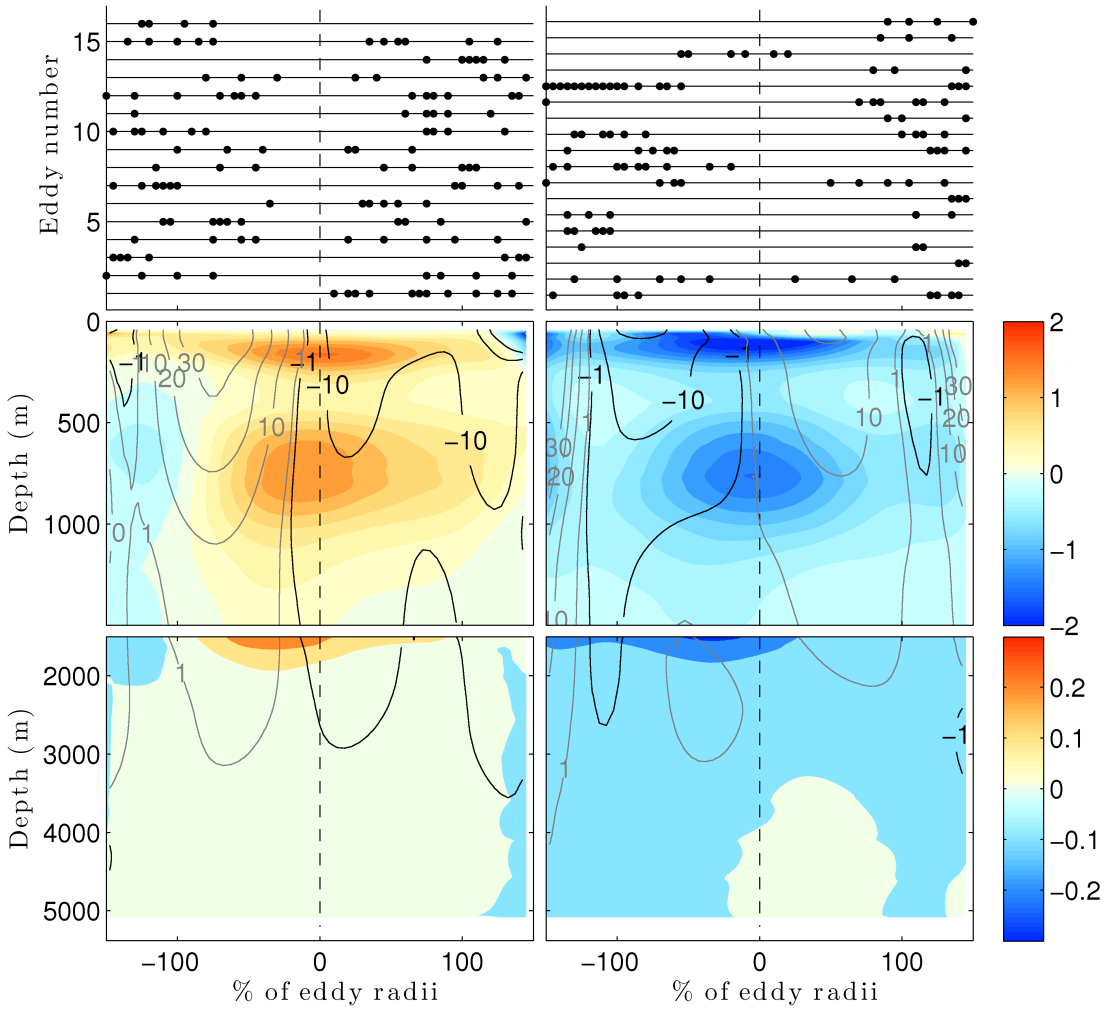

Figure 4.5: In the top panel, each line represents an eddy detected within a distance of $1.5r$ of Wb5 in the altimetry. Each eddy centre position relative to Wb5 is marked by a point. Composite potential temperature anomalies (in °C, colours) and geostrophic velocity (cm s^{-1}, lines) of anticyclone (left) and cyclone (right) at Wb5. Geostrophic velocities are referenced to the bottom. The percentage of eddy radius corresponds to the distance from the mooring to the eddy centre normalised by the instantaneuous eddy radius.

to 55 (85) θ/S profiles. The eddy composite of θ' at Wb4 is displayed in Fig. 4.6. The principal difference with Wb5 is in the eddy-core main thermocline anomaly with values up to ±3°C. The θ' vertical gradient is particularly strong below the main thermocline maximum as θ' at 2000 m (0.08°C) is not larger than at Wb5. The seasonal thermocline maximum is strongly defined for the anticyclone with a maximal value of 3.8°C. The eddy core averaged deep θ' is within 0.05°C from 2000 to 3500 m and is negative up to -0.05°C in the western and eastern sections, respectively. The eastern section of the anticyclone, which is characterised by an opposite anomaly than for the rest of the composite, may be influenced by the DWBC.

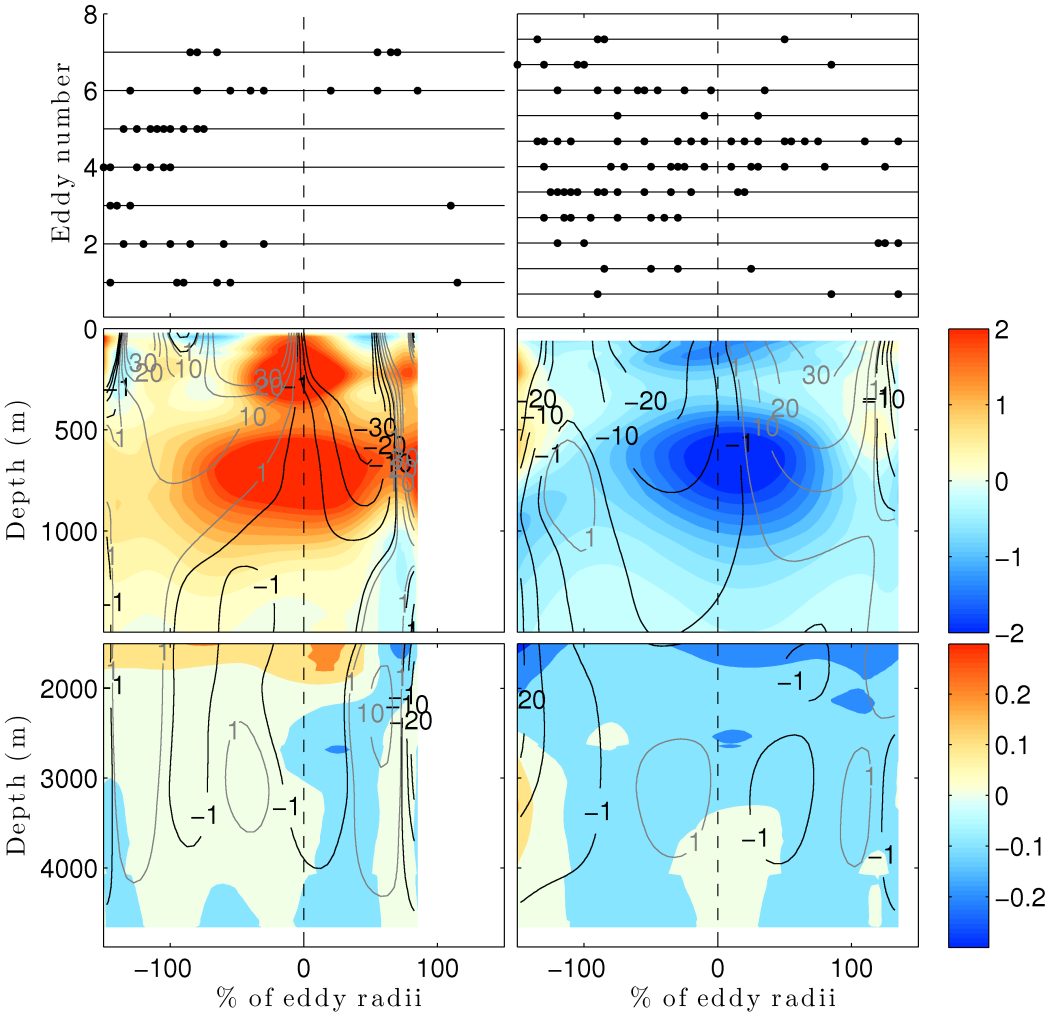

Figure 4.6: Same as Fig. 4.5 but for Wb4.

Overall temperature and salinity anomalies and geostrophic velocities at Wb4 are intensified compared to values at Wb5 in the ocean interior. The eddy intensification was observed in the elevated SSHA and DHA at the boundary (Fig. 2.3). Further work may explain this difference, which could partly arise from the shallowing topography. Eddy heat fluxes are known to be significant in the case of vertical shift of θ' as found in the North Pacific by Roemmich and Gilson (2001). Despite the presence of a similar shift in the seasonal thermocline in cyclonic conditions, no dominant eddy heat flux could be determined in the eddy composites. Out of the eddy ensemble at the western boundary, 55% are observed to cross the longitude of Wb4. The energetic eddies at Wb4 will interact with the boundary. The eddy/topography interaction is investigated in the next sections.

4.4 Eddy decay at the western boundary

In this section, an anticyclone-cyclone decay will be studied using the altimetry to have a global coverage of the western boundary (section 4.4.1). At the same time, the vertical profile of the meridional velocity at the boundary and the deep flow over the topographic rise are analysed given the eddy polarity and the mean currents (section 4.4.2). Having defined a deep flow pattern for the decay of one anticyclone-cyclone pair, this pattern is tested for the major eddies affecting the western boundary using 2 years of ADCP data (section 4.4.3).

4.4.1 An anticyclone-cyclone decay using altimetry

The evolution of one anticyclone-cyclone eddy pair as it approaches the western boundary is displayed in Fig. 4.7. This analysis provides an eddy pair description in the region essential for the understanding of the behavior of bottom velocity at Wba studied in the next two sections. Using SSHA before June 2010 (not shown), the axisymetric anticyclone is observed arriving at the boundary from the east with a purely zonal direction. The eddy is not measured at Wba before June 2010 (Fig. 4.7a). At this time, the anticyclone is no longer zonally symmetric because it is constrained on its eastern side by incoming propagating features. This constraint is observed through the meridional direction of sea surface levels associated with the enhanced zonal gradient of SSHA on the eastern side of the eddy compared to its western side. The eddy asymmetry at this stage is diagnosed from its meridional extent ($\sim$300 km) being larger than its zonal extent ($\sim$200 km). One month later (Fig. 4.7b), the maximum SSHA increased from 20 cm to 25 cm within a reduced eddy extent of $\sim$150 km diameter. Accordingly, surface geostrophic speeds are intensified in the northern and eastern eddy sections. Another month later (Fig. 4.7c), the eddy is trapped between Great Abaco and Eleuthera island at its western and southern boundaries, respectively. In September 2010, the eddy radius ($\sim$50 km) is close to the local internal deformation radius (calculated to be 47 km at Wb2 in the second chapter). Despite the disappearance of the eddy structure, its northern and western sections strenghten the incoming eddy edge through the formation of an elongated submesoscale front.

The disappearance of the anticyclone at the western boundary is followed by the appearance of a cyclone propagating from the east (Fig. 4.7d). However, this feature originates from the northeast (Fig. 4.7c), and thus does not have an entirely zonal propagation. In late September, the cyclone reaches Wba and is not axisymetric largely due to a southeast elongation. At this stage, the surface geostrophic velocities are particularly intensified and this intensification is characterised by the SSHA minimum of -30 cm. One month later (Fig. 4.7e), the eddy decay has been effective in removing some of the eddy energy and decreasing its size to a diameter of $\sim$150 km. Another month later (Fig. 4.7f) when the eddy radius is below the deformation radius, the eddy disappears leaving only a frontal reinforcement on its western side as was previously noted for the

anticyclone. Using the altimetry, the process of one anticyclone-cyclone decay does not seem to be very dependent on the eddy polarity. This is observed in the similar surface structures of both eddies in the last two months of their lifetime at the western boundary. Once an eddy arrives at the western boundary, its western edge directly interacts with the oceanic boundary whereas its eastern edge may strengthen the edge of another incoming eddy.

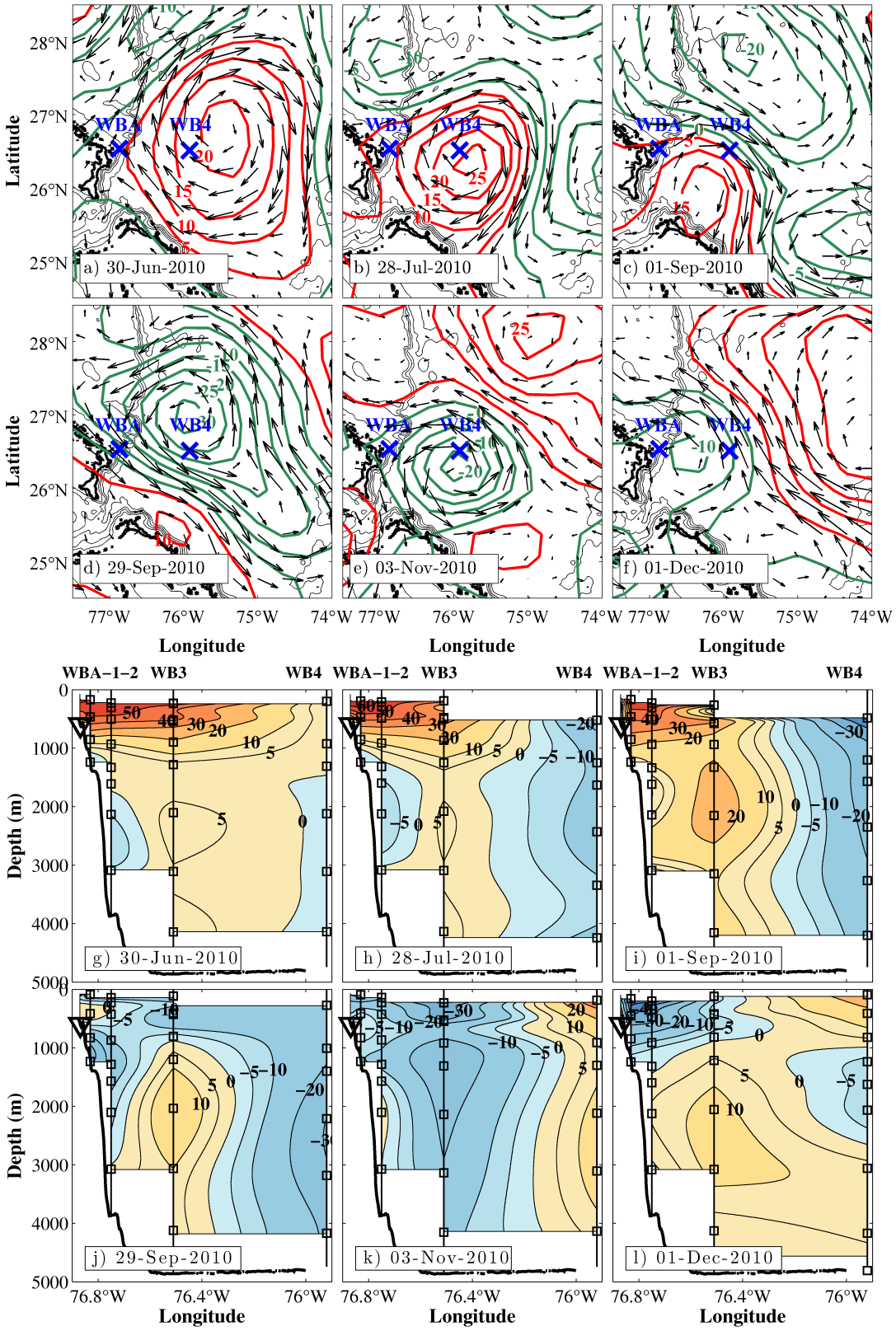

Figure 4.7: SSHA (coloured isolines) and surface geostrophic currents (arrows) during the decay at the western boundary of one anticyclone from June to September 2010 (a–c) followed by the decay of one cyclone from September to December 2010 (d–f). Great Abaco and Eleuthera islands are located in the east and south of the region, respectively. Meridional velocity of the western boundary measured by Wba, Wb1, Wb2, Wb3 and Wb4 during the anticyclone (g–i) and the cyclone (j–l). The black squares mark the positions of the current meters.

4.4.2 Transect of meridional velocity during the eddy decay

Using current meters, the subsurface eddy decay can be studied and related to its surface expression. Before studying the link between both datasets, the strong northward Antilles Current at the boundary is introduced. This current, along with the Gulf Stream which is restricted to the Florida Straits at this latitude, completes the northward transport of the subtropical gyre (Lee et al., 1996). Lee et al. (1996) estimated a mean Antilles Current of 5 $\pm$2 Sv needed to balance the southward Sverdrup circulation. They described a strong northward jet in the upper 800 m along the Bahamas with an intensification at 400 m which does not extend further than 100 km from the boundary. The mean maximum of the Antilles Current at 400 m along the coast of Abaco is estimated in Bryden et al. (2005a) to be 40 cm s^{-1} (Fig. 2.1). Despite the presence of an intensified mean jet, the Antilles Current variability is strongly affected by the presence of propagating eddies (Gunn and Watts, 1982; Lee et al., 1996) as further described in Frajka-Williams et al. (2013).

To study the velocity profile of the last two months of the anticyclone and cyclone lifetime, the mooring array from Wba to Wb4 is used. The vertical profiles of meridional velocity, interpolated in depth and longitude, are displayed in Fig. 4.7g-l. At the arrival of the anticyclone at the boundary in June (Fig. 4.7g), most of the array extending to 108 km offshore is within the surface-intensified northward leg of the anticyclone (Fig. 4.7a). The northward velocities are above 5 cm s^{-1} in the top 1000 m of the longitudinal section, and they increase when approaching Wba to values above 50 cm s^{-1} from the surface to 400 m and above 40 cm s^{-1} from 400 m to 600 m. The highest velocity at this location is expected from the location of the maximum azimuthal velocity at the edge of the eddy when represented by a Rankine vortex (Kundu et al., 2012). Moreover, the Antilles current jet also present at this location should enhance the northward/western edge of the anticyclone. At this time, the vertical structure of the eddy velocity which intensifies at the surface and decreases to the base of the thermocline corresponds to a first baroclinic mode structure, even if the deeper section below 1000 m at Wb3 does not behave accordingly with a reversed southward velocity. This is in agreement with the results of the second chapter showing that the Wb2/Wb3 deep variability is represented by higher baroclinic modes than the first mode. One month later, the center of the anticyclone is close to Wb4 (Fig. 4.7b) which now seems to be part of the southward leg of the eddy from the velocity profile (Fig. 4.7h). As expected from the decreased eddy size associated with enhanced SSHA observed in late July compared to June, the eddy strengthens with a velocity of 60 cm s^{-1} at Wba. The merger of the eastern eddy section within the front is noticed from the higher velocity gradient between Wb3 and Wb4 (30 to -20 cm s^{-1}) compared to the previous month (40 to 5 cm s^{-1}).

During the cyclone, the expected southward section of the eddy is observed in the thermocline of the array extending to Wb4 in late September (Fig. 4.7j) and between

Wba to Wb3 in December (Fig. 4.7l). However, the maximal azimuthal velocity expected at the western eddy edge is less obvious compared to the anticyclone. The northward Antilles current is believed to be responsible for the decreased velocity amplitude at Wba.

4.4.3 ADCP velocity profiles from 2010 to 2011

The aim of the present study is to test for the existence at Wba of lee waves which may be created by eddy enhanced bottom geostrophic transport over topographic features. To assess whether this process occurs close to the ADCP location (Wba), it is essential to first study the bottom velocity field, where the amplitude depends on the eddy polarity as seen in the anticyclone-cyclone example in Fig. 4.7. Using the altimetric coverage and ADCP velocities, bottom velocities are interpreted given the surface mesoscale characteristics (Fig. 4.8) from May 2010 to November 2011. The surface relative vorticity normalised by the planetary vorticity (ζ/f with $\zeta = \partial v/\partial x - \partial u/\partial y$) is computed to indicate the existence of eddies and to determine the eddy polarity at the boundary region (Fig. 4.8a). If we assume a solid-body rotation, $|\zeta/f|$ corresponds to twice the Rossby number with values between 0.05-0.1 during eddy events. The relative vorticity is calculated in the region centered at 26.6°N and 76°W close to Wb4 using surface geostrophic velocity within one degree of latitude and longitude. Under these limits ($\sim$100 km), we expect to detect the eddy polarity during their decay assuming it happens in the region close to Wb4, until they reach a 100 km diameter (Fig. 4.7c and f). At this scale the geostrophy is maintained in each eddy section. Under this scale, the eddy radius is below the internal Rossby radius and the eddy edge close to the coast may not be entirely in geostrophic balance whereas its ocean interior edge reinforces the offshore frontal region.

The presence of anticyclones and cyclones is established first from the relative vorticity at Wb4 (Fig. 4.8a) and the knowledge of SSHA in the region during ADCP measurements. Three major anticyclones lasting several weeks are observed in the boundary region around August 2010, January 2011 and September 2011. During their decay, the latitude of the eddy centre is within 1.5 and 0.5 degrees of Wb4 latitude at 26.5°N. Around June 2011, another anticyclone affects Wba for two weeks. The latitude of this eddy centre is at 29°N and so its effect on the ADCP is expected to be reduced compared to the three major anticyclones. Two major cyclones, each with a two-month lifetime at Wba, are observed around October 2010 and May 2011. The second one is directly preceded by a small cyclone lasting one month followed by a short period of negative vorticity in March 2011. Two consecutive cyclones have adjacent sections of opposite meridional transport which creates this period of negative ζ between them. In June 2011, a small cyclone transits north of the array with its southern edge around 26.5°N. Two incomplete cyclonic measurements are also present at the beginning and end of the measurement period. Overall, the three major anticyclones and two main cyclones noted thereafter A1, A2, A3, C1 and C2 (Table 4.3) are expected to strongly influence the deep transport in the vicinity of Wba based on their lifetimes and eddy

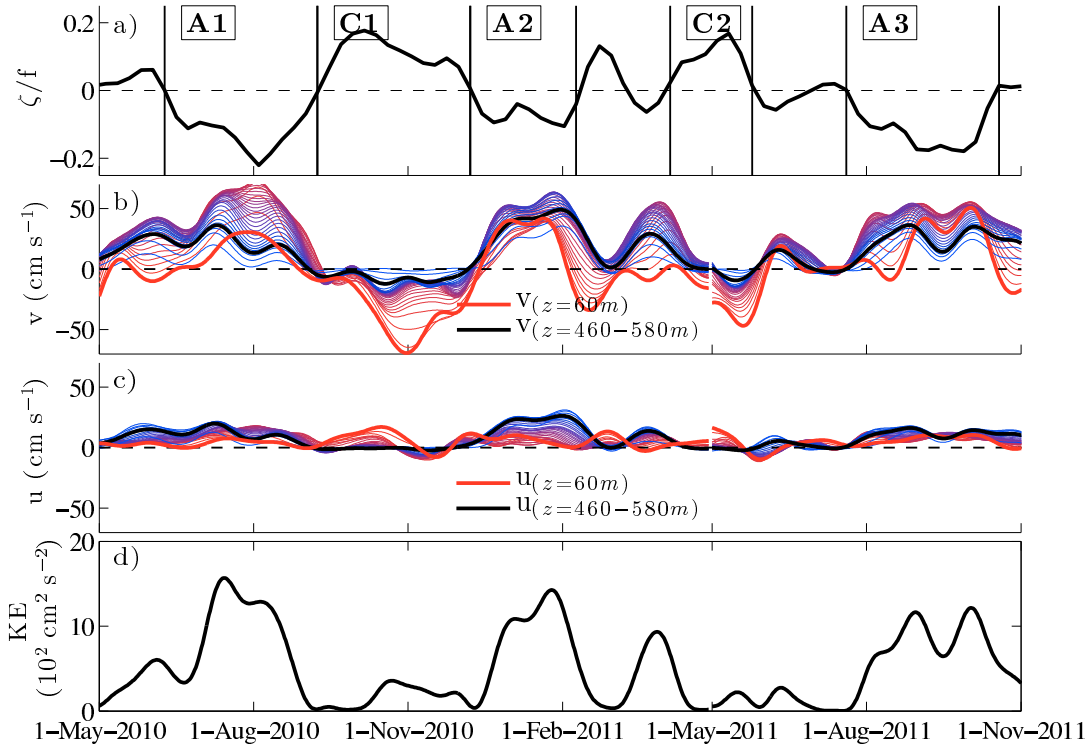

Figure 4.8: (a) Surface relative vorticity (ζ) within one degree of latitude/longitude of Wb4 normalised by the planetary vorticity. The sign of ζ delimits each main anticyclone (A1, A2 and A3) and cyclone (C1 and C2). (b) Meridional and (c) zonal velocity 30-hour low-pass filtered at Wba with varying colors representing each depth from 60 m (thick red) to 580 m (blue). The thick black line is the bottom averaged velocity from 460–580 m. (d) Depth-averaged (60–580 m) horizontal kinetic energy at Wba.

centre latitudes.

The meridional and zonal velocity profiles are studied (Fig. 4.8b and c) based on the knowledge of the surface relative vorticity. During the major anticyclones, the surface and bottom 100-m meridional velocities are relatively close as seen from their averaged values in Table 4.3. A large meridional barotropic transport is thus observed, which is particularly strong during the last two anticyclones (A2 and A3) whereas the first anticyclone (A1) contains a mid-depth velocity intensification (Fig. 4.8b). As observed from the transect sections (Fig. 4.7), the vertical coherence of the meridional velocity at Wba may be maintained by the presence of the Antilles current, which is known to intensify around 400 m. This velocity profile differs from a first-mode vertical structure which decreases from the surface. Another mechanism, which could be responsible for the acceleration of meridional velocity in the presence of anticyclones only, is based on the conservation of potential vorticity (PV). PV is defined as the ratio of the sum of the relative and planetary vorticity by the depth $(\zeta + f)/D$. Assuming an eddy propagating zonally in shallow waters, as in our case, the PV conservation requires a decreasing relative vorticity. In the case of an anticyclone with negative vorticity, this effect will

Eddy	$\bar{\zeta}/f$	$\bar{\mathrm{v}}_{(z=60m)}$	$\bar{\mathrm{v}}_{(z=460-580m)}$	Start date	End date
A1	-0.11	12.1	19.4	9th June 2010	8th September 2010
C1	0.09	-33.2	-6.0	8th September 2010	15th December 2010
A2	-0.07	27.8	38.7	15th December 2010	9th February 2011
C2	0.09	-22.3	-0.5	6th April 2011	25th May 2011
A3	-0.13	23.5	25.7	27th July 2011	12th October 2011

Table 4.3: Main anticyclones (A) and cyclones (C) observed at Wba from May 2010 to November 2011. Temporal mean during each eddy of the surface relative vorticity normalised by the planetary vorticity, the meridional velocity (cm s^{-1}) measured at 60 m and depth-averaged from 460 to 580 m. The start and end dates, which delimit each eddy, are defined from the sign of the relative vorticity measured within one degree in latitude and longitude from Wb4.

accelerate the flow while a deceleration will be associated with cyclones. The zonal deep velocity is in the range 10–25 cm s^{-1} for the three anticyclones. This is expected for the first and last anticyclones given that their centre is located slightly southward of Wb4. During the second anticyclone however, the eastward velocity is counterintuitive given its centre is at 28°N but a southwestward eddy elongation observed in SSHA may partly explain this transport.

During the two major cyclones a fully baroclinic meridional transport is observed decreasing from the surface to the bottom. In spite of the apparently similar eddy decay at the surface (Fig. 4.7a–f), cyclones and anticyclones affect the bottom meridional transport at Wba differently. A scatter plot of ζ/f versus the meridional velocity at various depths underlines the anticyclone/cyclone's distinct behaviours in Fig. 4.9. Shallow velocities are significantly correlated with the surface vorticity and this relationship is independent of the vorticity sign ($\rho = 0.56$ and 0.45 for anticyclones and cyclones respectively). However, the significance of the correlation is no longer verified for velocities at increasing depth at 460–580 m and at 580 m for cyclones. This reduction in the correlation is a consequence of the small deep current in cyclonic conditions. The skewed distribution of the deepest meridional velocity is seen in its time-average of 12.3 cm s^{-1} versus -0.9 cm s^{-1} by averaging positive or negative velocities of the lowest bin (580 m). The velocity in the deepest 100 m, referred hereafter as the deep velocity and whose amplitude is governed by the eddy polarity will be further considered as a controlling parameter along with topographic characteristics, which assume constant bottom stratification in the lee wave creation.

The significant correlation between the vorticity and shallow velocity confirms our choice of longitudinal and latitudinal limits for the vorticity construction. The temporal limits of the surface and subsurface parameters of the three main anticyclones, i.e. the ζ/f and meridional velocities zero-crossings seem to be in phase in Fig. 4.8a and b. However, the anticyclonic limit in the deep velocity lags the shallow velocity, particularly at the

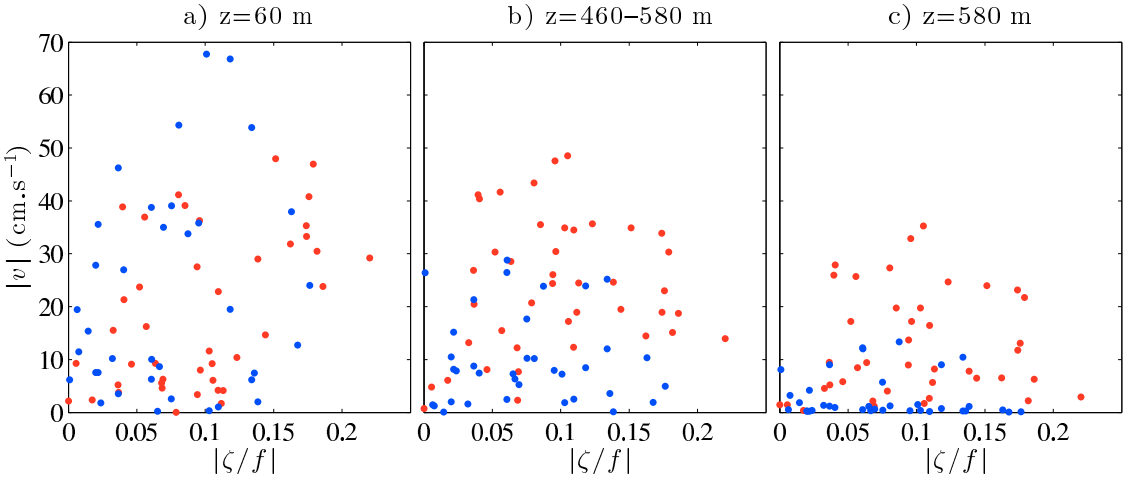

Figure 4.9: Scatter plot of weekly surface relative vorticity normalised by the planetary vorticity (ζ/f) versus meridional velocity measured by the ADCP (Wba) from May 2010 to November 2011. The anticyclones (cyclones) are displayed in red (blue) and the velocity at Wba are measured at (a) 60 m, (b) 460–580 m and at (c) 580 m.

end of the last two main anticyclones (February and October 2011).

The distinction between the enhanced anticyclonic barotropic transport and the cyclonic baroclinic transport with a reduced bottom transport is also apparent in the depth-averaged horizontal kinetic energy (KE) in Fig. 4.8. The three main peaks of KE correspond to the three major anticyclones and a smaller peak appears in the region of negative vorticity encompassed by two cyclones in March 2011. The bottom velocity, which is strongly dependent on the eddy polarity, will influence not only the frictional drag but also the internal wave field, and the focus on the second pathway is the main motivation of the present study.

4.5 Eddy-modulated internal wave activity

4.5.1 Shear variance

The shear spectra in vertical wavenumber is calculated for various deep velocity ranges and compared to the GM model representative of the open ocean in Fig. 4.10a. The buoyancy frequency normalized shear is detrended at each time step before applying a vertical wavenumber spectrum to the zonal and meridional shear. The shear spectra are temporally averaged according to deep velocity intervals. The periods for each velocity range are defined on the 30-hour low-passed meridional deep velocity (Fig. 4.8b) and applied to the 30-min shear to distinguish the mesoscale contribution from the internal wave effect. The shear spectra for low amplitude deep meridional velocity ($|v|$<8 cm s^{-1}) is in agreement with the GM model for all vertical wavenumbers. Despite the location of Wba on the continental slope away from the open ocean, internal waves present dur-

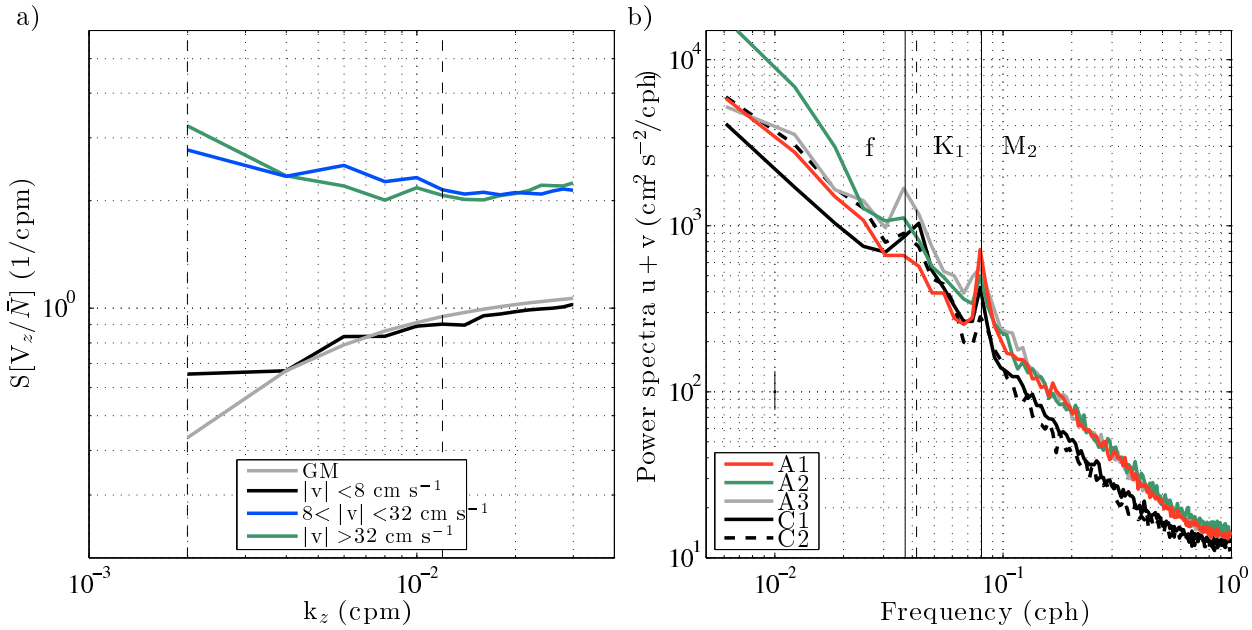

Figure 4.10: (a) Buoyancy frequency normalized mean shear spectra in vertical wavenumber for varying meridional velocity in the deepest 100 m at Wba. The shear spectra of the GM model is added in grey. The vertical dashed lines indicate the integration limits of the shear variance (83–500 m). (b) Depth-averaged (60–580 m) velocity frequency spectra (WOSA with 50% overlap) calculated for each main anticyclone (A1, A2 and A3) and cyclone (C1 and C2). The vertical black line indicates the 95% confidence interval.

ing cyclonic conditions are not significantly different from the GM prediction. Because cyclonic eddies only have a weak bottom velocity signal, the internal wave field at the boundary is not strongly influenced by cyclones. However the spectra of enhanced deep velocity ranges (8< $|v|$<32 cm s^{-1} and $|v|$>32 cm s^{-1}) are intensified at each wavenumber compared to the GM expectation. Thus we see that anticyclones strongly affect the shear spectra.

To obtain the dissipation rate (Eq. 4.3) shown in Fig. 4.11e, the shear variance is calculated by integrating the vertical wavenumber shear spectra from 83 to 500 m. Spectral corrections of vertical shear (Polzin et al., 2002), such as range-averaging and finite differencing, are not used in the present study. These corrections are normally used to correct for the attenuation of the spectra at smaller wavelengths (50 m) than our wavelength limit. The meridional velocities are also presented in Fig. 4.11b, c and d with a 30-hour low-pass, 3-10-hour and 0.8–1.3×f band-pass filters applied to characterize mesoscale, high frequency and near-inertial internal wave processes, respectively. Meridional velocities are band-passed with a fourth order Butterworth zero-phase filter used in both forward and reverse directions. The internal wave frequency distinction will help to ascertain the sources of these processes, given that no particular frequency is expected for lee waves, and near-inertial waves mostly represent wind generated waves. However, the negative vorticity associated with anticyclones, which shifts the lower in-

ternal wave frequency limit to a subinertial frequency (Kunze 1985), is responsible for wave trapping in geostrophic shear. Anticyclones may thus contribute to enhance internal wave activity through these two processes: lee wave radiation and the trapping of subinertial waves.

Enhanced internal waves, evident in the high frequency velocity and dissipation rate (Fig. 4.11c and e), are apparent for the three major anticyclones (A1, A2 and A3) associated with strong northward barotropic and deep transport (Fig. 4.11b). As observed with the reduced high frequency velocity and dissipation rate, the internal wave activity is less important during the two major cyclones (C1 and C2). The agreement of enhanced internal wave field for anticyclones confirms our observation on the shear spectra (Fig. 4.10a). The temporal variability of the dissipation rate indicates extended periods of enhanced dissipation of approximately two/three months. This timescale corresponds to the eddy period at the boundary detected in the surface relative vorticity (Fig. 4.8a).

The strength of near-inertial waves in the band-passed (0.8–1.3×f) velocity also seems enhanced during anticyclonic conditions (Fig. 4.11d) but to a lesser extent than high frequency waves. A further insight on the frequency content is provided in sections 4.6.1 and 4.6.3. In addition to the slowly varying internal wave field due to mesoscale conditions, several transient events appear in the high frequency and near-inertial velocity independent of the eddy polarity. Because these peaks are enhanced in inertial velocity, they are related to extreme wind events associated with tropical storms. Two of the largest dissipation rate peaks seen in the full depth high frequency and inertial velocity anomalies are found during cyclonic conditions: the first one lasting five days in December 2010 and the second one lasting three days in mid-May 2011. Two longer surface intensified peaks in the top 200-300 m are seen in October 2010 and September 2011 during one cyclone and anticyclone (Fig. 4.11d), respectively and will be studied in section 4.6.3.

4.5.2 Dissipation rate

The turbulent kinetic energy dissipation rate is calculated from the shear variance (Eq. 4.3). Because only the shear is available, the sensitivity of the dissipation rate to the choice of the shear-to-strain ratio (R_ω) is assessed. This ratio gives an indication of the internal wave frequency but, as first observed from Fig. 4.11 and further developed in section 4.6, the lee wave creation seems to affect the entire frequency range from high frequency to the inertial frequency. A constant shear-to-strain ratio of 3, 7 and 20 corresponding to waves with frequencies near N, GM and inertial wave fields, respectively, provide mean dissipation rates of 4.7, 2.3 and 1.2×10^{-9} W kg^{-1} and mean eddy diffusivities of 5.9, 2.9 and 1.5×10^{-5} m^2 s^{-1}.

The dissipation rate is displayed against each meridional velocity averaged in the bottom-

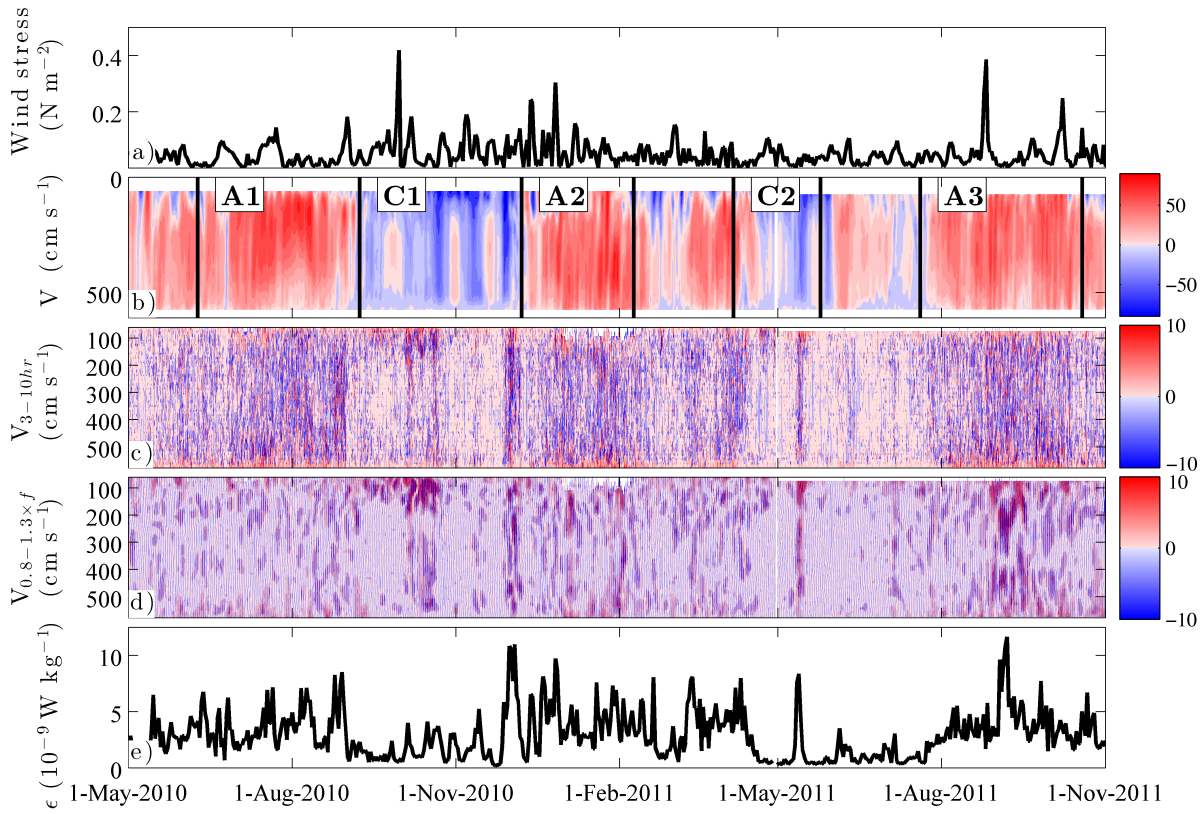

Figure 4.11: (a) Wind stress measured at Wba. Meridional velocity at Wba: (b) 30-hour low-pass filtered, (c) baroclinic velocity 3-10 hour band-pass filtered and (d) baroclinic velocity 0.8–1.3×f band-pass filtered. (e) Dissipation rate (ϵ) daily averaged at Wba.

most 100 m in Fig. 4.12. As previously done for the shear spectra, the deep meridional velocity is 30-hour low-pass filtered and the dissipation rate is daily averaged. In the weak velocity range ($|v|$<8 cm s^{-1}) corresponding mostly to cyclonic conditions (82% based on ζ/f), the average dissipation rate is relatively small (ϵ=(0.9 ± 0.6)×10^{-9} W kg^{-1}), and does not seem to be dependent on the effect of increased velocity. For bottom velocity higher than 8 cm s^{-1}, characteristic of stronger anticyclonic conditions, the dissipation rate increases with bottom velocity (ϵ=(2.8 ± 0.4)×10^{-9} W kg^{-1} for 8< $|v|$<50 cm s^{-1}). Enhanced internal wave velocities are detected in the shear variance and ϵ when the flow intensifies. The presence of waves is apparent at this velocity threshold and lasts until 32 cm s^{-1}. After this value and up to the maximal observed velocities around 50 cm s^{-1}, the minima of epsilon are smaller than those found for an eddy velocity of 25 cm s^{-1}.

The presence of internal waves or enhanced dissipation rate is found to increase for a bottom velocity accelerating from 8 to 32 cm s^{-1}. In this case, we assume that water parcels, which are located at a critical depth within few tens of meters from the crest, can travel over the topographic rise. The displacement of these water parcels can contribute to the creation of lee waves. On the other hand, water parcels located below this critical depth are blocked by the topography and may travel around the rise instead of

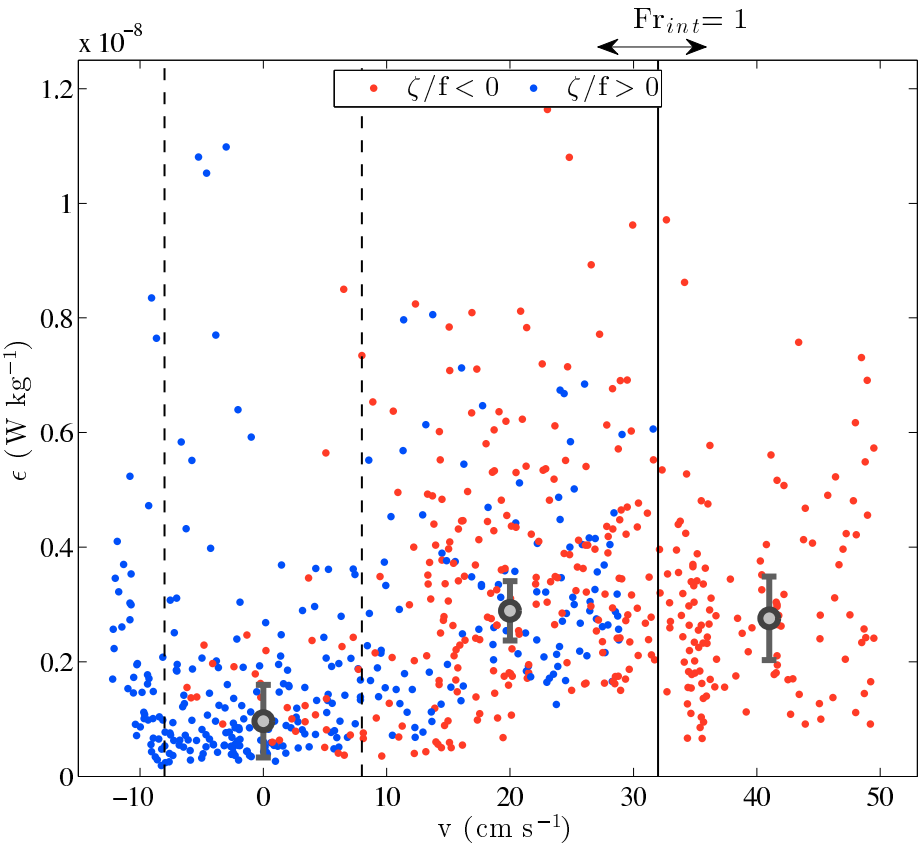

Figure 4.12: Turbulent energy dissipation rate ϵ versus meridional velocity of the deepest 100 m for anticyclones (red) and cyclones (blue). The thick gray points and lines indicate the median and standard error of the dissipation rate for each interval delimited by $|v|$= 8 cm s^{-1} (dashed lines) and 32 cm s^{-1} (solid line).

above. The regime of lee waves propagating upstream occurs as long as the lee wave phase speed is higher than the flow speed. When the reverse happens, at the criticality of the internal Froude number, the waves cannot travel upstream anymore. This may provide an interpretation for the velocity threshold (32 cm s^{-1}) above which the dissipation rate is reduced and is no longer enhanced. This could be due to the turbulent field being swept further downstream from the mooring.

The vertical wavelength ($m = 2\pi U/N$) and the range of horizontal wavelength are estimated from the linear theory. This approximation was done in the case of a large topographic Froude number by taking the velocity at the crest of the hill as measured by the ADCP instead of the upstream velocity (Klymak et al., 2010). For the lower (higher) deep velocity thresholds of 8 and 32 cm s^{-1}, the vertical wavelength is $m = 126$ m ($m = 503$ m). For the highest eddy velocity group, the horizontal wavelength ($U_0/N = 503$ m $< k^{-1} < U_0/f = 30.9$ km) becomes comparable to the topographic scale of 21.6 km. These ranges provide an estimate of the wave scales with the caveat that nonlinearities may strongly affect these scales.

4.6 Internal wave field

Both high frequency internal waves and to a lesser extent, near-inertial waves are modulated in anticyclonic conditions. The exact mechanism which produces enhanced internal wave activity is believed to be the eddy/topography interaction. For near-inertial waves however, the wave trapping expected due to the negative vorticity may also be responsible for their enhancement. First, a frequency spectrum will indicate the prevailing frequencies during anticyclonic vs cyclonic conditions. The presence of a peak at near-inertial frequencies will confirm whether the wave trapping is present. Secondly, wavenumber rotary spectra will also help to identify the wave sources by detecting the vertical direction of energy propagation. The principal mechanism proposed and investigated for the generation of internal waves at Wba is the eddy/topography interaction. However, wind forced inertial waves and internal tides are also present in the region. The interaction of eddy-generated lee waves with the tides and inertial propagations may redistribute the enhanced energy within these processes via triad interaction. This question is not the main subject of the present study and our focus is on the eddy source of internal waves.

4.6.1 Lee wave frequency range

To study the frequency content of the internal field for varying eddy conditions, the power spectra of the velocity is displayed in Fig. 4.10b. The WOSA method using a Hanning window is applied with 50% overlapping on the velocity. Spectra of 7-day blocks are time and depth averaged, thus providing a minimum degree of freedom for the five major eddies of 107 before averaging in depth. A spectrum is calculated for each major eddy of ∼2–3 month period as described in 4.4.3. The eddy limits are defined from the sign of the surface relative vorticity in Fig. 4.8a. The choice to average over the full depth will limit the distinction of surface waves against bottom generated waves but rotary spectra in the next section should address the propagation direction.

The main feature of the spectra is the significantly stronger energy in each anticyclone compared with each cyclone in the period range from 3 to 10 hours. This result confirms the previous observation on the meridional velocity band-passed on a similar range in Fig. 4.11c. The mechanism of internal wave enhancement by anticyclonic eddies seems to be especially pronounced at high frequencies. With the exception of the intensified near-inertial wave activity in the top 300 m (Fig. 4.11d) following strong winds ($\tau = 0.4$ N m^{-2}, Fig. 4.11a) from tropical storm Otto (October 2010) and Hurricane Irene (September 2011), wind stress is visibly not the main modulator of the internal wave field. A peak at M2 (12.42 hr) is observed for every eddy period but is particularly significant for the first and last anticyclones (A1 and A3). The intensity of the M2 tidal peak of the anticyclone A1 compared to the cyclone C1, or their M2 difference compared to their difference at 10 hr, may indicate that a portion of the enhanced eddy

energy is contributing to the M2 peak. Closer to the inertial peak, this anticyclone A1 is less intense than the other eddies which are intensified independently of their polarity. However given the 1-hour Nyquist period, the peak at 26.8 hr is not fully distinguishable from the K1 tidal peak at 23.9 hr, which prevails for the first cyclone (C1). Some aliasing may be present which does not render the identification of the f and K1 peaks straightforward at our latitude.

The frequency spectra confirm the results of filtered velocity timeseries with enhanced high frequency (3–10 hr) signal during anticyclonic conditions. At lower frequencies, however, the eddy/deep velocity effect on the internal wave field is less clearly identified due to the presence in the region of tidal and wind generated inertial waves. In theory, near-inertial waves may be trapped in anticyclones. The near-inertial peak during the anticyclones is not strongly different than the near-inertial peak of cyclones which is also aliased with the K1 peak. Overall, the higher energy of the anticyclone may shift the peak but should not make it significantly different than the cyclonic near-inertial peak. Also, the absence of a near-inertial peak for the anticyclone A1 renders an excitation of waves by flow/topography interaction at this frequency less predictable than at higher frequencies. This makes the observation of enhanced near-inertial waves from Fig. 4.11d during anticyclones hard to confirm. The presence of inertial waves could stem from another source other than the eddy which would then be intensified with anticyclonic properties. This may explain the strong near-inertial waves in the last anticyclone A3, which may be intensified at the surface. A rotary spectra may help to identify the direction of wave propagations and to hypothesize on their sources assuming that we observe directly the waves after their excitation but not after reflection.

4.6.2 Direction of energy propagation using wavenumber rotary spectra

To confirm the generation of internal waves from the interaction of the deep velocity with the toppgraphy, the detection of the energy propagation direction is necessary. The rotary spectra may provide the required information. The rotary spectra can be calculated during cyclonic and anticyclonic eddies to separate the clockwise and counterclockwise rotating components of the horizontal velocity vector timeseries as in Leaman and Sanford (1975). Rotary wavenumber spectra (Gonella 1972) are calculated using the knowledge of shear spectra and their quadrature spectra (defined as the imaginary part of the cross-spectrum). Using this methodology, the anticlockwise and clockwise spectrum are composed of both autospectra plus or minus the quadrature spectra, respectively. The sense of rotation of the shear vector or the polarization around the wavevector is directly related to the directions of the phase and energy propagation (Leaman and Sanford, 1975). Looking downward, a clockwise ellipse is associated with upward phase and downward energy propagation in the northern hemisphere. A counterclockwise ellipse characterizes a downward phase and upward energy propagation. The rotary spectrum is calculated on the detrended buoyancy frequency normalised

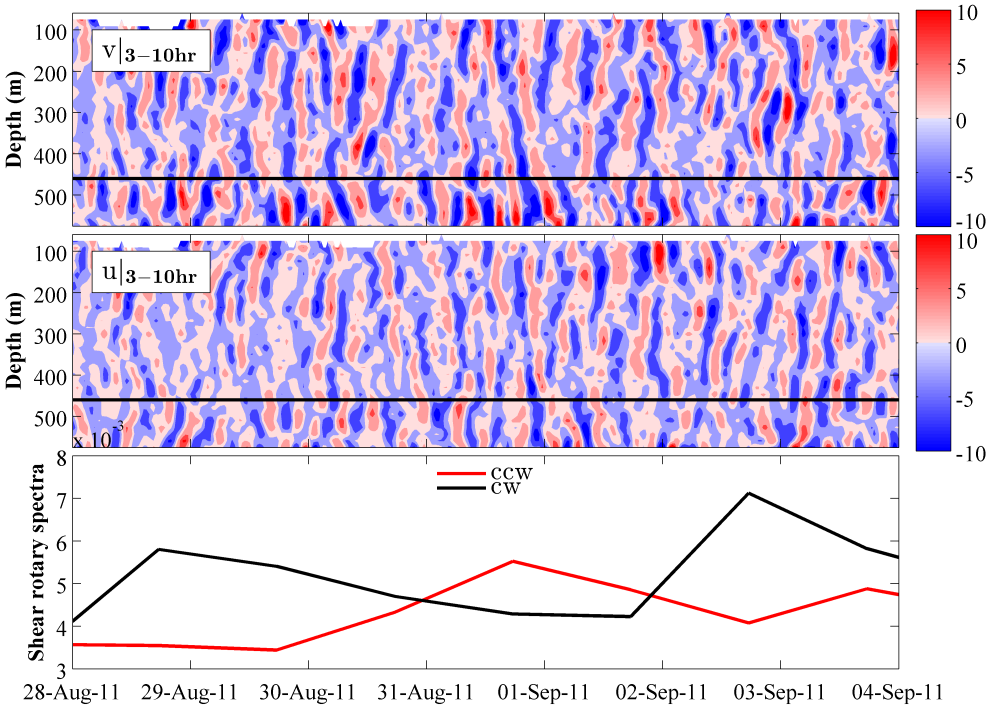

Figure 4.13: Meridional (top) and zonal (middle) baroclinic 3–10 hours filtered velocity during enhanced northward flow anticyclonic conditions at Wba from 28th August to 4th September 2011. Rotary wavenumber spectra of the buoyancy frequency normalised shear measured in the deepest 100 m and integrated over the vertical wavenumber (bottom). The anticlockwise and clockwise daily averaged are displayed in red and black respectively.

shear at each 30-minute interval. A daily average is then calculated. To focus on waves of various frequency, the spectra is computed on high frequency and inertially-filtered shear.

Before analysing rotary spectra over the full ADCP period, meridional and zonal high frequency filtered velocities are displayed along with their rotary spectra for a strong anticyclonic event around August 2011 in Fig. 4.13. Internal waves are observed across the full depth in the period 3–10 hours with stronger amplitudes for the meridional than for zonal velocity. Looking at the meridional velocity, waves of downward phase propagation or upward energy propagation are found during almost the entire period in the deepest 200 m. These waves are particularly well-defined for v below 400 m for the 31st of August and the downward phase propagation is observed over the entire column in the last 12 hours of the 31st. Despite this well defined event, the wave crests above 400–500 m for the rest of the period are almost vertical, and they can also have opposite phase propagation, for example in the top 300 m for the 1st of September. The enhanced anticyclonic northward flow is believed to affect the high frequency internal wave phase propagation.

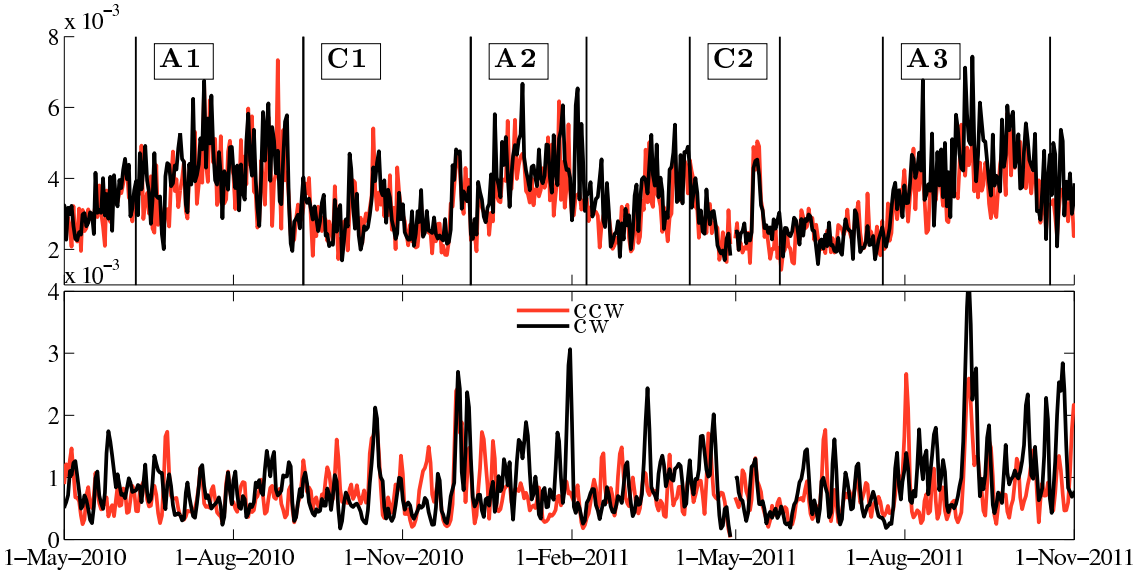

Figure 4.14: Rotary spectra of the buoyancy frequency normalised shear measured in the deepest 100 m for the high frequency (top) and inertial frequency (bottom) filtered baroclinic velocities and integrated over the vertical wavenumber. The anticlockwise and clockwise daily averaged are displayed in red and black respectively.

The daily rotary spectra integrated over the vertical wave number are also displayed for the same strong anticyclonic period in Fig. 4.13. As expected from the observations on the velocity fields, the counterclockwise spectrum prevails during the period around the 31st of August to the 2nd of September whereas the clockwise spectrum is more energetic for the rest of the period. The rotary spectra confirms the difficulty of clearly identifying the upward propagating energy. The choice of the depth range over which the shear rotary spectra is calculated is an essential parameter in the identification of upward propagating energy. The most significant difference of the anticlockwise/clockwise spectra around the 31st of August is found in the bottommost 100 m as displayed in Fig. 4.13. The dominance of counterclockwise over clockwise energy still persists if the spectra are calculated over the bottommost 200 m but the difference is less significant than for 100 m. Around 300 m both directions are equally represented so the rotary spectra is strongly sensitive to the depth range.

Because upward propagating waves from the seafloor seem to be well identified during the anticyclonic event in Fig. 4.13 for the bottommost 100 m, the rotary spectra are calculated in the same depth range for high frequency and inertial filtered shear over the extended period in Fig. 4.14. The first observation when comparing the high frequency and inertial rotary spectra shows that the three anticyclones A1, A2 and A3 have more energy in the high frequency spectra than in the near-inertial spectra. This confirms the results of the frequency spectra of each eddy in Fig. 4.10b. Despite the anticyclonic effect on the rotary spectra, the larger counterclockwise spectra over clockwise spectra for the anticyclone is not evident as expected from the remarks on Fig. 4.13. This may

be because the presence of a strong mean current across the full water column during anticyclonic conditions will not only affect the Doppler-shifted frequency but may influence the wave propagation and so interfere with the rotary spectra results. For example, a high frequency wave which propagates against a vertical sheared flow, as hypothesised in our anticyclonic case, will have its phase lines vertically-shifted (Baines 1995). The phase line shift may hinder a clear distinction of high frequency upward propagating lee waves with downward propagating waves.

The critical layer, where the vertical wavenumber is zero and at which a wave of opposite direction is reflected, satisfies $(\omega - U(z)k)^2 = N^2$. The N peak can also introduce a critical layer. The reflected wave, as well as surface reflected waves, will blur the rotary signal. The rough estimate of horizontal wavelength, calculated in 4.5.2, prevents us from clearly identifying a critical depth. In addition, waves may not propagate in the strongest flow which also satisfies a supercritical Froude number as mentioned in 4.3.2. Similarly, no over representation of counterclockwise or clockwise waves at the inertial frequency is visible during anticyclones. In addition, downward propagating energy of wind induced near-inertial waves may also oppose inertial lee waves. The propagation of near-inertial waves, known to be sensitive to the eddy polarity, is addressed in the next section by considering the additional wind effect.

4.6.3 Inertial waves in anticyclonic conditions

The presence of enhanced high-frequency internal waves during anticyclonic conditions was first observed in the filtered baroclinic velocity in Fig. 4.11c and then confirmed from the frequency spectra of each anticyclone (Fig. 4.10b). The link between the anticyclonic flow/topography interaction seems particularly strong for internal waves in the highest frequency range. For near-inertial waves, however, even if the presence of strong waves seems related to anticyclonic conditions in Fig. 4.11d, there is no clear difference of spectral energy for different eddy polarities in Fig. 4.10b. In order to determine the proportion of near-inertial waves which could be identified as lee waves, it is useful to associate wind-induced near-inertial waves with downward propagating energy. In addition to anticyclonic lee waves, anticyclones are believed to enhance the wave field through the near-inertial wave trapping due to the presence of background negative relative vorticity as described in Kunze (1985). From the frequency spectra averaged over each anticyclone (Fig. 4.10b), no shift in the inertial frequency was observed as would have been expected if the background anticyclone field was influencing the wave field. The wave trapping does not seem to occur on the eddy time scale. However, the inertial rotary spectra contains high peaks of shorter scales than eddy timescales (Fig. 4.14) which may in part be induced by wind anomalies. Despite the absence of the inertial frequency shift over mesoscale timescales, the wave trapping may still exist for the wind induced waves. This section will thus investigate whether anticyclones may also contribute to the internal wave field through the shear flow/wave interaction in addition to

the lee wave creation.

Kunze (1985) used a wave mean flow interaction model to explain the observed link between the high energy intermittent near-inertial peak and the low frequency mesoscale flow. Assuming a comparable horizontal lengthscale for the waves and the mean flow, the author included in the equations of motion the nonlinear terms of both the wave shear and the mean flow shear. The internal wave dispersion relation of the Doppler shifted intrinsic frequency becomes dependent on the effective frequency ($f_{\text{eff}} = f + \zeta/2$), which adjusts the effect of the planetary vorticity by the eddy background relative vorticity (ζ). In the present case, we focus on the effect of the horizontal shear assuming a barotropic flow. This assumption is confirmed by the anticyclonic flow at Wba which contains a strong barotropic component when the Antilles current intensifies the bottom flow as seen in Fig. 4.8. The reduced effective frequency compared to the inertial frequency in anticyclonic conditions extends the frequency range of internal waves. If a wave is created in the range f_{eff} to f, it will be trapped in the eddy and cannot enter the region of higher inertial frequency outside the eddy. From Fig. 4.10b, it was concluded that lee waves are not created in this extended frequency range. Considering that wind-induced waves will propagate from the surface instead of from the bottom as for lee waves, these waves will approach the mean shear from a different angle. A ray tracing method may help to define the exact path of these waves but this is beyond the scope of the present study. Before testing if subinertial waves exist in addition to lee waves during anticyclonic conditions, we first need to identify wind anomalies above the anticyclonic decay region whose maximum extent was roughly approximated to be 300 km diameter asymmetric vortex in Fig. 4.7.

The western North Atlantic region is strongly affected by storms and their associated amplified wind stress events. Storm induced inertial waves are studied in D'Asaro et al. (1995) and presented in the North Atlantic midlatitudes in Jaimes and Shay (2010). The subsequent effect of wind-generated waves, propagating in the ocean interior, on vertical mixing can be evaluated (Cuypers et al., 2013). If storms are not strongly affected by oceanic mesoscale processes, wind induced near-inertial waves can be present whatever the eddy polarity. This seems to be true for the large events of near-inertial waves in Fig. 4.11d which happens during the cyclone C1 and anticyclone A3 in October 2010 and September 2011. A closer look at the inertial velocity profiles confirms the downward propagation of energy during these two periods. These two events are related to the passage of two storms in the vicinity of the Bahamas. The centre of the tropical storm Otto is located at 23.6°N and 68.3°W with wind speeds of 83 km h^{-1} on the 7th of October 2010 before becoming a hurricane and traveling to the northeast (Cangialosi, 2010). From the 22nd to 26th of August 2011, Hurricane Irene was observed around the Bahamas, and on the 26th was centred at 30°N and 77.4°W with wind speeds of 157 km h^{-1} before moving towards the US coast (Avila and Cangialosi, 2011). The effect of these two storms on the wind stress at Wba is visualised in Fig. 4.11a. Two periods of

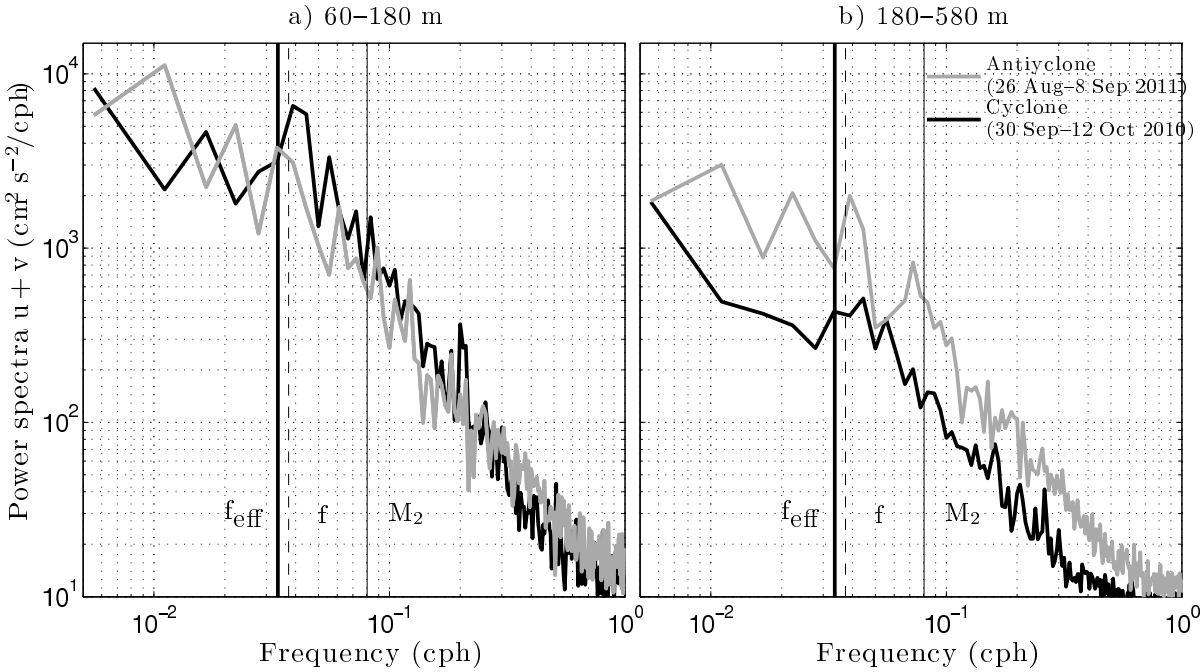

Figure 4.15: Depth averaged from 60–180 m (left) and from 180–580 m (right) meridional and zonal velocity spectra in frequency calculated during one cyclone (black) and anticyclone (grey). The periods are chosen after the passage of a storm. The inertial (dashed) and M2 (thin line) frequency are plotted for both depth range and f_{eff} (thick line) is added for the shallow depth range (left).

two weeks are chosen following the passage of the storms to study near-inertial waves. The first period, from 30th September to 12th October 2010, in the cyclone C1 starts few days before the passage of Hurricane Otto, which is preceded by a strong wind anomaly around Wba on the 30th September 2010. The second period, 26th August to 8th September 2011, during the anticyclone A3 starts after the passage of Hurricane Irene. Due to the location of these storms in the vicinity of Wba, their effect is seen at Wba in Fig. 4.11d.

Having detected two periods of strong wind stress during one cyclone and anticyclone, the effect of the background shear on the near-inertial wave is tested in Fig. 4.15. Frequency spectra are calculated on velocity profiles and averaged for a shallow (60–180 m) and deep (180–580 m) range. The velocity spectra are computed for the two 2-week periods in Fig. 4.15. During the cyclone C1, the inertial peak is located at the frequency f. For the anticyclone A3 however, the inertial frequency is shifted from the f frequency toward a lower frequency in the shallow range. By taking a surface vorticity of -0.2 as observed during the anticyclones in Fig. 4.8, the effective frequency ($0.9 \times f$) is displayed in the spectra. This effective frequency corresponds to the observed lower frequency peak observed in the shallow region. Wind induced inertial waves propagating from the surface thus seem to be shifted in frequency by the anticyclonic field at Wba. This process, in addition to the creation of lee waves over the topographic rise at Wba is also

expected to be responsible for the enhanced wave activity and subsequently to intensify the mixing during anticyclones. The anticyclonic lee wave activity is also observed in the power spectra of the deep section (Fig. 4.15b) compared to the cyclonic conditions for frequency higher than M2.

4.7 Discussion

The mean eddy diffusivity behaviour is comparable to the dissipation rate if we assume a constant stratification. For weak deep velocity ($|v|$<8 cm s^{-1}), the median eddy diffusivity is $(1.2 \pm 0.8)\times10^{-5}$ m^2 s^{-1} whereas for stronger velocity ($|v|$>8 cm s^{-1}), characterising mostly the anticyclonic behaviour, the diffusivity is $(3.5 \pm 0.5)\times10^{-5}$ m^2 s^{-1}. The diffusivity is affected by the presence of strong deep northward anticyclonic flow, which may be enhanced by the Antilles current. Our estimation can be compared to K_ρ=10^{-4} m^2 s^{-1} which was the first estimation of Munk (1966) from the 1D vertical advective diffusive balance required to balance the 25 Sv of deep water formation. Increased deep diffusivity values were also observed at the boundaries in the Brazil Basin (Polzin et al., 1997) and in the Southern Ocean (Naveira-Garabato et al., 2004). Using microstructure data and a tracer release, Polzin et al. (1997) found enhanced diapycnal mixing over rough topography (5×10^{-4} m^2 s^{-1}) versus smooth topography (0.1×10^{-4} m^2 s^{-1}). This enhancement was subsequently attributed to the interaction of barotropic tides with the topography. This process is more efficient over the rough topography of the Mid-Atlantic Ridge than in the eastern side of the basin. Enhanced mixing rates were also observed over the rough topography of the Southern Ocean (Naveira-Garabato et al. 2004) but the strength of eddy flow versus tidal flow led the authors to conclude that topography/mesoscale interaction may primarily modulate the mixing level. Despite the large difference of eddy diffusivity attributed mostly to our shallower study with higher stratification, the western boundaries of the ocean seem to play a significant role in the removal of eddy energy to smaller scale internal waves. In the present study we confirm the modulation of internal waves by anticyclones. A strong argument for the eddy energy destruction at the western boundary and the associated enhanced mixing comes from the westward propagating direction of eddies in the absence of strong currents such as the Gulf Stream. In addition to the mixing value found at Wba, the presence of strong northward flow between 500–1500 m (Fig. 4.7) should also interact with the topographic features around 1500–2000 m observed north of the array (Fig. 4.1).

The enhanced anticyclonic diffusivity (3.5×10^{-5} m^2 s^{-1}) can be compared to values from previous studies in the North Atlantic western boundary which analysed the effect of varying DWBC flow (Stöber et al., 2008; Köhler et al., 2014) instead of varying eddy conditions. These studies used six cruises with CTD and LADCP profiles across the boundary at 16°N from 2000 to 2005. Stöber et al. (2008) separated DWBC dominated regimes with enhanced bottom meridional velocity (v>35 cm s^{-1}) and diffusivity up to

3×10^{-3} m^2 s^{-1} on the continental slope below 1000 m from eddy northward flow regimes with lower diffusivity (K_ρ <3×10^{-4} m^2 s^{-1}). Despite the lower values of diffusivity found in our study, due in part to the large stratification in the upper 600 m, we have found that the western boundary diapycnal mixing is not only modulated by the DWBC but also by eddies. The direct effect of eddy-induced internal waves on the mixing was further considered in the Southern Ocean and over the MAR. Liang and Thurnherr (2012) were able to find a link between eddy flow and internal waves from the subinertial and finescale kinetic energy near a crest of the East Pacific Rise. Other studies also linked the turbulent dissipation with eddy activity by focusing in regions of enhanced eddy kinetic energy such as the Drake Passage (Brearley et al., 2013). Large dissipation rates were also associated with strong currents over rough topography in the energetic Antarctic Circumpolar Current (Sheen et al, 2013; Waterman et al., 2013).

4.8 Conclusions

The present chapter investigates the link of the internal wave field with mesoscale eddies when these eddies impinge on the western boundary of the North Atlantic. The following points summarise the main findings of the chapter.

- In the North Atlantic midlatitudes, eddies are observed travelling zonally towards the western boundary in altimetric data. Out of the eddy ensemble at the western boundary, 55% are observed to cross the longitude of Wb4. The energetic eddies at Wb4 interact with the boundary.

- In anticyclonic conditions, enhanced bottom velocities of an ADCP located at 13 km from the coast in 600 m deep water are observed. This enhanced northward deep flow modulates the internal wave field over a 1500 m high and 21 km wide topographic rise.

- The internal wave activity seems to increase for a bottom velocity accelerating from 8 to 32 cm s^{-1}. The upper limit of the range (32 cm s^{-1}) may be related to the criticality of the internal Froude number.

- Using a finescale parameterisation, an intensified diffusivity of 3.5×10^{-5} m^2 s^{-1} is characteristic of anticyclonic conditions compared with a background level of 1.2×10^{-5} m^2 s^{-1}.

- Internal waves were observed to be amplified particularly in the 3–10 hour period.

- Rotary spectra support energy propagating upward from the bottom for short events, which is consistent with high frequency lee waves. However, this observation could not be generalised to all anticyclonic periods. A phase line shift by the intense eddy mean flow may interfer with the rotary spectra.

Current profiler and altimetric observations at the western boundary of 26.5°N provide convincing evidence that the internal wave field is modulated by the mesoscale eddy field. In particular, anticyclones with large bottom flow at the boundary are associated with elevated shear variance and dissipation, relative to cyclones. Further study in the region may define the prevailing mechanism of internal wave generation: lee waves over small or steep topography, Kelvin wave hydraulic control or another mechanism of wave creation. A study of the internal wave propagation, whether or not hydraulically controlled, may establish the eddy-induced effect on the local hydrography and tracer concentrations as well as the effect on the deep mixing and circulation at the western boundary.

Chapter 5

Conclusion

The present study has addressed two problems related to westward propagating features in the North Atlantic. First the effect of eddies and Rossby waves on the upper mid-ocean transport was estimated using 7 years of data from the RAPID array associated with altimetric data. Having observed that eddies propagate to the western boundary, it became relevant to study the decay of these processes. To do so the modulation of internal waves over a topographic feature was investigated by analysing ADCP and altimetric data. The present chapter summarises the main results and suggests possible future work.

5.1 The effect of eddies and Rossby waves on the MOC

The effect of eddies and Rossby waves on the meridional overturning circulation measured at 26.5°N with the RAPID array was first addressed. In the future, a precise estimation of this effect may allow us to distinguish the inherent variability of the MOC attributed to westward propagating processes generated at midlatitudes from potential long-term changes such as variations in the rate of deep water formation at high latitudes. To quantify the contribution of westward propagating signals on the geostrophic and transbasin transports of the MOC, eddies and Rossby waves were detected in data from altimetry and full-depth moorings. Their frequency and zonal wavelength were characterised as well as their vertical structure in terms of baroclinic modes. Given their tendency to propagate westward, it was possible to observe them as they travelled across 26.5°N in the Atlantic.

In order to characterise westward propagating anomalies, their presence was first confirmed over the entire basin in the latitudinal band from 20 to 30°N. The magnitude and direction of propagating anomalies was defined from lagged cross-correlations of SSHA. In the absence of strong mean flow, such as the North Brazil Current or the Gulf Stream which is confined to the Florida Straits, these anomalies are observed to reach the western boundary at midlatitudes around the RAPID array. The link between surface anomalies and isopycnal displacements was then investigated using the three moorings Wb2, Wb3 and Wb5 located at 20, 49 and 500 km offshore of the western boundary,

respectively. The correlation of isopycnal displacements with SSHA is significant in the top 4500 m at Wb5. At the Wb2 mooring, isopycnal displacements are significantly correlated with SSHA in the top 1200 m. A decomposition in baroclinic modes of isopycnal displacements was performed and supported by a WKBJ analysis at each mooring to detect the most representative vertical structure of westward propagating anomalies. These results were consistent with the evolution of the correlation of isopycnal displacements with SSHA as the boundary is approached. The percentage of variance explained of available potential energy by the first baroclinic mode was found to reduce from 52% to 15% when moving from Wb5 to Wb2. Meanwhile, the variance explained of the third mode increased from 10 to 17%. Despite the decreased importance of mode 1 at the boundary, a common period of maximum variability is found above 80 days with a maximum at 180 days in all moorings. Based on the identification of the vertical structure of westward propagating features, the period associated with these features (80–200 days) was confirmed using their SSHA signature. From coherence spectra, the phase speed of these features described by the first baroclinic mode was observed to be faster 500 km off the western boundary (7.3 cm s^{-1}) than the phase speed over the entire North Atlantic (4.6–5.1 cm s^{-1}) calculated from a 2D frequency-zonal wavenumber SSHA spectra. At the boundary between Wb2 and Wb3 however, the phase speed declined to 4 cm s^{-1}.

By considering isopycnal displacements only related to a first baroclinic mode structure at Wb2, it became possible to assess the role of eddies and Rossby waves on the internal and upper mid-ocean transports. Density anomalies attributed to the first mode were reconstructed and used at the western boundary of the geostrophic calculation. A correlation of 0.77 was found between the geostrophic transport attributed to mode 1 and the observed geostrophic transport. As expected from the structure of propagating anomalies at Wb2, this correlation was significant only in the top 1100 m. On interannual timescales, the correlation between the observed transports and those attributable to mode 1 was not significant. Eddies and Rossby waves are thus not expected to directly affect the geostrophic transport on interannual timescales. This observation should help to differentiate the effect of eddies and Rossby waves on the variability of the MOC from other processes characterised by longer timescales. The correlation of 0.77 is reduced to 0.65 when considering the upper mid-ocean transport, which also includes the wedge and the compensating barotropic transports. Given the relationship between SSHA and mode-1 structure/geostrophic transports, we can attempt to evaluate the meridional coherence of the subannual geostrophic transport using SSHA. The correlation between SSHA at 26.5°N along the 3900 m isobath is below significance within three degrees north or south. Transport anomalies are not expected to be coherent for meridional scales greater than 600 km. The standard deviation of the upper mid-ocean transport attributed to the first mode is 2.6 Sv, which gives an estimation of the variability associated with eddies and Rossby waves at periods of 80–250 days.

5.2 Generation of internal waves by eddies impinging on the western boundary of the North Atlantic

In the fourth chapter, eddies were analysed at the western boundary to find whether they can modulate the internal wave field over topographic features during their decay. The focus was on the internal wave activity over a topographic rise using an upward looking ADCP (Wba) located on this rise in 600 m deep water 13 km offshore. The topographic rise, which is 1500 m high and 21.6 km wide in the meridional direction, is adjacent to the continental slope. Using an eddy tracking product, it became possible to identify eddies propagating towards the western boundary. Out of all the eddies travelling within one degree of latitude and longitude from Wb4 and Wb5, located at 100 and 500 km offshore respectively, 55% are observed to cross the longitude of Wb4 and may interact with the boundary. The decay of an anticyclone-cyclone pair was analysed using the altimetry and a section of current meters extending from Wba to Wb4. The decline of an anticyclone-cyclone pair did not reveal any dependence in SSHA or in the surface relative vorticity to the eddy polarity. The meridional velocity however, was only enhanced for anticyclones with a large barotropic component and bottom values reaching up to 50 cm s^{-1} at Wba. In contrast, cyclones are more baroclinic with a surface intensified flow. The dependence of the bottom velocity to the eddy polarity was also noticed during the two years of ADCP data, which detected 3 major anticyclones and 2 major cyclones measured for about 2–3 months at Wba. The presence of the Antilles Current, located at the boundary with its centre at 400 m, may account for the bottom velocity behaviour.

Given the relationship of the deep velocity with the eddy polarity, the presence of internal waves was investigated for varying bottom velocities. The shear spectra also demonstrates a dependence to the eddy polarity with enhanced variability for anticyclonic conditions and a spectra closer to the GM model for bottom velocities associated with cyclonic conditions. Using a finescale parameterisation, the dissipation rate of turbulent kinetic energy was estimated from the integrated shear spectra. The dissipation rate is found to be dependent on the bottom velocity at Wba. A median dissipation rate of 2.8×10^{-9} W kg^{-1} is measured for strong velocity ($8< |v|<50$ cm s^{-1}), whereas the dissipation rate reduces to 0.9×10^{-9} W kg^{-1} for weak bottom velocity ($|v|<8$ cm s^{-1}). A decline in the dissipation rate minima is found around 32 cm s^{-1}. This decline may result from the enhanced bottom velocity, which prevents waves from propagating upstream at the criticality of the internal Froude number. The intensification of the internal wave activity during anticyclonic conditions is particularly significant in the period range from 3–10 hours but is not as significant for the f and M2 peaks. While for some events, the integrated rotary spectra suggest that near the bottom, high frequency internal waves are upward propagating, the results were not consistent in anticyclonic periods. The strength of the anticyclonic barotropic flow and the presence of near-inertial waves may hinder the rotary spectra. In addition to the enhanced activity of lee waves during anti-

cyclones, the background negative vorticity of anticyclones lowers the inertial frequency of internal waves and allows a larger frequency range of near-inertial waves subsequent to the passage of a storm.

5.3 Further work

The identification of the effect of eddies and Rossby waves on the upper mid-ocean transport may enhance in the future the detection of any other process which may affect the MOC. In this regard, the influence of westward propagating features was detected in a period range of 80–250 days. The effect of these anomalies on the standard deviation of the upper mid-ocean transport was estimated to be 2.6 Sv. It becomes possible for example to ascertain whether or not propagating features are responsible for any observed anomaly or trend in the calculation of the geostrophic transport. The 30% MOC decline observed in McCarthy et al (2012) from early 2009 to mid-2010 was observed in the strengthening of the southward thermocline transport associated with a decreasing southward LNADW. The temporal scale and vertical structure of this anomaly are not comparable to the period range associated with eddies and Rossby waves at the western boundary or to their vertical structure. The present findings may also be useful to compare the role of westward propagating features on the meridional circulation in global circulation models, which are improving from eddy-permitting to eddy-resolving. This could make easier the detection of the influence of other processes than westward propagating features on the circulation at midlatitudes.

The extent of the measurements by the RAPID array will allow in the future to analyse the stability of the field of eddies and Rossby waves. Over seven years of observations it can be difficult to identify any trend in the properties of eddies and Rossby waves. In the hypothesis of a changing climate associated with a high probability of extreme events, the eddy frequency and amplitude might also be affected. This could result in a period with a standard deviation of the upper mid-ocean transport attributed to westward propagating features larger than the 2.6 Sv presently found.

Having detected the most representative structure of westward propagating features, it may be worthwhile in the future to investigate meridional propagating features such as boundary trapped waves in the region around Wb2. A first comparison could be done theoretically using the dispersion relation. In the presence of moorings located in the meridional direction around Wb2, it should be possible to detect boundary propagating features, to distinguish them from the signals with an eastward origin, and to finally quantify their influence on the upper mid-ocean transport. These meridional processes may be responsible for the deep energy found in higher baroclinic modes than the first mode at Wb2 and Wb3 within a distance of one Rossby radius from the boundary.

The enhanced activity of internal waves and the associated elevated dissipation rate during anticyclonic conditions should help to improve the understanding and the parameterisation of eddy dissipation at the western boundary, where eddies are particularly intensified. The interaction with the wave field is one pathway of eddy dissipation and other mechanisms should also be considered to fully describe the eddy dissipation. The bottom drag with its dependence to the velocity squared is expected to be also amplified during anticyclonic conditions. By determining the exact area where the dissipation rate is enhanced at the boundary, the decay rate of KE could be compared to the dissipation rate for anticyclonic and cyclonic conditions. The KE can be approximated from the integral in cylindrical coordinates of the KE in the section from Wba to Wb4 in the top 1000 m. The enhanced anticyclonic dissipation rate is expected to remove more energy than for the cyclones. The decay timescale ($\sim$2–3 months) however, did not seem to be dependent on the eddy polarity. In contrast, the eddy/mean flow interaction may have to be further considered in the case of cyclonic eddies. The presence of moorings extending meridionally should help to investigate this question.

Additional moorings may also allow to study the extent of the Antilles Current and its effect on the decay of cyclones and anticyclones. In that case, the horizontal scales and the direction of energy propagation of the detected internal waves could also be investigated. This will also provide a better estimation of their generation sites, which is believed from our study to happen in the lee of the topographic rise. Furthermore, the wave activity is expected to be enhanced over abyssal hills of smaller scales than the topographic rise and also by the entire topographic rise, which extends northwestward and southeastward of Wba. Internal waves with longer periods than 10 hours may be investigated during anticyclonic conditions with particular attention to wind-induced near-inertial waves and M2 internal tides. The interaction of these three types of waves may be investigated using triad interactions to investigate whether anticyclones can also contribute to the wave activity at larger periods than 10 hours.

Further study using additional moorings or a model could help to determine the extent of the influence of these eddy-generated internal waves on the deep mixing and circulation at the boundary. From the analysis of a regional model it will become possible to estimate the form drag over the topographic rise and to evaluate it against the frictional drag. A dependence of the form drag to the eddy polarity is expected as anticyclones were found to enhance the internal wave activity. This may help to assess the removal of eddy energy at the western boundary, which remains a fundamental question in determining energy budget and the role of turbulent flows in shaping the large-scale ocean circulation.

Bibliography

Amante C., and B. W. Eakins (2009), ETOPO1 1 Arc-Minute Global Relief Model: Procedures, Data Sources and Analysis, *NOAA Technical Memorandum NESDIS NGDC-24,* 1–19.

Anderson, D. L. T., and A. E. Gill (1975), Spin-up of a stratified ocean, with applications to upwelling. *Deep-sea Res., 22*, 583–596.

Antoni, J. and J. Schoukens (2009), Optimal settings for measuring frequency response functions with weighted overlapped segment averaging, *IEEE T. Instrumentation and Measurement, 58*, 3276–3287.

Atkinson, C. P., H. L. Bryden, S. A. Cunningham, and B. A. King (2012), Atlantic transport variability at 25°N in six hydrographic sections, *Ocean Sci., 8*, 497–523.

Avila, L. A., and J. P. Cangialosi (2011), Hurricane Irene Tropical Cyclone Report, *National Hurricane Center.*

Baines, P. G. (1995), Topographic Effects in Stratified Flows, *Cambridge University Press.*

Baringer, M. O., and J. C. Larsen (2001), Sixteen years of Florida current transport at 27°N, *Geophys. Res. Lett., 28*, 3179–3182.

Bell, T. H. (1975), Topographically generated internal waves in the open ocean, *J. Geophys. Res., 80*, 320–327.

Bingham, R. J., C. W. Hughes, V. Roussenov, and R. G. Williams (2007), Meridional coherence of the North Atlantic meridional overturning circulation, *Geophys. Res. Lett, 34*, L23606.

Brachet, S., P. Y. Le Traon, and C. Le Provost (2004), Mesoscale variability from a high-resolution model and from altimeter data in the North Atlantic Ocean, *J. Geophys. Res., 109*, C12025.

Brearley J. A., K. L. Sheen, A. C. Naveira Garabato, D. A. Smeed, and S. Waterman (2013), Eddy-induced modulation of turbulent dissipation over rough topography in the Southern Ocean, *J. Phys. Oceanogr., 43*, 2288–2308.

Broecker, W. S. (2003), Does the trigger for abrupt climate change reside in the ocean or in the atmosphere?, *Science, 300*, 1519–1522.

Bryden, H. L., W. E. Johns, and P. M. Saunders (2005a), Deep western boundary current east of Abaco: Mean structure and transport, *J. Mar. Res., 63*, 35–57.

Bryden, H. L., H. R. Longworth, and S. A. Cunningham (2005b), Slowing of the Atlantic meridional overturning circulation at 25°N, *Nature, 438*, 655–657.

Bryden, H. L., A. Mujahid, S. A. Cunningham, and T. Kanzow (2009), Adjustment of the basin-scale circulation at 26°N to variations in Gulf Stream, deep western boundary current and Ekman transports as observed by the Rapid array, *Ocean Sci., 5*, 421–433.

Bryden, H. L., B. A. King, G. D. McCarthy, and E. L. McDonagh (2014), Impact of a 30% reduction in Atlantic meridional overturning during 2009–2010, *Ocean Sci., 10*, 683–691.

Cangialosi, J. P. (2010), Hurricane OTTO Tropical Cyclone Report, *National Hurricane Center*

Chaigneau, A., M. Le Texier, G. Eldin, C. Grados, and O. Pizarro (2011), Vertical structure of mesoscale eddies in the eastern South Pacific Ocean: A composite analysis from altimetry and Argo profiling floats, *J. Geophys. Res., 116*, C11025.

Chelton, D. and M. Schlax (1996), Global observations of oceanic Rossby waves, *Science, 272*, 234.

Chelton, D., M. Schlax, K. E. Naggar, and N. Siwertz (1998), Geographical variability of the first baroclinic Rossby radius of deformation, *J. Phys. Oceanogr., 28*, 433–460.

Chelton, D. B., M. G. Schlax, R. M. Samelson, and R. A. de Szoeke (2007), Global observations of large oceanic eddies, *Geophys. Res. Lett., 34*, L15606.

Chelton, D. B., M. G. Schlax, and R. M. Samelson (2011), Global observations of nonlinear mesoscale eddies, *Prog. Oceanogr., 91*, 167–216.

Chidichimo, M. P., T. Kanzow, S. A. Cunningham, W. E. Johns, and J. Marotzke (2010), The contribution of eastern-boundary density variations to the Atlantic meridional overturning circulation at 26.5°N, *Ocean Sci., 6*, 475–490.

Cipollini, P., D. Cromwell, M. S. Jones, G. D. Quartly, and P. G. Challenor (1997), Concurrent altimeter and infrared observations of Rossby wave propagation near 34°N in the northeast Atlantic, *Geophys. Res. Lett., 24*, 889–892.

Cipollini, P., D. Cromwell, G. D. Quartly, and P. G. Challenor (2000), Remote sensing of oceanic extra-tropical Rossby waves. *Satellites, Oceanography and Society,* D. Halpern, Ed., Elsevier, 99–119.

Cunningham, S. A., T. Kanzow, D. Rayner, M. O. Baringer, W. E. Johns, J. Marotzke, H. R. Longworth, E. M. Grant, J. J.-M Hirschi, L. M. Beal, C. S. Meinen, and H. L. Bryden (2007), Temporal Variability of the Atlantic Meridional Overturning Circulation at 26.5°N, *Science, 317*, 935–938.

Cushman-Roisin, B. and J.-M. Beckers (2011), Introduction to Geophysical Fluid Dynamics: Physical and Numerical Aspects, *Academic Press.*

Cuypers, Y., X. Le Vaillant, P. Bouruet-Aubertot, J. Vialard, and M. J. McPhaden (2013), Tropical storm-induced near-inertial internal waves during the Cirene experiment: Energy fluxes and impact on vertical mixing, *J. Geophys. Res., 118*, 358–380.

D'Asaro, E., C. E. Eriksen, M. D. Levine, P. Niiler, C. A. Paulson, and P. V. Meurs (1995), Upper-ocean inertial currents forced by a strong storm. Part I: Data and comparisons with linear theory, *J. Phys. Oceanogr., 25*, 2909–2936.

Dee D.P. et. al. (2011), The ERA-Interim reanalysis: configuration and performance of the data assimilation system. *Q. J. R. Meteorol. Soc., 137*, 553–597.

Desaubies, Y. and M. C. Gregg (1981), Reversible and irreversible finestructure, *J. Phys. Oceanogr., 11*, 541–556.

Dewar, W. K. and A McC. Hogg (2010), Topographic inviscid dissipation of balanced flow, *Ocean Modell., 32*, 1–13.

Ducet, N., P. Y. Le Traon, and G. Reverdin (2000), Global high-resolution mapping of ocean circulation from TOPEX/Poseidon and ERS-1 and -2, *J. Geophys. Res., 105*, 19,477–19,498.

Emery, W. and R. Thomson (2001), Data analysis methods in physical oceanography, *Elsevier Science.*

Ferrari R. and C. Wunsch (2009), Ocean circulation kinetic energy: Reservoirs, sources, and sinks, *Annu. Rev. Fluid Mech., 41*, 253–282.

Fofonoff, N. P. (1969), Spectral characteristics of internal waves in the ocean, *Deep Sea Res., 16*, 58–71.

Frajka-Williams E., W. E. Johns, C. S. Meinen, L. M. Beal, and S. A. Cunningham (2013), Eddy impacts on the Florida Current, *Geophys. Res. Lett., 40*, 349–353.

Fratantoni, D. M. and P. L. Richardson (2006), The evolution and demise of North Brazil Current rings, *J. Phys. Oceanogr., 36*, 1241–1264.

Fu, L.-L. (2006), Pathways of eddies in the South Atlantic Ocean revealed from satellite altimeter observations, *Geophys. Res. Lett., 33*, L14610.

Fu, L.-L. and G. R. Flierl (1980), Nonlinear energy and enstrophy transfers in a real-

istically stratified ocean, *Dyn. Atmos. Oceans, 4*, 219–246.

Fuglister, F. C. (1960), Atlantic Ocean Atlas of Temperature and Salinity Profiles and Data from the International Geophysical Year of 1957-1958, *Vol. 1, Woods Hole Oceanographic Institution Atlas Series,* WHOI, Woods Hole, Massachusetts.

Ganachaud, A. (2003), Error budget of inverse box models: The North Atlantic, *J. Atmos. Ocean. Technol., 20*, 1641–1655.

Garrett, C. J. R., and W. H. Munk (1975), Space–time scales of internal waves. A progress report, *J. Geophys. Res., 80*, 291–297.

Gill, A. E. (1982), Atmosphere-Ocean Dynamics, *Academic Press.*

Gill, A. E. and P. P. Niiler (1973), The theory of the seasonal variability in the ocean, *Deep Sea Res., 20*, 141–177.

Gonella, J. (1972), A rotary-component method for analysing meteorological and oceanographic vector time series, *Deep-Sea Res., 19*, 833–846.

Gregg, M C. (1989), Scaling turbulent dissipation in the thermocline, *J. Geophys. Res., 94*, 9686–9698.

Gregg, M. C., and E. Kunze (1991), Shear and strain in Santa Monica Basin, *J. Geophys. Res., 96*, 16,709–16,719.

Gregg, M. C., T. B. Sanford, and D. P. Winkel (2003), Reduced mixing from the breaking of internal waves in equatorial waters, *Nature, 422*, 513–515.

Gregory, J. M., et al. (2005), A model intercomparison of changes in the Atlantic thermohaline circulation in response to increasing atmospheric CO_2 concentration, *Geophys. Res. Lett, 32*, L12703.

Gunn, J. T. and D. R. Watts (1982), On the currents and water masses north of the Antilles/Bahamas arc, *J. Mar. Res., 40*, 1–18.

Hall, M. M. and H. L. Bryden (1982), Direct estimates and mechanisms of ocean heat transport, *Deep Sea Res., 29*, 339–359.

Halliwell, G. R., P. Cornillon, and D. A. Byrne (1991), Westward-propagating SST anomaly features in the Sargasso Sea, 1982-88, *J. Phys. Oceanogr., 21*, 635–649.

Henyey, F. S., J. Wright, and S. M. Flatte (1986), Energy and action flow through the internal wave field: An eikonal approach, *J. Geophys. Res., 91*, 8487–8495.

Hirschi, J. J.-M., P. D. Killworth, and J. R. Blundell (2007), Subannual, seasonal, and interannual variability of the North Atlantic meridional overturning circulation, *J. Phys. Oceanogr., 37*, 246–1265.

Hirschi, J. J.-M., A. T. Blaker, B. Sinha, A. Coward, B. de Cuevas, S. Alderson, and G. Madec (2013), Chaotic variability of the meridional overturning circulation on subannual to interannual timescales, *Ocean Sci., 9*, 805–823.

Hogg, A. McC., W. K. Dewar, P. Berloff, and M. L. Ward (2011), Kelvin wave hydraulic control induced by interactions between vortices and topography, *J. Fluid Mech., 687*, 194–208.

Isern-Fontanet, J., E. García-Ladona, and J. Font (2003), Identification of marine eddies from altimetry, *J. Atmos. Oceanic Technol., 20*, 772–778.

Jackett, D. R. and T. J. McDougall (1997), A neutral density variable for the Worlds Oceans, *J. Phys. Oceanogr., 27*, 237–263.

Jaimes, B. and L. K. Shay (2010), Near-inertial wave wake of Hurricanes Katrina and Rita over mesoscale oceanic eddies, *J. Phys. Oceanogr., 40*, 1320–1337.

Jochumsen, K., M. Rhein, S. Hüttl-Kabus, and C. W. Böning (2010), On the propagation and decay of North Brazil Current rings, *J. Geophys. Res., 115*, C10004.

Johns, W. E., T. Kanzow, and R. Zantopp (2005), Estimating ocean transports with dynamic height moorings: An application in the Atlantic deep western boundary current, *Deep Sea Res., 52*, 542–1567.

Johns, W. E., L. M. Beal, M. O. Baringer, J. R. Molina, S. A. Cunningham, T. Kanzow, and D. Rayner (2008), Variability of shallow and deep western boundary currents off the Bahamas during 2004-05: Results from the 26°N RAPID-MOC array, *J. Phys. Oceanogr., 38*, 605–623.

Johns, W. E., M. O. Baringer, L. M. Beal, S. A. Cunningham, T. Kanzow, H. L. Bryden, J. J.-M. Hirschi, J. Marotzke, C. S. Meinen, B. Shaw, and R. Curry (2011), Continuous, array-based estimates of Atlantic Ocean heat transport at 26.5°N, *J. Climate, 24*, 2429 2449.

Kanzow, T., S. A. Cunningham, D. Rayner, J. J.-M. Hirschi, W. E. Johns, M. O. Baringer, H. L. Bryden, L. M. Beal, C. S. Meinen, and J. Marotzke (2007), Observed flow compensation associated with the MOC at 26.5°N in the Atlantic, *Science, 317*, 938941.

Kanzow, T., H. L. Johnson, D. P. Marshall, S. A. Cunningham, J. J.-M. Hirschi, A. Mujahid, H. L. Bryden, and W. E. Johns (2009), Basinwide integrated volume transports in an eddy-filled ocean, *J. Phys. Oceanogr., 39*, 3091–3110.

Kanzow, T., S. A. Cunningham, W. E. Johns, J. J.-M. Hirschi, J. Marotzke, M. O. Baringer, C. S. Meinen, M. P. Chidichimo, C. Atkinson, L. M. Beal, H. L. Bryden, and J. Collins (2010), Seasonal variability of the Atlantic meridional overturning circulation at 26.5°N, *J. Climate, 23*, 5678–5698.

Killworth, P. D., D. B. Chelton, and R. de Szoeke (1997), The speed of observed and theoretical long extra-tropical planetary waves, *J. Phys. Oceanogr., 27*, 1946–1966.

Killworth, P. D., and J. R. Blundell (2003), Long extratropical planetary wave propagation in the presence of slowly varying mean flow and bottom topography. Part I: The local problem, *J. Phys. Oceanogr., 33*, 784–801.

Klymak, J. M., S. Legg, and R. Pinkel (2010), High-mode stationary waves in stratified flow over large obstacles, *J. Fluid Mech., 644*, 312–336.

Köhler J., C. Mertens, M. Walter, U. Stöber, M. Rhein, and T. Kanzow (2014), Variability in the internal wave field induced by the Atlantic deep western boundary current at 16°N, *J. Phys. Oceanogr., 44*, 492–516.

Kundu, P. K., J. S. Allen, and R. L. Smith (1975), Modal decomposition of the velocity field near the Oregon coast, *J. Phys. Oceanogr., 5*, 683–704.

Kundu, P. K., I. M. Cohen, and D. R. Dowling (2012), Fluid Mechanics, *Academic Press.*

Kunze E. (1985), Near inertial-wave propagation in geostrophic shear, *J. Phys. Oceanogr., 15*, 544–565.

Kunze, E., E. Firing, J. M. Hummon, T. K. Chereskin, and A. M. Thurnherr (2006), Global abyssal mixing inferred from lowered ADCP shear and CTD strain profiles, *J. Phys. Oceanogr., 36*, 1553–1576.

Kurian, J., F. Colas, X. Capet, J. C. McWilliams, and D. B. Chelton (2011), Eddy properties in the California Current System, *J. Geophys. Res., 116*, C08027.

Kurczyn, J. A., E. Beier, M. F. Lavín, A. Chaigneau, and V. M. Godínez (2013), Anatomy and evolution of a cyclonic mesoscale eddy observed in the northeastern Pacific tropical-subtropical transition zone, *J. Geophys. Res., 118*, 1–20.

Lapeyre, G. (2009), What vertical mode does the altimeter reflect? On the decomposition in baroclinic modes and on a surface-trapped mode, *J. Phys. Oceanogr., 39*, 2857–2874.

Leaman K. D. and T. B. Sanford (1975), Vertical energy propagation of inertial waves: A vector spectral analysis of velocity profiles, *J. Geophys. Res., 80*, 1975–1978.

Lee, T., W. E. Johns, R. Zantopp, and E. Fillenbaum (1996), Moored observations of western boundary current variability and thermohaline circulation at 26.5°N in the subtropical North Atlantic, *J. Phys. Oceanogr., 26*, 962–983.

Levitus, S., R. Burgett, and T. Boyer (1994), *World Ocean Atlas 1994.* Vol 3: *Salinity*; Vol. 4: *Temperature*. NOAA Atlas NESDIS 3 & 4, U.S. Dept. of Commerce.

Llewellyn Smith, S. G. and W. R. Young (2003), Tidal conversion at a very steep

ridge. *J. Fluid Mech., 495*, 175–191.

Liang X. and A. M. Thurnherr (2012), Eddy-modulated internal waves and mixing on a midocean ridge, *J. Phys. Oceanogr., 42*, 1242–1248.

Longworth, H. R. (2007), Constraining variability of the Atlantic Meridional Overturning Circulation at 25°N from historical observations, 1980-2005, Ph.D. thesis, School of Ocean and Earth Science, University of Southampton, Southampton, UK, 200 pp.

Louis, J. P. and P. C. Smith (1982), The development of the barotropic radiation field of an eddy over a slope, *J. Phys. Oceanogr., 12*, 56–73.

Lynn, R. J. and J. L. Reid (1968), Characteristics and circulation of deep and abyssal waters, *Deep Sea Res., 15*, 577–598.

Marsh, R., B. A. de Cuevas, A. C. Coward, J Jacquin, J. J.-M. Hirschi, Y. Aksenov, A. J. G. Nurser, and S. A. Josey (2009), Recent changes in the North Atlantic circulation simulated with eddy-permitting and eddy-resolving ocean models, *Ocean Modell., 28*, 226–239.

McCarthy, G., E. Frajka-Williams, W. E. Johns, M. O. Baringer, C. S. Meinen, H. L. Bryden, D. Rayner, A. Duchez, C. Roberts, and S. A. Cunningham (2012), Observed interannual variability of the Atlantic meridional overturning circulation at 26.5°N, *Geophys. Res. Lett, 39*, L19609.

McGillicuddy Jr., D. J. et. al. (2007), Eddy/wind interactions stimulate extraordinary mid-ocean plankton blooms, *Science, 316*, 1021–1026.

McWilliams, J. C. and G. R. Flierl (1976), Optimal, quasi-geostrophic wave analyses of MODE array data, *Deep Sea Res., 23*, 285–300.

Meinen, C. S., W. E. Johns, S. L. Garzoli, E. V. Sebille, D. Rayner, T. Kanzow, and M. O. Baringer (2013), Variability of the Deep Western Boundary Current at 26.5°N during 2004-2009, *Deep Sea Res., Part II, 85*, 154–168.

MODE Group (1978), The Mid-Ocean Dynamics Experiment, *Deep Sea Res., 25*, 859–910.

Morrow, R., F. Birol, D. Griffin, and J. Sudre (2004), Divergent pathways of cyclonic and anticyclonic ocean eddies, *Geophys. Res. Lett., 31*, L24311.

Munk, W. H. (1966), Abyssal recipes, *Deep Sea Res., 13*, 707–730.

Nikurashin M. and R. Ferrari (2010), Radiation and dissipation of internal waves generated by geostrophic motions impinging on small-scale topography: Application to the Southern Ocean, *J. Phys. Oceanogr., 40*, 2025–2042.

Nikurashin M. and R. Ferrari (2011), Global energy conversion rate from geostrophic flows into internal lee waves in the deep ocean, *Geophys. Res. Lett., 38*, L08610.

Naveira Garabato, A. C., K. L. Polzin, B. A. King, K. J. Heywood, and M. Visbeck (2004), Widespread intense turbulent mixing in the Southern Ocean. *Science, 303*, 210–213.

Oakey, N. S., (1982), Determination of the rate of dissipation of turbulent energy from simultaneous temperature and velocity shear microstructure measurements, *J. Phys. Oceanogr., 12*, 256–271.

Osborn T. R. (1980), Estimates of the local rate of vertical diffusion from dissipation estimates, *J. Phys. Oceanogr., 10*, 83–89.

Osychny, V. and P. Cornillon (2004), Properties of Rossby waves in the North Atlantic estimated from satellite data, *J. Phys. Oceanogr., 34*, 61–76.

Parker, C. E. (1971), Gulf Stream rings in the Sargasso Sea, *Deep Sea Res., 18*, 981–993.

Percival, D. B. and A. T. Walden (1993), Spectral Analysis for Physical Applications, *Cambridge University Press.*.

Pohlmann, H., F. Sienz, and M. Latif (2006), Influence of the multidecadal Atlantic meridional overturning circulation variability on European climate, *J. Climate, 19*, 6062–6067.

Polzin, K. L., J. M. Toole, and R. W. Schmitt (1995), Finescale parameterizations of turbulent dissipation, *J. Phys. Oceanogr., 25*, 306–328.

Polzin, K. L., J. M. Toole, J. R. Ledwell, and R. W. Schmitt (1997), Spatial variability of turbulent mixing in the abyssal ocean, *Science, 276*, 93–96.

Polzin K. L., E. Kunze, J. Hummon, and E. Firing (2002), The finescale response of lowered ADCP velocity profiles, *J. Phys. Oceanogr., 19*, 205–224.

Polzin, K. L., A. C. Naveira Garabato, T. N. Huussen, B. M. Sloyan, and S. Waterman (2014), Finescale parameterizations of turbulent dissipation, *J. Geophys. Res., 119*, 1383–1419.

Qiu, B., and S. Chen (2005), Eddy-induced heat transport in the subtropical North Pacific from ARGO, TMI, and altimetry measurements, *J. Phys. Oceanogr., 35*, 458–473.

Rayner, D., J. J.-M. Hirschi, T. Kanzow, W. E. Johns, P. G. Wright, E. Frajka-Williams, H. L. Bryden, C. S. Meinen, M. O. Baringer, J. Marotzke, L. M. Beal, and S. A. Cunningham (2011), Monitoring the Atlantic meridional overturning circulation, *Deep Sea Res., Part II, 58*, 1744–1753.

Rhines, P. B. (1977), The dynamics of unsteady currents, *The Sea, 6*, 189–318.

Richman, J. G., C. Wunsch, and N. G. Hogg (1977), Space and time scales of mesoscale

motion in the Western North Atlantic, *Rev. Geophys., 15*, 345–420.

Roemmich, D. and C. Wunsch (1985), Two transatlantic sections: meridional circulation and heat flux in the subtropical North Atlantic Ocean, *Deep Sea Research, 32*, 619–664.

Roemmich, D. and J. Gilson (2001), Eddy transport of heat and thermocline waters in the North Pacific: A key to interannual/decadal climate variability?, *J. Phys. Oceanogr., 31*, 675–687.

Salmon, R. (1978), Two-layer quasi-geostrophic turbulence in a simple special case, *Geophys. Astrophys. Fluid Dyn., 10*, 25–52.

Sangrà, P., et al. (2009), The Canary Eddy Corridor: A major pathway for long-lived eddies in the subtropical North Atlantic, *Deep Sea Res., Part I, 56*, 2100–2114.

Schlax, M. G. and D. B. Chelton (1994), Aliased tidal errors in TOPEX/POSEIDON sea surface height data, *J. Geophys. Res., 99*, 24761–24775.

Scott, R. B. and F. Wang (2005), Direct evidence of an oceanic inverse kinetic energy cascade from satellite altimetry, *J. Phys. Oceanogr., 35*, 1650–1666.

Sen A., R. B. Scott, and B. K. Arbic (2008), Global energy dissipation rate of deep-ocean low-frequency flows by quadratic bottom boundary layer drag: Computations from current-meter data, *Geophys. Res. Lett., 35*, L09606.

Sheen K. L., J. A. Brearley, A. C. Naveira Garabato, D. A. Smeed, S. Waterman, J. R. Ledwell, M. P. Meredith, L. St. Laurent, A. M. Thurnherr, J. M. Toole, and A. J. Watson (2013), Rates and mechanisms of turbulent dissipation and mixing in the Southern Ocean: Results from the Diapycnal and Isopycnal Mixing Experiment in the Southern Ocean (DIMES), *J. Geophys. Res., 118*, 2774–2792.

Shi, C. and D. Nof (1994), The destruction of lenses and generation of wodons, *J. Phys. Oceanogr., 24*, 1120–1136.

Siegel, D. A., D. J. McGillicuddy Jr., and E. A. Fields (1999), Mesoscale eddies, satellite altimetry, and new production in the Sargasso Sea, *J. Geophys. Res., 104*, 13,359-13,379.

Simpson, J. J., T. D. Dickey, and C. J. Koblinsky (1984), An offshore eddy in the California Current System Part I: interior dynamics, *Prog. Oceanog., 13*, 5–49.

Sinha, B., B. Topliss, A. T. Blaker, and J. J.-M Hirschi (2013), A numerical model study of the effects of interannual time scale wave propagation on the predictability of the Atlantic meridional overturning circulation, *J. Geophys. Res., 118*, 1–16.

Smeed, D. A., G. D. McCarthy, S. A. Cunningham, E. Frajka-Williams, D. Rayner, W. E. Johns, C. S. Meinen, M. O. Baringer, B. I. Moat, A. Duchez, and H. L. Bryden (2014), Observed decline of the Atlantic meridional overturning circulation 2004–2012, *Ocean Sci, 10*, 29–38.

Smith, K. S. and G. K. Vallis (2001), The scales and equilibration of midocean eddies: freely evolving flow, *J. Phys. Oceanogr., 31*, 554–571.

Souza, J. M. A. C., C. de Boyer Montégut, C. Cabanes, and P. Klein (2011), Estimation of the Agulhas ring impacts on meridional heat fluxes and transport using ARGO floats and satellite data, *Geophys. Res. Lett., 38*, L21602.

Stammer, D. (1997), Global characteristics of ocean variability estimated from regional TOPEX/POSEIDON altimeter measurements, *J. Phys. Oceanogr., 27*, 1743–1769.

Stöber U., M. Walter, C. Mertens, and M. Rhein (2004), Mixing estimates from hydrographic measurements in the Deep Western Boundary Current of the North Atlantic, *Deep-Sea Res. I, 55*, 721–736.

Szuts, Z. B., J. R. Blundell, M. P. Chidichimo, and J. Marotzke (2012), A vertical-mode decomposition to investigate low-frequency internal motion across the Atlantic at 26°N, *Ocean Sci., 8*, 345–367.

Tailleux, R. and J. McWilliams (2000), Acceleration, creation, and depletion of wind-driven, baroclinic Rossby waves over an ocean ridge, *J. Phys. Oceanogr., 30*, 2186–2213.

Talley, L. D., G. L. Pickard, W. J. Emery, and J. H. Swift (2011), Descriptive Physical Oceanography: An Introduction (Sixth Edition), *Elsevier.*

Trenberth, K. E., J. M. Caron, and D. P. Stepaniak (2001), The atmospheric energy budget and implications for surface fluxes and ocean heat transports. *Climate Dyn., 17*, 259–276.

Tulloch, R., J. Marshall, and K. S. Smith (2009), Interpretation of the propagation of surface altimetric observations in terms of planetary waves and geostrophic turbulence, *J. Geophys. Res., 114*, C02005.

Waterman, S., A. C. Naveira Garabato, and K. L. Polzin (2013), Internal waves and turbulence in the Antarctic circumpolar current, *J. Phys. Oceanogr., 43*, 259–282.

Wunsch, C. (1997), The vertical partition of oceanic horizontal kinetic energy, *J. Phys. Oceanogr., 27*, 1770–1794.

Wunsch, C. (2008), Mass and volume transport variability in an eddy-filled ocean, *Nat. Geosci., 1*, 165–168.

Zhai X., H. L. Johnson, and D. P. Marshall (2010), Significant sink of ocean-eddy energy near western boundaries, *Nat. Geosci., 3*, 608–612